BRASKI

DOE/ER-0045/1

Alloy Development for Irradiation Performance

Quarterly Progress Report

For Period Ending December 31, 1979

U.S. Department of Energy

Assistant Secretary for Energy Technology

Office of Fusion Energy

Printed in the United States of America. Available from
National Technical Information Service
U.S. Department of Commerce
5285 Pori Royal Road, Springfield, Virginia 22161
NTIS price codes—Printed Copy: A09 Microfiche A01

This report was prepared as an account of work sponsored by an agency of the United States Government. Neither the United States Government nor any agency thereof, nor any of their employees, makes any warranty, express or implied, or assumes any legal liability or responsibility for the accuracy, completeness, or usefulness of any information, apparatus. product, or process disclosed, or represents that its use would not infringe privately owned rights. Reference herein to any Specific commercial product, process, or service by trade name, trademark, manufacturer, or otherwise, does not necessarily constitute or imply its endorsement, recommendation. or favoring by the United States Government or any agency thereof. The views and opinions of authors expressed herein do not necessarily State or reflect those of the United States Government or any agency thereof.

DOE/ER-0045/1
Distribution
Category
UC-20, 20c

ALLOY DEVELOPMENT FOR IRRADIATION PERFORMANCE QUARTERLY PROGRESS REPORT FOR PERIOD ENDING DECEMBER 31,1979

Compiled and Edited by B. G. Ashdown, ORNL
from Contributions of Participating Laboratories

ARGONNE NATIONAL LABORATORY

GENERAL ATOMIC COMPANY

HANFORD ENGINEERING DEVELOPMENT LABORATORY

McDONNELL DOUGLAS ASTRONAUTICS COMPANY

NAVAL RESEARCH LABORATORY

OAK RIDGE NATIONAL LABORATORY

WESTINGHOUSE FUSION POWER SYSTEMS

Date Published: **April** *1980*

Prepared by
OAK RIDGE NATIONAL LABORATORY
Oak Ridge, Tennessee 37830
operated by
UNION CARBIDE CORPORATION
for the
DEPARTMENT OF ENERGY
Under Contract No. W-7405-eng-26

FOREWORD

This report is the eighth in a series of Quarterly Technical Progress Reports on ***"Alloy Development for Irradiation Performance"*** (ADIP), which is one element of the Fusion Reactor Materials Program, conducted in support of the Magnetic Fusion Energy Program of the U.S. Department of Energy. Other elements of the Materials Program are:

- ***Damage Analysis and Fundamental Studies*** *(DAFS)*
- ***Ptasma-Materials Interaction*** *(PMI)*
- ***Special-Purpose Materials*** *(SPM)*

The first seven reports in this series are numbered DOE/ET-0058/1 through 7. This report is the first in a new numbering sequence, DOE/ER-0045/1.

The ADIP program element is a national effort composed of contributions from a number of National Laboratories and other government laboratories, universities, and industrial laboratories. It was organized by the Materials and Radiation Effects Branch, Office of Fusion Energy, DOE, and a Task Group on ***Alloy Development for Irradiation Performance,*** which operates under the auspices of that Branch. The purpose of this series of reports is to provide a working technical record of that effort for the use of the program participants, for the fusion energy program in general, and for the Department of Energy.

This report is organized along topical lines in parallel to a Program Plan of the same title so that activities and accomplishments may be followed readily relative to that Program Plan. Thus, the work of a given laboratory may appear throughout the report. Chapters 1, 2, 8, and 9 review activities on analysis and evaluation, test methods development, status of irradiation experiments, and corrosion testing and hydrogen permeation studies, respectively. These activities relate to each of the alloy development paths. Chapters 3, 4, 5, 6, and 7 present the ongoing work on each alloy development path. The Table of Contents is annotated for the convenience of the reader.

This report has been compiled and edited under the guidance of the Chairman of the Task Group on ***Alloy Development for Irradiation Performance,*** E. E. Bloom, Oak Ridge National Laboratory, and his efforts, those of the supporting staff of ORNL and the many persons who made technical contributions are gratefully acknowledged. T. C. Reuther, Materials and Radiation Effects Branch, is the Department of Energy Counterpart to the Task Group Chairman and has responsibility for the ADIP Program within DOE.

Klaus M. Zwilsky, Chief,
Materials and Radiation Effects Branch
Office of Fusion Energy

CONTENTS

FOREWORD., ... iii

1. ANALYSIS AND EVALUATION STUDIES 1

1.1 Materials Handbook for Fusion Energy Systems (McDonnell Douglas Astronautics Company — St. Louis and Hanford Engineering Development Laboratory) 2

The Materials and Radiation Effects branch of the Office of Fusion Energy has established a mterials data book for use in fusion related studies. This handbook will be known as the Materials Handbook for Fusion Energy Systems and initial copies should be available in the near future. The handbook will be part of the Analysis and Evaluation subtask group of ADIP and will establish the data requirements and priorities for the preparation of the individual data sheets. At the present time Analysis and Evaluation suhtask group has given the data sheets to support the ETF study the first priority. Based on recom mendations from R. E. Nygren (ETF-Materials) the first data sheets will be those relating to the austenitic stainless steels.

1.2 Assessment of Cyclic Creep-Fatigue Life of First-Wall Structural Material (Oak Ridge National Laboratory) 5

Cyclic lifetimes for a fusion reactor first wall were independently evaluated with two methods: linear damage summation (LDS), which is currently being employed for use in ASME high-temperature design Code Case N-47, and strain-range partitioning (SRP), which is being studied for inclusion in the design Code. Despite their diversity, results estimated with the two analytical techniques agreed reasonably well in several practical design situations. Furthermore, this excercise has reaffirmed our earlier finding that 20%-cold-worked type 316 stainless steel could be used as a fusion first-wall material meeting a 8 to 10 MW-year/m^2 lifetime goal for a neutron wall loading of about 2 MW/m^2 and a maximum temperature of about 500°C.

2. TEST MATRICES AND TEST METHODS DEVELOPMENT 17

2.1 Initial Test Results on Miniature Compact Tension Fracture Toughness Specimen (Hanford Engineering Development Laboratory) 18

Fracture toughness tests have been performed on miniature circular tension specimens of HT-9 at room temperature. The shape and size of specimens were tailored for efficient stacking in EBR-II irradiation. Furthermore, the number of specimens required will be reduced by using a single specimen method. The electropotential technique has been applied to obtain a calibration curve for voltage change versus crack extension. Using this calibration curve, J-integral measurements are imde. They are in agreement with those from a multi-specimen method.

3. PATH A ALLOY DEVELOPMENT — AUSTENITIC STAINLESS STEELS 27

3.1 The Influence of Irradiation on the Properties of Path A Alloy Weldments (Oak Ridge National Laboratory) 28

Weldments of type 316 stainless steel joining 20%-cold-worked type 316 stainless steel base metal have been irradiated in the HFIR over the temperature range 280 to 620°C. Fluences up to 1.3 × 10^{26} n/m^2 [>0.1 MeV (0.02 pJ)] produced 5.3 to 9.8 dpa and 170 to 480 at. ppm He. Tensile tests at temperatures near the irradiation temperature showed strength values greater than those of unirradiated material for temperatures below 475°C but comparable with the unirradiated strengths for higher temperatures. Maximum elongation occurred at 475°C but vas below unirradiated values for all irradiation conditions.

4. PATH B ALLOY DEVELOPMENT — Fe-Ni-Cr Alloys 35

5. PATH C ALLOY DEVELOPMENT — REACTIVE AND REFRACTORY ALLOYS . . . 37

5.1 Mechanical Property Testing of Unirradiated Path C Alloys (Oak Ridge National Laboratory) 38

Preparation for cyclic fatigue tests of vanadium-based alloys has been initiated. Appropriate heat treatments will be determined from the study of microstructures of the annealed samples. Strain-controlled fatigue tests of Nb–1% Zr are continuing. Additional test results show that Nb–1% Zr has only marginally better fatigue resistance than does 20%-cold-worked type 316 stainless steel tested in the low-cycle fatigue range.

5.2 Microstructure of Titanium Alloys After EBR-II Irradiation (McDonnell Douglas Astronautics Company — St. Louis and McDonnell Douglas Research Labs) 42

Bulk annealing experiments performed on Ti-6Al-4V indicate that the beta precipitate observed, following irradiation, was dissolved after annealing for 24 hours at 650°C. The temperature where the precipitate dissolved was well below the beta transus and appears to support the contention that the precipitate is irradiation induced and not a result of supersaturation of the alpha phase. Instead the precipitate appears to be caused by the alpha solute segregation at vacancy sinks. These sinks appear to act as traps for the vanadium atoms which have a high diffusion mobility as titanium because of its smaller atom size. The presence of a larger concentration of vanadium at the defect site results in alteration of the equilibrium concentration resulting in the precipitation of the beta phase. The near alpha alloys Ti-6242S and Ti-56215 use molybdenum as a beta stabilizer, however, because of its larger atom size and low concentration, it effectively suppresses the irradiation beta formation under these irradiation conditions.

5.3 Effect of Hydrogen on Flaw Growth of Titanium Alloy Ti-6242s (McDonnell Douglas Astronautics Company — St. Louis) 50

The planning of this study is complete. Modified wedge opening loading (modified WOL) specimens are being machined from 0.32 cm (0.125 inch) thick Ti-6242s. One half of the specimen blanks are being charged with hydrogen to a desired bulk level of 500 wppm with the hydrogen uniformly distributed throughout the samples.

5.4 Hydrogen in Titanium Alloys (McDonnell Douglas Astronautics Company — St. Louis) 53

A review of current knowledge concerning the effects of hydrogen on the mechanical properties of titanium has provided minimal data directly applicable to fusion reactor usage. Although no definite conclusions have been drawn as yet, it presently appears that because of the large number of interdependent variables associated with hydrogen interactions it may be impractical to predict with any degree of certainty the embrittlement effects, if any, for the alloys of interest for fusion energy. There are some indications that titanium alloys m y not be adversely degraded in the elevated temperature, low hydrogen pressure conditions in the reactor.

5.5 Examination of Titanium Alloy Specimens Irradiated in EBR-II (Hanford Engineering Development Laboratory) 58

The AD-1 experiment consists of three uninstrumented pins containing microstructural and mechanical property specimens made from titanium alloys. These three pins were designed for irradiation temperatures of 394°C, 450°C and 500°C and have been irradiated in EBR-11 until fluences greater than $4 \times 10^{22} n/cm^2$ (E>0.11 MeV) have been attained. Evidence of corrosion was observed on several specimens contained in the subcapsule designed for an irradiation temperature of 500°C. The subsequent opening of the other two subcapsules has been delayed until more information has been obtained concerning this corrosion.

6. PATH D ALLOY DEVELOPMENT — INNOVATIVE MATERIAL CONCEPTS 71

6.1 Development of Iron-Base Alloys with Long-Range-Ordered Crystal Structure (Oak Ridge National Laboratory) 72

A series of iron-base tong-range-ordered (LRO) alloys with compositions $(Fe,Ni,Co)_3V$ are being developed for fusion energy applications. The alloys form a cubic ordered structure similar to $AuCu_3$ below their critical ordering temperature (T_c). The alloys in the ordered state are ductile, with total elongation in excess of 30% at room temperature. Tensile tests of the LRO alloys at elevated temperatures indicate an unusually attractive

mechanical behavior. Their strength, instead of decreasing as with conventional alloys, increases with temperatures because of ordering. The ordered alloys also exhibit excellent creep strength. Their creep rate at 650°C is lower than that of type 316 stainless steel by more than three orders of magnitude.

7. PATH E ALLOY DEVELOPMENT — FERRITIC STEELS 81

7.1 Welding and Fabrication of Candidate Ferritic Steel (General Atomic Company) 82

The logic and overall approach in the program was developed to meet the objectives of making firm recommendations regarding the ferritic steel fabrication/welding procedures and fracture management scheme for ETF components. Candidate sources were evaluated and a procurement plan for a 30,000 lb program heat of 12 Cr steel was developed. A chemical composition specification was formulated. A preliminary study to establish welding procedures for specimens to be exposed in the near term EBR 11 and HFIR irradiation was initiated and test panel welding was completed. The microstructural features of conventional gas-tungsten arc (GTA) and advanced laser weldments of HT9 were evaluated and compared. Preliminary evidence indicates that laser welding may be a promising method for producing 12 Cr wetdments.

7.2 Preparation of Nickel-Doped Ferritic Alloys for HFIR Irradiation to Produce Helium (Oak Ridge National Laboratory) 100

Small heats of HT9 and 9 Cr-1 Mo steels have been prepared containing 1 and 2% Ni. An additional heat of each alloy was prepared with 2% Ni but with adjustments in the carbide-forming elements to restore the chromium equivalent to a value near that of the original alloy. Tensile and transmission electron microscope (TEM) specimens of these mterials will be irradiated in the High Flux Isotope Reactor (HFIR). The thermal flux in the HFIR will result in the formation of helium in concentrations approximating those produced in fusion reactor service.

7.3 Test Plan for the Investigation of Irradiation Effects Upon Mechanical Properties of Ferritic Alloys (Hanford Engineering Development Laboratory) 105

The AD-2 experiment will consist of six, uninstrumented B-7c pins containing microstructure and mechanical property specimens made from ferritic alloys. Alloy selection, irradiation temperatures and the test matrix have been specified and approved by the Alloy Development for Near Term Applications Working Group. Approval in principle has been granted by DOE for the AD-2 experiment and irradiation will begin at EBR-11 in June, 1980.

7.4 **Environment Effects on Properties of Ferritic Steels (Argonne National Laboratory)** 115

This program was initiated in the first quarter of FY 1980 with initial phases of the program focused on (1) combined effects of stress and coolant environment on the properties of ferritic steels and (2) the compatibility of ferritic steels with candidate solid tritium-breeding materials and neutron multipliers. The first experiments include determination of the effects of a liquid lithium environment on the fatigue properties of the Sandvik RT-9 alloy and tests on the compatibility of candidate ferritic steels with Li_2O and Li_2SiO_3.

8. STATUS OF IRRADIATION EXPERIMENTS AND MATERIALS INVENTORY . . . 119

8.1 Irradiation Experiment Status and Schedule 120

Bar charts show the irradiation experiments schedule, including experiments completed, in progress, and planned. Experiments are presently under way in the ORR and the HFIR, which are mixed-spectrum reactors, and in the EBR-11, which is a fast reactor.

8.2 ETM Research Materials Inventory (Oak Ridge National Laboratory and McDonnell Douglas) 127

The Office of Fusion Energy has assigned program responsibility to ORNL for the establishment and operation of a central inventory of research materials to be used in the Fusion Reactor Materials research and development programs. The objective is to provide a common supply of materials for the Fusion Reactor Materials Program. This wilt minimize unintended materials variables and provide for economy in procurement and for centralized record-keeping. Initially this inventory is to focus on materials related to first-wall and structural applications and related research, but various special purpose materials may be added in the future.

9. CORROSION TESTING AND HYDROGEN PERMEATION STUDIES 139

9.1 Hydrogen Dissolution and Permeation Studies of ADIP Program Alloys (Argonne National Laboratory) 140

Efforts to characterize the hydrogen dissolution and permeation characteristics of alloys currently under development in the ADIP Program have continued. An effort to measure the hydrogen permeability of pure α-titanium was generally unsuccessful owing to a tendency of the material to creep in the gasket-seal-type assembly normally used for difficult-to-weld alloys. Work a the solubility of hydrogen in Ti-6Al-4V was completed. Rased on these results, the amount of hydrogen dissolved in a Ti-6Al-4V fusion reactor first wall assembly could range from several

hundred grams to a few kilograms, depending on the effective average T_2 pressure in the plasma boundary region and the first wall temperature distribution. Results of a survey of the hydrogen permeation characteristics of ferritic alloys showed that they are ~5-times more permeable than 300-series stainless steels in the surface-unperturbed state, but that significant reductions in permeability can be achieved for oxidized aluminum-and chromium-containing ferritics.

9.2 Vanadium Alloy/Lithium Pumped-Loop Studies (Argonne National Laboratory) 148

The stainless steel-clad vanadium alloy loop with circulating lithium has continued to operate through the first quarter of FY 1980. Test samples of zirconium, vanadium, V-15Cr-5Ti, titanium, and yttrium have been exposed at 873 K to investigate the distribution of nonmetallic elements in lithium/refractory metal systems. The zirconium and yttrium exposures have been used to adjust and evaluate the nonmetallic (O, N, H, and C) concentration in lithium. Results of hydrogen analyses of the test samples have been compared with calculated distribution coefficients for hydrogen. Similar analyses of oxygen and nitrogen distribution are in progress.

9.3 Corrosion of Fe-Ni-Cr and Fe-Ni-V Alloys in Static Lithium (Oak Ridge National Laboratory) 152

Data are reported on the compatibility of 500 and 600°C lithium with alloy 800 [46 Fe—32 Ni—21 Cr (wt %)] and a long-range-ordered (LRO) alloy [45 Fe—32 Ni—23 V (wt %)]. Although these alloys contained similar concentrations of Fe and Ni, alloy 800 was severely corroded in certain instances, while the LRO alloy resisted attack and incurred no loss of tensile properties in Li.

9.4 Corrosion of Type 316 Stainless Steel and Alloys B1 and B3 in Lithium Thermal-Convection Loops (Oak Ridge National Laboratory) 158

Results from three thermal-convection-loop experiments are reported. The corrosion rates of ADIP alloys B1 and R3 [64 Fe—25 Ni—10 Cr—1 Mo (wt %) and 56 Fe—30 Ni—12 Cr—3 Mo (wt %)], respectively1 were much greater than that of type 316 stainless steel. Similar corrosion mtes in flowing lithium were measured for type 316 stainless steel in both austenite and a-ferrite systems. Adding aluminum to a type 316 stainless steel loop that had already been circulating lithium for over 5000 h resulted in flow restrictions that were probably the result of aluminum deposits in the coldest part of the circuit. Consequently, corrosion inhibition by aluminum addition to the lithium is most effective in a new system.

9.5 Compatibility of Type 316 Stainless Steel with the Tritium-Processing Salt LiF-LiCl-LiBr (Oak Ridge National Laboratory) 166

A type 316 stainless steel thermal-convection loop circulated LiF-LiCl-LiBr for over 8000 h. The steady-state corrosion rate was low enough to assure adequate compatibility between the salt and stainless steel.

1. ANALYSIS AND EVALUATION STUDIES

1.1 MATERIALS HANDBOOK FOR FUSION ENERGY SYSTEMS - J. W. Davis (McDonnell Douglas Astronautics Company - St. Louis) and J. C. Spanner, (Hanford Engineering Development Laboratory).

1.1.1 ADIP Task

Task Number 1.A.1 - Define material property requirements and make structural life predictions.

1.1.2 Objective

To provide an authoritative and consistent source of material property data for use by the fusion energy community in concept evaluation, design, safety analysis, and performance/verification.

1.1.3 Summary

The Materials and Radiation Effects branch of the Office of Fusion Energy has established a materials data book for use in fusion related studies. This handbook will be known *as* the Materials Handbook for Fusion Energy Systems and initial copies should be available in the near future. The handbook will be part of the Analysis and Evaluation subtask group of ADIP and will establish the data requirements and priorities for the preparation of the individual data sheets. At the present time Analysis and Evaluation subtask group has given the data sheets to support the ETF study the first priority. Based on recommendations from R. E. Nygren (ETF-Materials) the first data sheets will be those relating to the austenitic stainless steels.

1.1.4 Progress and Status

At the last two ADIP task group meetings the concept of creating a handbook containing materials data specifically devoted for use in near term and long range conceptual fusion reactor designs was introduced and discussed. The concept has now reached fruition and will be known as the Materials Handbook for Fusion Energy Systems (MHFES). The handbook will be similar in format to the Nuclear Systems Materials Handbook (NSMH) and will be published by the same organization (Hanford Engineering Development Laboratory) that distributes the NSMH. However, this

handbook is not intended to be a replacement to the NSMH but rather to compliment it and in many cases will directly reference entries in the NSMH. The primary objective of the MHFES will be to provide an authoritative and consistent source of material property data for use by the fusion energy community in concept evaluation, design, safety analysis, and performance/verification of various fusion energy systems. Initially the handbook will concentrate on structural materials used in the first wall and blanket structure. Later it will be expanded to include other components in the blanket usch as neutron multipliers, coolants, and tritium breeders. Ultimately the handbook should cover other reactor components such as magnets, plasma heaters (RF and neutral beam), divertors, limiters, shields, and other vital materials used outside the first wall and blanket region.

The handbook will be part of the Analysis and Evaluation Subtask group of ADIP and will receive its technical direction from this group. Current plans call for the Analysis and Evaluation subtask group to document the data needs form the ADIP organization and also from the various design projects such as ETF and Starfire (Commercial Tokamak). As other design projects reach maturity, such as mirror or EBT, etc., their data needs will also be included. Using these inputs the subtask group will then establish the data needs along with the priorities for the data sheets for inclusion in the handbook. The chairman of the handbook activity (J. W. Davis, McDonnell Douglas) will subsequently take these data priorities and in the case of structural materials for the first wall, request the appropriate working group or sub-working group to take the lead responsibility for preparation of the data sheets. For example, preparation of data sheets relating to the austenitic stainless steel would be handled by the Path A alloy group which is part of the Alloy Development for near term applications subtask group. Another part of this subtask group are the martensitic stainless steels which have been designated as the Path E alloys and all data sheets relating to the martensitic steel would be handled by this working group. Preparation of the data sheets relating to the Path B alloys (nickel) and Path C alloys (niobium, vanadium, and titanium) would be handled by the

Alloy Development for long term applications subtask group. After receiving the various assignments on preparation of the data sheets the Chairman of the subtask group or appropriate working group identifies a key individual to take the lead responsibility for preparation of data sheets. This individual would be responsible for coordinating the preparation of the data sheets and preliminary review. The prepared data sheets are then sent to the Chairman of the handbook for coordination of the review and approval prior to release for inclusion in the handbook.

The Analysis and Evaluation subtask group is in the process of evaluating the various data needs of the design projects. They have however, identified a series of data needs for the ETF project. These data requirements all pertain to austenitic stainless steel and have been transmitted to the Path A alloy working group for implementation. As a result, the Path A alloys will be the first data sheets for inclusion in the handbook.

The handbook itself is well along in development. The covers have been ordered and received along with the tab dividers. The format has been established and some preliminary data sheets received. Therefore, as soon as the Path A alloy data sheets are prepared the handbook will be ready for release.

1.2 ASSESSMENT OF CYCLIC CREEP-FATIGUE LIFE OF FIKST-WALL STRUCTURAL MATEKIAL — K. C. Liu and M. L. Grossbeck (ORNL)

1.2.1 ADIP Task

Task No. I.A.l, Define Material Property Requirements and Make Structural Life Prediction.

1.2.2 Objective

The objective of this work is to identify materials engineering problem areas and needs as well as to assess the practical implementation of existing design rules and criteria for fusion reactor systems. Specific and basic materials property requirements for MFE applications will be identified for inclusion in a materials development and engineering test plan to provide essential information in support of MFE research and development effort.

1.2.3 Summary

Cyclic lifetimes for a fusion reactor first wall were independently evaluated with two methods: linear damage summation (LDS),[1] which is currently being employed for use in ASME high-temperature design Code Case N-47,[2] and strain-range partitioning (SRP),[3] which is being studied for inclusion in the design Code. Despite their diversity, results estimated with the two analytical techniques agreed reasonably well in several practical design situations. Furthermore, this excercise has reaffirmed our earlier finding that 20%-cold-worked type 316 stainless steel could be used as a fusion first-wall material meeting a 8 to 10 MW-year/m^2 lifetime goal for a neutron wall loading of about 2 MW/m^2 and a maximum temperature of about 500°C.

1.2.4 Progress and Status

1.2.4.1 Introduction

In an earlier report[4] we demonstrated a possible application of the strain-range partitioning method to lifetime estimates of a first wall of

a tokamak fusion reactor. Lack of high-cycle fatigue data for the material tested at the temperature and environment within the range of interest precluded making conclusions on the accuracy of the predicted results. Since strain-range partitioning is one of many available methods for assessing creep-fatigue damage, it would be valuable to compare results predicted by different methods but applied to the same design.

We are currently using linear damage summation lifetime analysis and examining the extent of cohesiveness in calculated results predicted by both LDS and SRP methods. To further broaden the investigation, the earlier assessment analysis has been expanded to include various wall thicknesses ranging from 1.5 to 3 mm. More accurate stress-strain curves for 20%-cold-worked type 316 stainless steel were used based on recent test data obtained at ORNL. Biaxial stress states expected to exist in the blanket during operation were considered through the use of Von ilises stress and strain measures tu interpret uniaxial test data.

1.2.4.2 Method of Assessment

The present method for assessing creep-fatigue damage, as set forth in Code Case N-47 of the *ASME Boiler and Pressure Vessel Code,* was based on the linear damage summation rule:

$$\sum_j (n/N_f)_j + \sum_k (t/T_r)_k \leq D \ , \qquad (1)$$

where

n = number of applied cycles under jth loading condition;

N_f = number of cycles to failure under the jth loading condition from the fatigue curves that include the effect of hold times, corresponding to the maximum metal temperature during cycle;

t = time duration of kth loading condition;

T_r = rupture time at a given stress intensity from the kth loading condition;

D = total creep-fatigue damage (no greater than unity, depending on the material used).

To estimate lifetime at failure, N_f is calculated from $N_f = 20N_d$, where N_d is determined from design Code fatigue curves. For conservatism

the same safety factor of 20 was used for the determination of N_e at the high-cycle range. The T_r values are obtained from average stress-rupture curves. For stainless steels (types 304 and 316) D is less than unity for some designs.

Fatigue life was predicted by using the interaction damage rule given by the SRP method as

$$\frac{1}{N_{pred}} = \frac{F_{pp}}{N_{pp}} + \frac{F_{pc}}{N_{pc}} + \frac{F_{cp}}{N_{cp}} + \frac{F_{cc}}{N_{cc}} , \tag{2}$$

where

N_{pred} = predicted life in cycles,

F_{pp} = $\Delta\varepsilon_{pp}/\Delta\varepsilon_{in}$,

F_{pc} = $\Delta\varepsilon_{pc}/\Delta\varepsilon_{in}$,

F_{cp} = $\Delta\varepsilon_{cp}/\Delta\varepsilon_{in}$,

F_{cc} = $\Delta\varepsilon_{cc}/\Delta\varepsilon_{in}$,

$\Delta\varepsilon_{in}$ = total inelastic strain range,

$\Delta\varepsilon_{pp}$ = tensile plastic strain reversed by compressive plastic strain,

$\Delta\varepsilon_{pc}$ = tensile plastic strain reversed by compressive creep strain,

$\Delta\varepsilon_{cp}$ = tensile creep strain reversed by compressive plastic strain,

$\Delta\varepsilon_{cc}$ = tensile creep strain reversed by compressive creep strain.

The values of N_{pp}, N_{pc}, N_{cp}, and N_{cc} are determined from the life relationships, which are generally expressed as

$$N_{ij} = A_{ij}(\Delta\varepsilon_{in}/D_i)^{-B_{ij}} , \tag{3}$$

in which A_{ij} and B_{ij} are material constants, and D_i is the appropriate creep (i = e) or tensile (i = p) true ductility, respectively, in percent.

In applying the life relationships in Eq. (3) to fusion reactor components, ductility values of the materials or the changes of the ductility in a changing environment must be considered. Irradiation under

the conditions anticipated for fusion reactors usually results in increased strength and reduced ductility. Accordingly, Eq. (2) has been modified to take advantage of the high initial ductility and to not unduly penalize the design of the system. In the absence of "*cp*" and "*cc*" components, this form can be expressed as

$$\frac{1}{N_{pred}} = \left(\frac{\Delta\varepsilon_{pp}}{0.31\ \Delta\varepsilon_{in}^{-0.67}} + \frac{\Delta\varepsilon_{pc}}{0.1\ \Delta\varepsilon_{in}^{-0.67}} \right) \int_0^{L_f} D_p^{1.67}\ \frac{dL}{L_f} \ , \tag{4}$$

where $D_p = \ln(\varepsilon_t + 1)$, with ε_t being the total engineering elongation, which is used because reduction of area values were not available.

1.2.4.3 Irradiation Effects

To implement the above analyses the **following** equations were used to approximate the engineering tensile ductility of 20%-cold-worked type 316 stainless steel[5,6] (ε_t is the percent total elongation, and L is the wall exposure in MW-year/m^2).

At 350°C,

$$\varepsilon_t = 13.0 - 5.79L, \text{ for } L < 3.2 \ ; \tag{5}$$

$$\varepsilon_t = 8.89 - 2.29L, \text{ for } L > 3.2 \ . \tag{6}$$

At 450°C,

$$\varepsilon_t = 17.0 - 3.7L, \text{ for } L < 3.2 \ ; \tag{7}$$

$$\varepsilon_t = \varepsilon_t(575°C), \text{ for } L > 3.2 \ . \tag{8}$$

At 575°C,

$$\varepsilon_t = 14.6 - 1.51L, \text{ for } L < 2.3 \ ; \tag{9}$$

$$\varepsilon_t = 27.2 - 6.91L, \text{ for } 2.3 < L < 3.2 \ ; \tag{10}$$

$$\varepsilon_t = 8.14 - 0.81L, \text{ for } 3.2 < L < 8.6 \ ; \tag{11}$$

$$\varepsilon_t = 2.52 - 0.16L, \text{ for } L > 8.6 \ . \tag{12}$$

It is important to note that three assumptions were postulated when the above relations were considered for use in the predictions of fatigue life:

1. The mechanisms of fatigue life reduction are similar in both high-helium and low-helium-containing irradiated materials. Therefore, fatigue life can be predicted solely on the basis of ductility.

2. The simulation of the fusion reactor environment is adequate despite the lack of the correct displacements per atom (dpa)-to-helium concentration ratio.

3. The postirradiation tensile ductilities are the same as in-reactor ductilities.

Comparison of low strain rate postirradiation tests with in-reactor irradiation creep tests has shown that stainless steels exhibit higher ductility when deformed in the reactor than out of it. We have therefore been conservative in neglecting this effect.

Another effect that has been neglected is irradiation strengthening. At low total cyclic strain ranges, where the elastic component is greater than the plastic component, increasing the ultimate strength by irradiation-induced hardening could well increase the fatigue life.[7] This effect was not considered in the analysis, and the failure to do so at the low total strain ranges considered could well introduce additional conservatism into the predicted cyclic lives.

For a detailed discussion on ductility reduction in fusion reactor environment simulation and its correlation with irradiation damage parameters, such as dpa and helium concentration, the reader is referred to ref. 8.

1.2.4.4 Method of Analysis

An infinitely large, thin plate made of 20%-cold-worked type 316 stainless steel, as shown in the insert of Fig. 1.2.1, was used as a generalized model of a fusion reactor first wall. One side of the wall is exposed to plasma radiation, and the other is cooled. To facilitate

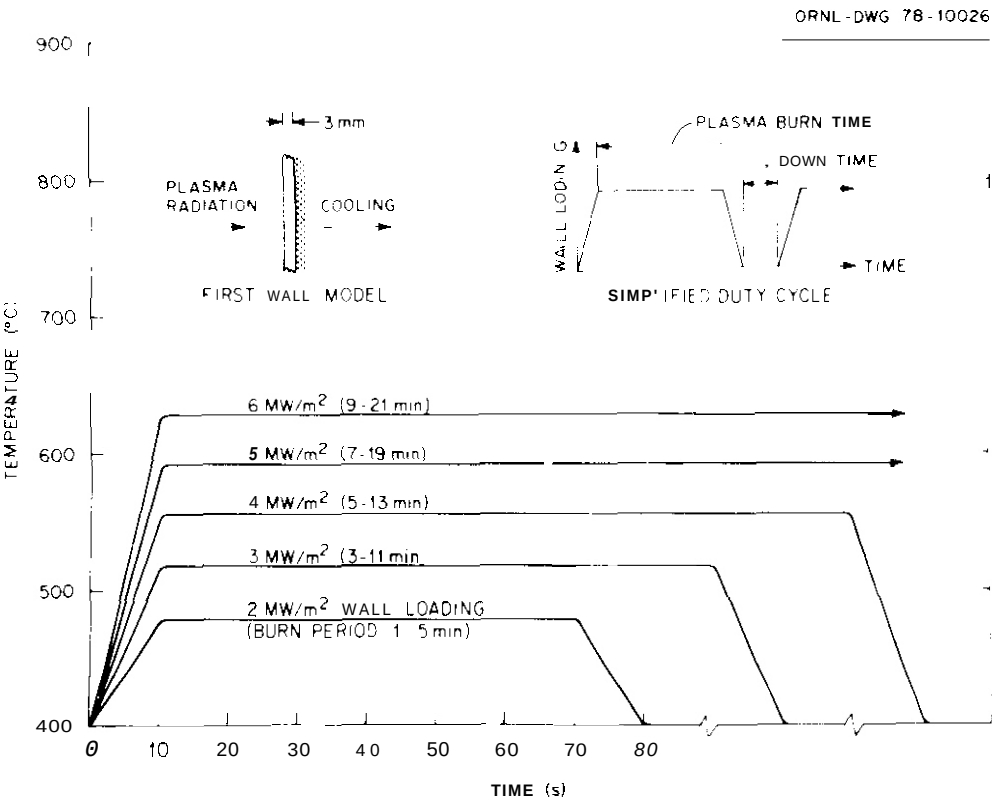

Fig. 1.2.1. Change of Temperature at Plasma Side of the First Wall Under Various Degrees of Neutron Wall Loading During Various Plasma Burn Periods.

thermal analysis we assume that the coolant inlet temperature is 300°C and that the outlet temperature is 500°C, with an averaging temperature of 400°C at the cold side of the first wall. Various types of radiation from the plasma deposit energy on the surface and the interior of the first wall. Neutron wall loadings of 2 to 5 MW/m^2 are considered here.

Since the heat is removed from the cold side of the wall, the temperature drops continuously through the wall thickness, and the gradient produces thermal stresses. Temperature traces were calculated for wall thicknesses of 1.5 to 3 mm by finite difference techniques. An example of one such calculation is given in Fig. 1.2.1.

We assume a simple on-off duty cycle with 95% burn time, as illustrated in Fig. 1.2.1. Since a longer plasma burn is more economical,

and burn time should increase as fusion technology improves, the duration assumed in the analysis increases progressively with neutron wall loading.

Stress-strain relations were derived from results of 20%-cold-worked type 316 stainless steel tested at ORNL. Yaterial constants and other information used in this analysis were obtained from ref. 9.

Thermal stress relaxation was calculated by using the creep equation €or unirradiated 20%-cold-worked type 316 stainless steel:[9]

$$\varepsilon = A\sigma \cosh^{-1}(1 + rt) + P\sigma^n t^m + Q\sigma^n t^{2.5} , \qquad (13)$$

where E is the hoop strain, r is the hoop stress, t is the time, and T is the temperature. The P, Q, A, P, n, and m values are functions of temperature. Equation (13) can he used for $\bar{\varepsilon}$ and $\bar{\sigma}$ by substituting E with $(\sqrt{3}/2)\bar{\varepsilon}$ and σ with $(2/\sqrt{3})\bar{\sigma}$. The stress relaxation rates are then:

$$\text{'Biaxial} = \frac{-\frac{1}{2}\left(\frac{\partial\bar{\varepsilon}}{\partial t}\right)}{\frac{1-\nu}{E} + \frac{\partial\bar{\varepsilon}}{\partial\bar{\sigma}}} , \qquad (14)$$

where E is the modulus of elasticity, and V is Poisson's ratio. Stress relaxation resulting from irradiation creep was calculated separately with the equation from ref. 9:

$$\dot{\bar{\varepsilon}} = \dot{\bar{\sigma}}\{(A\phi/\tau_{tr})\exp(-\phi t/\tau_{tr}) + DR\phi[1 - \exp(-\phi t/\Omega)] + B_0\phi\} , \qquad (15)$$

where ϕ is the neutron flux in n/cm^2-s [>0.1 MeV(0.02 pJ)]; R is a function of T; and A, B_0, D, T_{tr}, and Ω are constants.

1.2.4.5 Discussion of Results

As discussed earlier, the development of methods €or estimating creep-fatigue damage is still in its infancy. Therefore, different methods commonly yield better predictions in different types of applications since

each method was developed from its own specialized concept with experimental data that were tailored €or the application. When two different methods are applied to the same design situation, as demonstrated here, predicted results (summarized in Table 1.2.1) may differ somewhat.

While absolute accuracy of the results predicted with the two analytical nethods remains unknown, their relative accuracy can be discussed. An examination of N_f data without radiation effects shows that calculated cyclic lifetimes by the two nethods applied to the same design condition agree to the same order of magnitude where the wall temperature is between 450 and 510°C. This is equivalent to a first wall with a thickness of 2 mm exposed to a neutron wall loading from 2 to 4 MW/m^2.

For a wall temperature below 450°C, the LDS method overestimates the cyclic fatigue life predicted by the SKP method. Obvious reasons are that strain cycling within the elastic range predicts a high-cycle life (N_f) at low temperature and a long rupture life (T_r) for a low holding stress. The long rupture life virtually nullifies the second term of Eq. (I), and the cyclic life is determined only by the first term. However, at temperatures above 550°C the LDS method underestimates the cyclic fatigue lives predicted by the SRP method. The creep-fatigue life in this case can become substantially lower since N_f and T_r are both low at higher temperature under high holding stress.

The duration of the plasma burn is influential to the outcome of the predictive SRP method. A longer hold time is evidently detrimental to the cyclic lifetime predicted by SRP. However, it is interesting to point out that the lifetimes expressed in total radiation exposure (MW-year/m2) remain virtually unchanged. The LDS method is less sensitive than the SKP method to each hold time at the plasma burn. Where the stress and temperature are low and creep is not significant, the cyclic lifetimes can be estimated by the LDS method without considering hold time.

Results of thermal stress analysis, as summarized in Table 1.2.1, show that the strain range introduced in the first wall during a full operating cycle will be about 0.05 to 0.3% for a neutron wall loading from 2 to 5 MW/m^2. While most design information is needed in the low strain range, the bulk of experimental data has been obtained for strain ranges

Table 1 Z 1 Predicted Cyclic Creep-Fatigue Lives for Fusion First Wall Using 20% Cold-Worked Type 316 Stainless Steel

Wall Loading (MW/m^2)	Maximum Wall Temperature (°C)	Effective Strain Range (%)	Duration of Plasma Burn (min)	Inelastic Strainrange Component $\Delta\varepsilon_{pe}$ (%)	Calculated Cyclic Lifetime Based on SRP Method: Without Radiation Effect (Cycles)	Calculated Cyclic Lifetime Based on SRP Method: With Radiation Effect (Cycles)	Lifetime $\left(\frac{MW\text{-}year}{m^2}\right)$	Maximum Thermal Stress (MPa)	Lifetime Based on LDS Method: Without Radiation Effects (Cycles)
					Wall Thickness = 1.5 mm				
			1	3.03×10^{-5}	3.78×10^{8}	2.63×10^{6}	10.00		
2	439	0.054	3	7.79×10^{-5}	7.99×10^{7}	6.99×10^{5}	7.99	89 4	2 10^{9}
			5	1.09×10^{-4}	4.66×10^{7}	4.08×10^{5}	7.77		
			3	1.97×10^{-4}	1.70×10^{7}	5.89×10^{5}	10.08		
3	4 8	0 0ΞW	7	3.14×10^{-4}	8.34×10^{6}	2.56×10^{5}	10.23	132 4	1 2 10^{Ξ}
			11	4.15×10^{-4}	5.47×10^{6}	1.63×10^{5}	10.21		
			5	9.34×10^{-4}	1.16×10^{6}	1.74×10^{5}	6.60		
4	4 7	0 108	9	1.22×10^{-3}	7.73×10^{5}	1.01×10^{5}	6.94	174 4	4 10^{6}
			13	1.47×10^{-3}	5.88×10^{5}	7.13×10^{4}	7.06		
			7	1.84×10^{-3}	3.64×10^{5}	7.93×10^{4}	5.27		
5	4 9	0 1 5	13	2.43×10^{-3}	2.39×10^{5}	4.56×10^{4}	5.64	Z 5 3	8 9 10^{5}
			19	2.29×10^{-3}	1.81×10^{5}	3.21×10^{4}	5.81		
					Wall Thickness = 2.0 mm				
			1	5.20×10^{-5}	1.54×10^{8}	3.11×10^{6}	11.83		
2	4 2	0 073	3	1.34×10^{-4}	3.22×10^{7}	9.32×10^{5}	10.63	1 9 0	2 10^{8}
			5	1.87×10^{-4}	1.89×10^{7}	5.53×10^{5}	10.52		
			3	3.74×10^{-4}	5.41×10^{6}	4.77×10^{5}	8.16		
3	<7Ξ	0 W09	7	5.89×10^{-4}	2.65×10^{6}	2.08×10^{5}	8.13	17 6	7 10^{6}
			11	7.56×10^{-4}	1.80×10^{6}	1.33×10^{5}	8.37		
			5	1.08×10^{-3}	8.82×10^{5}	1.59×10^{5}	6.06		
4	503	0 W46	9	1.44×10^{-3}	5.64×10^{5}	9.21×10^{4}	6.31	2 0 3	Z 9 10^{6}
			13	1.74×10^{-3}	4.22×10^{5}	6.50×10^{4}	6.43		
			7	2.51×10^{-3}	2.05×10^{5}	6.37×10^{4}	4.26		
5	5Z7	0 μΞ2	13	3.35×10^{-3}	1.31×10^{5}	3.64×10^{4}	4.50	Z83 1	1 10^{4}
			19	4.04×10^{-3}	9.79×10^{4}	2.56×10^{4}	4.63		

Table 1.2.1. (Continued)

Wall Loading (MW/m^2)	Maximum Wall Temperature (°C)	Effective Strain Range (%)	Duration of Plasma Burn (min)	Inelastic Strainrange Component $\Delta\varepsilon_{pe}$ (%)	Calculated Cyclic Lifetime Based on SRP Method: Without Radiation Effect (Cycles)	Calculated Cyclic Lifetime Based on SRP Method: With Radiation Effect (Cycles)	Lifetime $\left(\frac{MW\text{-}year}{m^2}\right)$	Maximum Thermal Stress (MPa)	Lifetime Based on LDS Method: Without Radiation Effects (Cycles)
					Wall Thickness = 2.5 mm				
			1	8.38×10^{-5}	6.62×10^{7}	2.61×10^{6}	9.91		
2	[illegible]	0 092	3	2.14×10^{-4}	1.38×10^{7}	7.89×10^{5}	8.97	148 6	6 10^{7}
			5	2.99×10^{-4}	8.13×10^{6}	4.68×10^{5}	8.91		
			3	6.40×10^{-4}	1.97×10^{6}	3.64×10^{5}	6.22		
3	4[illegible]	0 1[illegible]	7	1.03×10^{-3}	9.62×10^{5}	1.59×10^{5}	6.34	2[illegible] <	3 5 × 10^{5}
			11	1.31×10^{-3}	6.58×10^{5}	1.03×10^{5}	6.45		
			5	2.09×10^{-3}	2.68×10^{5}	9.97×10^{4}	3.79		
4	5[illegible]	[illegible] 3	9	2.77×10^{-3}	1.72×10^{5}	5.84×10^{4}	4.00	[illegible] 4 9	1 10^{4}
			13	3.32×10^{-3}	1.29×10^{5}	4.15×10^{4}	4.11		
			7	1.09×10^{-2}	1.54×10^{4}	1.45×10^{4}	0.96		
5	560	0 26	13	1.38×10^{-2}	1.05×10^{4}	9.45×10^{3}	1.17	34 5	1 2 [illegible]^{3}
			19	1.61×10^{-2}	8.27×10^{3}	7.24×10^{3}	1.31		
					Wall Thickness = 3.0 mm				
			1	1.29×10^{-4}	3.07×10^{7}	2.26×10^{6}	8.58		
2	480	0 [illegible]1	3	$3.33 \times 1-^{-4}$	6.42×10^{6}	6.79×10^{5}	7.76	1[illegible] 1	5 [illegible] 1[illegible]^{6}
			5	4.62×10^{-4}	3.76×10^{6}	4.04×10^{5}	7.68		
			3	1.11×10^{-3}	7.80×10^{5}	2.47×10^{5}	4.23		
3	51[illegible]	0 [illegible]6	7	1.72×10^{-3}	3.83×10^{5}	1.11×10^{5}	4.45	2[illegible] 4	8 4 [illegible]^{4}
			11	2.19×10^{-3}	2.62×10^{5}	7.26×10^{4}	4.56		
			5	6.62×10^{-3}	3.59×10^{4}	3.23×10^{4}	1.23		
4	555	0 21	9	8.51×10^{-3}	2.38×10^{4}	2.07×10^{4}	1.42	3 8 5	1 × [illegible]^{4}
			13	9.99×10^{-3}	1.84×10^{4}	1.56×10^{4}	1.54		
			7	3.66×10^{-2}	1.90×10^{3}	1.69×10^{3}	[illegible].17		
5	591	0.281	13	4.29×10^{-2}	1.46×10^{3}	1.25×10^{3}	[illegible].22	391 4	1 × 10^{3}
			19	4.73×10^{-2}	1.24×10^{3}	1.04×10^{3}	[illegible].26		

between 3.5 and 2.0%. In estimating the lifetimes by the LDS method, much of the design information was extrapolated outside the Code tables and figures. Our concern is whether the predictive method can he extended into the long-rupture-time and low-strain-range regimes.

A limited number of tests has shown that cyclic fatigue and creep-fatigue damage are influenced by test environment and by irradiation. A higher cyclic fatigue life by a factor of 3 to 10 is not uncommon for tests in vacuum when compared with tests in air. Although fusion reactors are to he operated in a vacuum, this positive effect was not exploited in this analysis for conservatism. Neutron radiation is usually a negative effect that appears to have an impact on the cyclic fatigue life. The interactions of cyclic loading with the developing irradiation microstructures, including neutronically produced helium, are other uncertainties in the present analysis.

1.2.5 Conclusions

1. The lifetimes of fusion first walls with wall thicknesses of 1.5 to 3.0 mm were estimated for neutron wall loadings ranging from 2 to 5 MW/m^2 by using the Code-recommended linear damage summation (LDS) method and the strain-range partitioning (SRP) technique. The results predicted by the two techniques agreed reasonably well in many cases where the design conditions have been considered practical for 20%-cold-worked type 316 stainless steel to be used as a fusion first wall. Data used were those generated in air tests.

2. Results predicted by the SRP method are more conservative at low strain range and low temperature, whereas the LDS method is predicted to be more conservative at higher strain range and higher temperature.

3. Irradiation effects were included in the SRP method through the use of postirradiated tensile ductility. Results show that the neutron radiation is detrimental to the lifetime of the first wall.

4. Results independently predicted by the two methods tended to show that 20%-cold-worked type 316 stainless steel can be used as a first-wall material with an excess of 8 to 10 MW-year/m^2 lifetime in a vacuum for a neutron wall loading of 2 MW/m^2 and a maximum temperature of about 500°C.

1.2.6 References

1. L. F. Coffin, Jr., et al., *Time-Dependent Fatigue of Structural Alloys, A General Assessment* (1975), ORNL-5073 (January 1977).
2. "Code Case N-47 (1592-15), Class 1 Components in Elevated-Temperature Service," pp. 167-76 in *ASME Boiler and Pressure Vessel Code, Sect. 111, Div. 1,* The American Society of Mechanical Engineers, New York, 1977.
3. S. S. Manson, G. R. Halford, and M. H. Hirschberg, "Creep-Fatigue Analysis of Strainrange Partitioning, pp. 12-24 in *Proc. Symp. Design for Elevated Temperature Environment, 1st,* San Francisco, 1971.
4. K. C. Liu, C. R. Brinkman, and M. L. Grossbeck, "Assessment of Cyclic-Fatigue of First-Wall Structural Material," *ADIP Quart. Prog. Rep. Sept. 30, 1978,* DOE/ET-0058/3, pp. 5—15.
5. E. E. Bloom and F. W. Wiffen, "The Effects of a Large Concentration of Helium on the Mechanical Properties of Neutron Irradiated Stainless Steel," J. *Nucl. Mater.* 58: 171—84 (1975).
6. M. L. Grossbeck and P. J. Maziasz, "Tensile Properties of Type 316 Stainless Steel Irradiated in a Simulated Fusion Reactor Environment," *J. Nucl. Water. 85* & 86: 883—87 (1979).
7. D. J. Michel and G. E. Korth, "Effects of Irradiation on Fatigue and Crack Propagation in Austenitic Stainless Steels,'' pp. 117-37 in *Reactor Structural Materials,* M. L. Bleiberg and J. W. Bennett, Eds., The Metallurgical Society of AIME, New York, 1977.
8. C. R. Brinkman, K. C. Liu, and M. L. Grossbeck, "Estimates of Time-Dependent Fatigue Behavior of Type 316 Stainless Steel Subject to Irradiation Damage in Fast Breeder and Fusion Power Reactor Systems," pp. 490—510 in *Effects of Radiation on Structural Materials, Am. Soc. Test. Mater. Spec. Tech. Publ.* 683, American Society for Testing and Materials, Philadelphia, 1978.
9. *Nuclear Systems Material Yandbook,* Hanford Engineering Development Laboratory, TID 26666 (1975).

2. TEST MATRICES AND TEST METHODS DEVELOPMENT

2.1 INITIAL TEST RESULTS ON MINIATURE COMPACT TENSION FRACTURE TOUGHNESS SPECIMEN — F. H. Huang and G. L. Wire (Hanford Engineering Development Laboratory).

2.1.1 ADIP Task

Task 1.B.5.1 "Development Specimens and Test Methods"

2.1.2 Objective

The objective of this work is to evaluate the fracture toughness of HT-9 with a single specimen method. The electropotential technique has been developed to reduce the large number of specimens needed for a multi-specimen R-curve method. The work is aimed at characterizing the fracture behavior of fusion first wall materials.

2.1.3 Summary

Fracture toughness tests have been performed on miniature circular tension specimens of HT-9 at room temperature. The shape and size of specimens were tailored for efficient stacking in EBR-II irradiation. Furthermore, the number of specimens required will be reduced by using a single specimen method. The electropotential technique has been applied to obtain a calibration curve for voltage change versus crack extension. Using this calibration curve, J-integral measurements are made. They are in agreement with those from a multi-specimen method.

2.1.4 Progress and Status

2.1.4.1 Experimental Technique

Small and large test specimens were machined directly from as received HT-9 bar stock. The thermal-mechanical treatments of the alloy stock are 1050°C/30 min/AC + 780°C/ 2.5 hr/AC. Figure 2.1.1 shows the details of the processing of specimens machined from alloy stack. The schematic diagram of small HT-9 circular tension specimens (2.54 mm thick) is shown in Figure 2.1.2. The dimensions of 11.94 mm thick large specimens are doubled.

Specimens were fatigue precracked to 1.3 mm below a stress intensity factor of 28 $MPa\sqrt{m}$ using a servo-hydraulic MTS system.

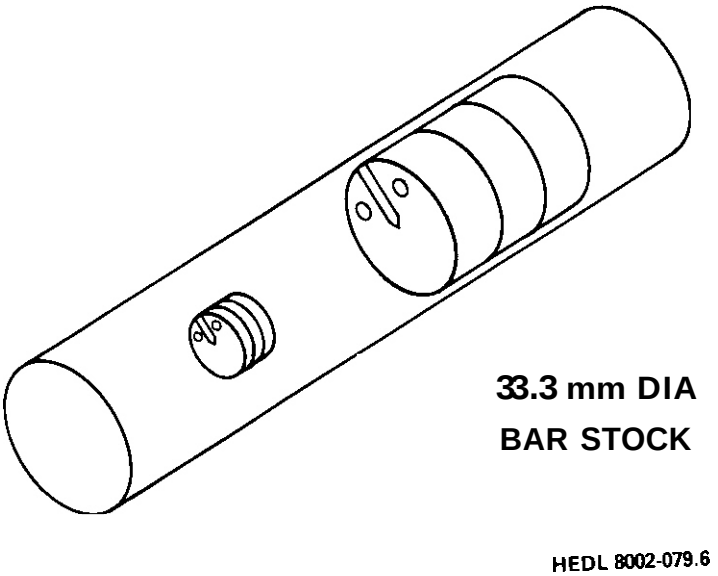

Fig. 2.1.1 Processing of HT-9 Specimens From Alloy Stock

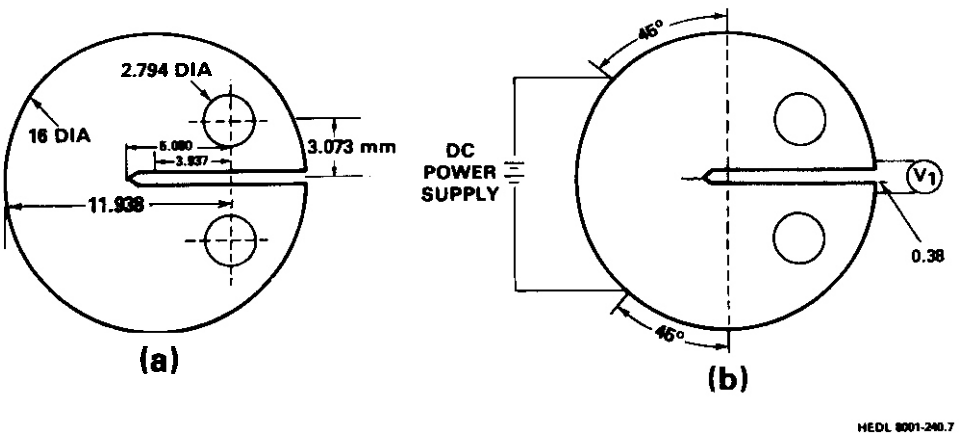

Fig. 2.1.2 (a) Circular Compact Test Specimens of HT-9
(b) Schematic Drawing of Electrical Potential Technique

An Instron testing machine was used to perform fracture toughness tests at room temperature. The values of J were calculated from load versus load-line displacement curves. Crack extension was revealed by heat tint Fig.2.1.3 and measured with a traveling microscope for the nultiple specimen method. During each test, the electropotential technique was applied to obtain continuous crack length measurements. Figure 2.1.2 shows the posi- of the current input and potential measurement leads.(1) A constant DC current of 15 amps was applied across the specimens, V_1 was measured using a microvoltmeter.

To calculate the values of J the following equation is used[2]

$$J = \frac{2A}{Bb}$$

where A is the area under load versus load-line displacement curve, B is specimen thickness, and b is unbroken ligament size.

1 mm

HEDL 8002-079.3

Fig. 2.1.3 Crack Extension as Revealed by Heat Treating for HT-9

2.1.4.2 Results and Discussion

The potential change versus load-line displacement for 2.54 mm thick HT-9 specimens is plotted in Figure 2.1.4. This smooth voltage curve is used to correlate crack extension through the parameters V_1/V_{10}, where V_{10} is the voltage measured for the initial crack length. The calibration curve for HT-9 circular specimens is shown in Fig. 2.1.5.

The J versus Δa curve derived for single specimens through the use of calibration curve are plotted in Figure 2.1.6 where the multiple specimen J-integral curve is also plotted for comparison. The figure shows that the J versus Δa curves obtained from both methods are in good agreement. The uncertainty in the calibration curve represented by dotted lines indicates that further work is needed to provide J versus Δa data at low crack extension.

Fracture toughness tests on large specimens were performed to study the thickness effect on fracture toughness. Typical load versus load-line displacement curve is shown in Figure 2.1.7. The large specimen fails by fast fracture with a straight crack front. The fracture surfaces of 0.1 inch thick and 0.47 inch thick specimens of HT-9 were examined by SEM as in Fig. 2.1.8. Cleavage facets are found to dominate the area immediately next to the stretch zone for both small and large specimens. However, the region away from the crack tip was made up of dimples and stepped features for small specimens. This is as expected because the constraint near the sharp crack formed by pre-cracking will be as high in the small sample as the large as long as the radius of curvature of the crack tip is very small compared to specimen dimensions. As the crack progresses and blunts in the thinner sample, the plane stress condition moves toward the center of the sample and constraint is reduced. However, the points for initiation of the crack motion constraint is high for both specimens.

If this reasoning is correct, crack propagation should begin at equivalent J values regardless of thickness. In fact,

$$K_{1J} = \sqrt{\frac{J_{1c}E}{1-\nu^2}}$$

was calculated to be 120 ksi $\sqrt{in}$ from the thin specimen J curve, and fracture

HT-9 CIRCULAR SPECIMEN

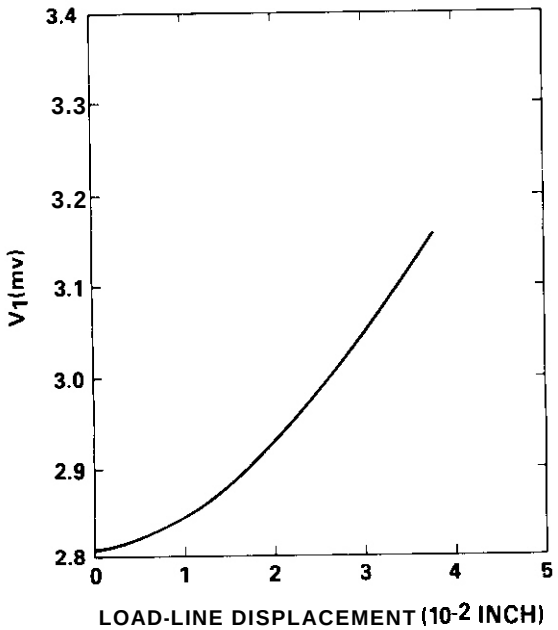

HEDL 8001 240 1

Fig. 2.1.4 Electrical Potential V Versus Load–Line Displacement for HT–9

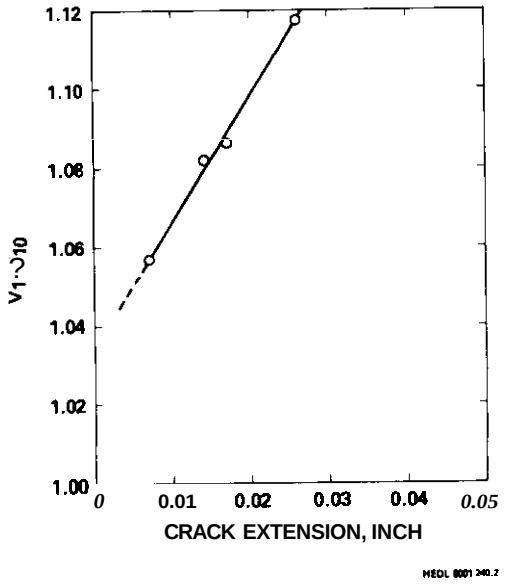

HEDL 8001 240.2

Fig. 2.1.5 Electrical Potential Calibration Curve for HT–9

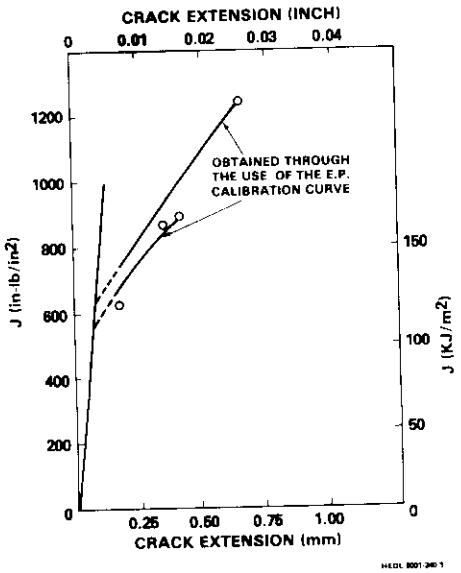

Fig. 2.1.6 J Versus Δa Tested at 25°C for HT-9

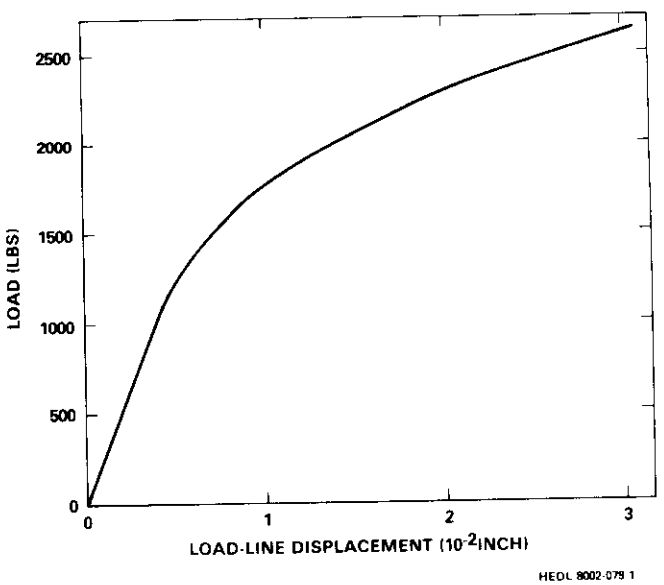

Fig. 2.1.7 Load Versus Load-Line Displacement Curve for 0.47 Inch Thick HT-9 Specimen

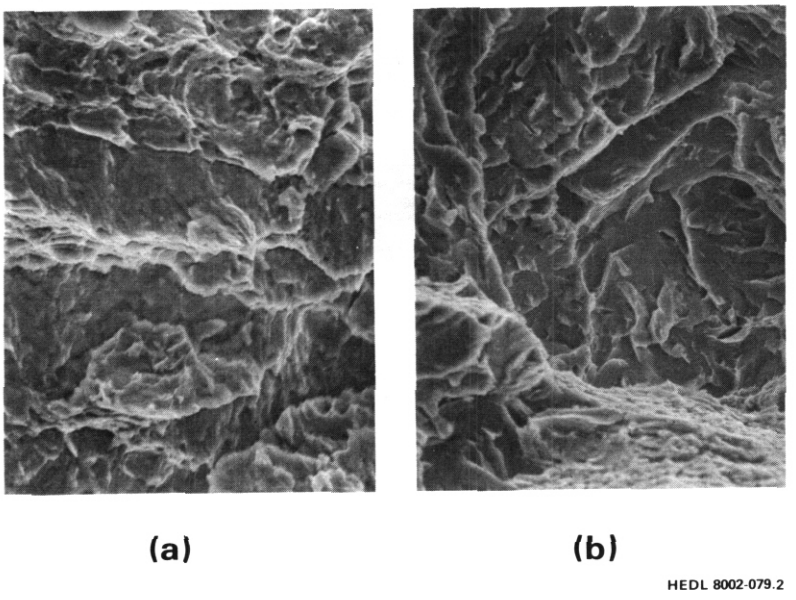

Fig. 2.1.8 SEM (1700X) for (a) 0.10 Inch Thick Specimen
(b) 0.47 Inch Thick Specimen

occurred in the thick specimen at K_{1J} ~114 ksi $\sqrt{in.}$ This result is very encouraging as it shows that the 0.1 inch specimen results can be utilized to describe fracture at higher constraints and thus results from these tests can be generalized.

2.1.5 Conclusions

Fracture toughness tests on HT-9 were performed on specimens designed for EBR-II irradiations at room temperature. The test results obtained through the use of electropotential techniques are in good agreement with those obtained for the multi-specimen method. Using the electropotential technique the single specimen J-integral measurements can offer the possibility of reducing the number of test specimens required for irradiation testing by a factor of five. This will enable a thorough study of irradiation environmental variables in the limited reactor space available for such tests.

2.1.6 References

1. F. H. Huang and G. L. Wire, "Techniques Developed for Elevated Temperature Fracture Toughness Testing of Irradiated Materials in Thin Sections," *J. Eng. Materials* and *Technol.* Vol 101, No. 4, 403 (1979).
2. J. R. Rice, P. C. Paris and J. G. Merkle, "Progress in Flow Growth and Fracture Toughness Testing," STP 536, American Society for Testing and Materials, 231 (1973).

3. PATH A ALLOY DEVELOPMENT – AUSTENITIC STAINLESS STEELS

3.1 THE INFLUENCE OF IRRADIATION ON THE PROPERTIES OF PATH A ALLOY WELDMENTS — F. W. Wiffen (ORNL)

3.1.1 ADIP Task

ADIP Task 1.5.13, Tensile Properties of Austenitic Alloys.

3.1.2 Objective

This work will determine the response of welds and weld-affected zones to irradiation over a range of temperatures and fluences. Welds with type 316 or 16-8-2 stainless steel filler metal joining 20%-cold-worked type 316 base metal are being irradiated in the Oak Ridge Research Reactor (ORR) and High Flux Isotope Reactor (HFIK). Tensile tests to determine the effects of irradiation on the mechanical properties of the irradiated specimens will be supplemented by fractography, metallography, and microscopy.

3. I. 3 Summary

Weldments of type 316 stainless steel joining 20%-cold-worked type 316 stainless steel base metal have been irradiated in the HFIK over the temperature range 280 to 620°C. Fluences up to 1.3×10^{26} n/m^2 [>0.1 MeV (0.02 pJ)] produced 5.3 to 9.8 dpa and 170 to 480 at. ppm He. Tensile tests at temperatures near the irradiation temperature showed strength values greater than those of unirradiated material for temperatures below 475°C but comparable with the unirradiated strengths for higher temperatures. Maximum elongation occurred at 475°C but was below unirradiated values for all irradiation conditions.

3.1.4 Progress and Status

Welds were prepared between sections of 6-mm-thick (0.25-in.) base metal plates of 20%-cold-worked type 316 stainless steel by using the gas tungsten-arc welding process. Weldments discussed in this report were made with type 316 filler metal. The specimens were machined from sections of material taken normal to the weld direction so that the specimen gage section contained both weldment and weld-affected material.

Specimens of type 316 weldment were irradiated in experiment HFIR-CTR-19 for 9.56 x 10^6 s (110.7 d) at full reactor power. Irradiation conditions are given in Table 3.1.1.

Additional details of weld specimen preparation and of the irradiation experiments have been reported previously.[1-3] The tensile properties of a similar series of experiments with 16-8-2 weldments have also been reported.[1]

The irradiated tensile specimens were tested at temperatures near the irradiation temperature. Tests were conducted in air at a strain rate of 4.6 × 10^{-5}/s (0.0028/min).

Fracture positions were located on all specimens by measurements on post-test photomacrographs and by comparison with preirradiation ferrite zone measurements used to locate the weldments. These measurements indicated that fractures in all specimens had occurred within the weldments.

Tensile test results on control and irradiated weldments are tabulated in Table 3.1.1. The data are also shown graphically in Fig. 3.1.1, with averages shown at temperatures where multiple tests were available. Stresses shown are engineering stresses, based on pretest specimen dimensions.

Specimens irradiated and tested throughout the range of temperatures of this experiment had yield strengths (YS) greater than those for the unirradiated controls. At 300°C the yield strength was nearly three times that of control material, but the strengthening decreased with increasing temperature until the irradiated strength was nearly equal to that of the unirradiated material at 625°C. The ultimate tensile strength (UTS) was greater than that of unirradiated material for temperatures from 300 to 425°C but was no greater than unirradiated values for temperatures from 475 to 625°C. Irradiation and testing at all temperatures in the ranges given led to elongation values lower than those in the control material. The maximum ductility occurred at 475°C, the temperature at which the irradiated and unirradiated strengths were most nearly equal.

The ultimate tensile strength and total elongation of the two weldment materials (data from ref. 1) and the base metal (data from refs. 4 and 5) for comparable irradiation conditions are shown in Fig. 3.1.2.

Table 3.1.1. Irradiation Conditions and Tensile Properties of Type 316 Stainless Steel Weldments Irradiated in the HFIR

Irradiation Conditions				Test Temperature (°C)	Tensile Properties[a]			
					Strength, MPa		Elongation, %	
Temperature (°C)	Fluence (>0.1 MeV) (n/m^2)	dpa	Helium[b] (at. ppm)		0.2% Yield	Ultimate	Uniform	Total
	control			35	350	603	19.5	23.1
	control			200	274	473	11.5	15.0
	control			300	238	443	11.0	15.8
	control			375	273	456	12.1	14.6
	control			475	211	481	16.3	19.1
	control			575	209	417	12.9	16.2
	control			625	206	358	9.9	14.3
284	0.71×10^{26}	5.3	174	300	675	694	1.6	5.4
374	1.06	7.9	343	375	643	668	1.2	4.0
374	1.05	7.8	337	375	669	703	1.7	4.2
447[c]	0.89	6.7	258	425	569	625	1.7	4.7
497[c]	0.72	5.3	178	475	333	506	6.8	9.1
466	0.89	6.7	259	475	341	500	7.3	9.2
473	1.29	9.6	462	475	235	476	7.9	10.2
473	1.28	9.6	461	475	313	490	9.5	11.3
564	1.19	8.9	412	575	275	376	3.8	4.3
564	1.19	8.9	410	575	238	416	7.5	8.3
620	1.32	9.8	480	625	208	320	2.6	4.0

[a]Strain rate = 4.6×10^{-5}/s (0.0028/min).

[b]Both weld and base metal are 13.5 wt % Ni.

[c]Irradiation temperature uncertainty greater than other ws a r⊛swlt of in experiment assembly.

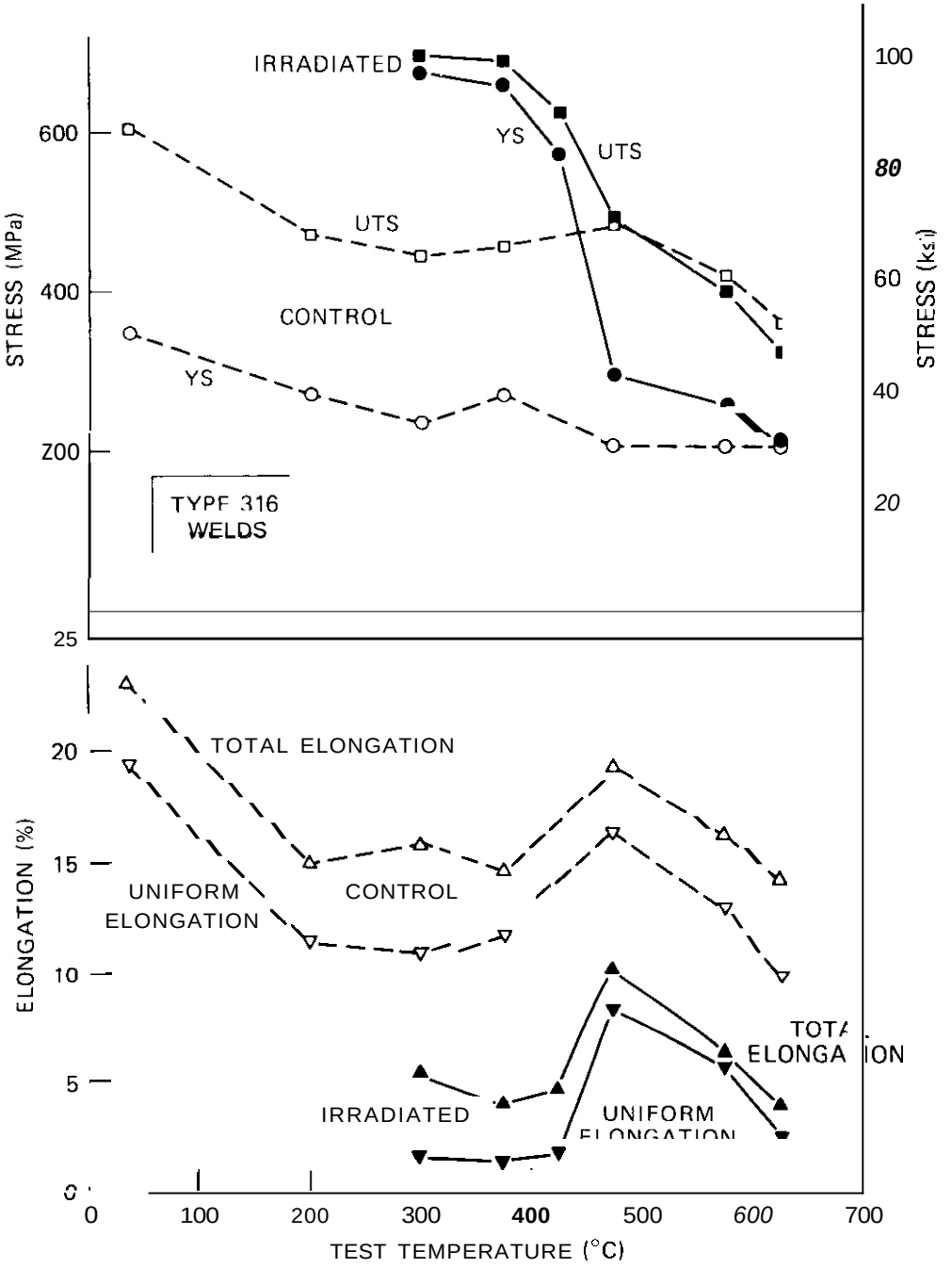

Fig. 3.1.1. Tensile Properties of Type 316 Weldments Irradiated in the HFIR. Specimens were irradiated at temperatures near the test temperature to fluences producing 5.3 to 9.8 dpa and 170 to *480* at. ppm He in the weldments and in the base metal. The strain rate is *4.6* × 10^{-5}/s (0.0028/min). Average data are plotted at several temperatures (see Table 3.1.1).

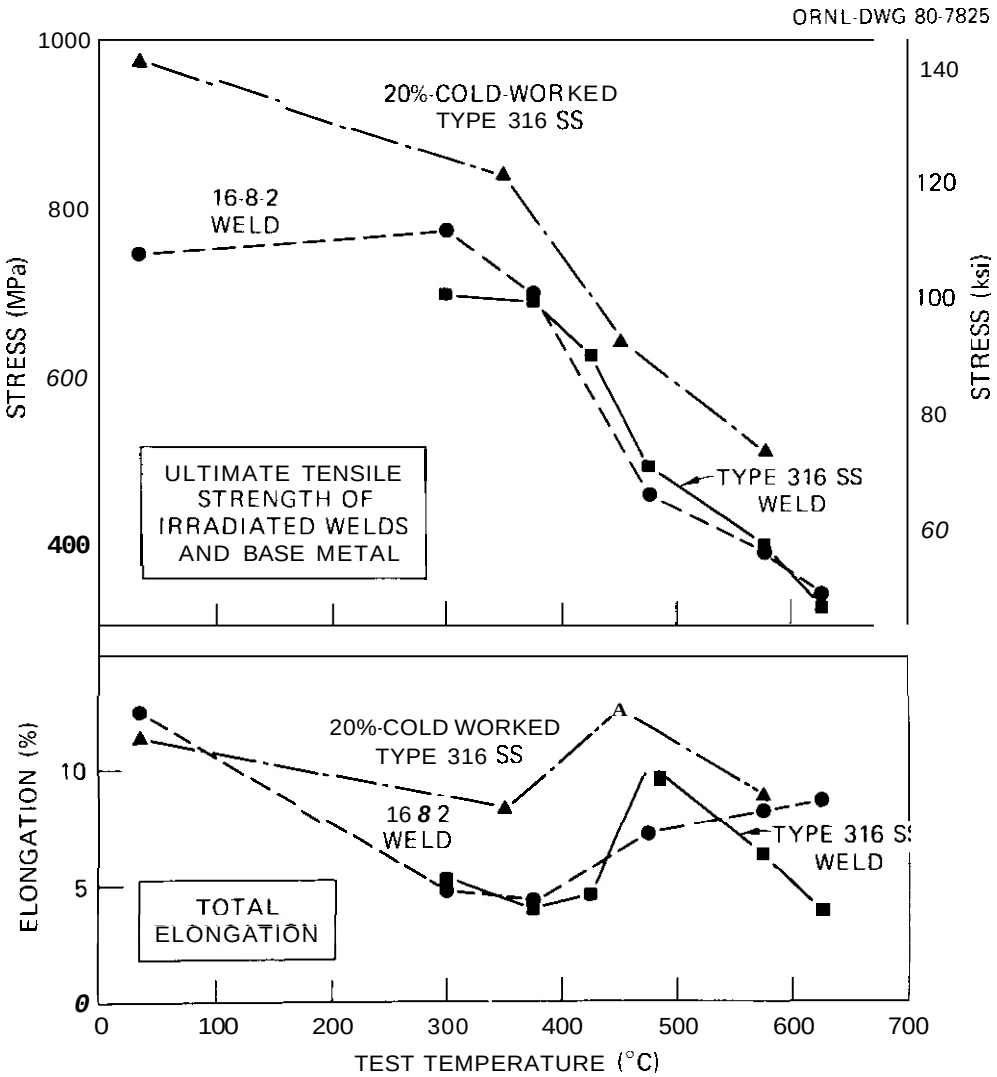

Fig. 3.1.2. A Comparison of the Ultimate Tensile Strength and Total Elongation of Two Irradiated Weldments and Irradiated Base Metal. Data on 16–8–2 welds are from ref. 1 and type 316 data are from refs. 4 and 5.

For the range of conditions examined, the strength of the irradiated 20%-cold-worked type 316 stainless steel base metal is greater than that for either weldment material. The two weldments show very similar strengths.

The type 316 base metal also has greater ductility than either of the weldments. The elongation values of the two weldments do show some differences. While the type 316 weldment shows decreasing elongation for increasing temperatures above 475°C, the 16–8–2 weldment shows the opposite trend.

3.1.5 Future Work

Scanning electron microscopy and optical metallography as necessary are planned to determine the fracture mode. Other work may be initiated, pending the outcome of fractography.

3.1.6 References

1. F. W. Wiffen, "The Influence of Irradiation on the Properties of Path A Alloy Weldments," *ADIP Quart. Prog. Rep. Sept. 30, 1979,* DOE/ET-0058/7, pp. 128–33.
2. F. W. Wiffen, D. P. Edmonds, J. F. King, and J. A. Horak, "The Influence of Irradiation on the Properties of Path A Alloy Weldments," *ADIP Quart. Prog. Rep. Mar. 31, 1978,* DOE/ET-0058/1, pp. *86–88.*
3. F. W. Wiffen, D. P. Edmonds, and J. F. King, "Influence of Irradiation on the Properties of Path A Alloy Weldments," *ADIP Quart. Prog. Rep. June 30, 1978,* DOE/ET-0058/2, pp. 47–53.
4. F. W. Wiffen, "The Effects of Irradiation at About 55°C on Type 316 Stainless Steel," *ADIP Quart. Prog. Rep. Mar. 31, 1978,* DOE/ET-0058/1, pp. 89–93.
5. M. L. Grossbeck and P. J. Maziasz, "Tensile Properties of Type 316 Stainless Steel Irradiated in a Simulated Fusion Reactor Environment," *J. Nucl. Mater. 85 & 86:* 883–87 (1979).

4. PATH B ALLOY DEVELOPMENT — HIGHER STRENGTH Fe–Ni–Cr ALLOYS

5. PATH C ALLOY DEVELOPMENT — REACTIVE AND REFRACTORY ALLOYS

5.1 MECHANICAL PROPERTY TESTING OF UNIRRADIATED PATH C ALLOYS — K. C. Liu (ORNL)

5.1.1 ADIP Task

ADIP Task I.B.3, Fatigue Crack Growth in Reactive and Refractory Alloys.

5.1.2 Objective

Fatigue and crack growth behavior are among the most important properties of an alloy to be used in a fusion reactor. There is essentially no information on these properties for refractory metal alloys. The objective of this work is to develop base-line information for the Path C refractory metal scoping alloys in the unirradiated condition.

5.1.3 Summary

Preparation for cyclic fatigue tests of vanadium-based alloys has been initiated. Appropriate heat treatments will be determined from the study of microstructures of the annealed samples. Strain-controlled fatigue tests of Nb—1% Zr are continuing. Additional test results show that Nb—1% Zr has only marginally better fatigue resistance than does 20%-cold-worked type 316 stainless steel tested in the low-cycle fatigue range.

5.1.4 Progress and Status

5.1.4.1 Heat Treatment and Specimen Preparation of Vanadium Alloys

Three vanadium-based alloys (V—20% Ti, V—15% Cr—5% Ti, and Vanstar-7) from the ADIP reference heats were received as 6.4-mm-diam bars (cold worked 80 to 90%) for use in cyclic fatigue testing. Microhardness tests were performed on the end cross section and lateral surface of the bar stock in the as-received condition. Table **5.1.1** shows the average values of five hardness tests examined on the respective locations as indicated. The hardness values on the end cross section are about 2 to 5% higher than those on the side, but these values all fall within the scatter of reported

Table 5.1.1. Average Hardness Values of Three Vanadium-Base Alloys

Alloy	Cold Work (%)	As-Received, DPH		Annealed,[a] End Cross Section, DPH
		End Cross Section	Side of Bar	
V–20% Ti	88	290	276	225
V–15% Cr–5% Ti	81	285	279	213
Vanstar-7	81	276	264	185

[a]Annealed 1 h at 1200°C.

values.[1] The high hardness values result from the cold work. Heat treatments to develop fully recrystallized microstructures are required for reproducible elevated-temperature testing.

Examinations of literature data concerning cold work, recovery, recrystallization, and grain growth of various vanadium-base alloys[1,2] indicate that full recrystallization occurs on annealing at a temperature of 900°C or greater. The grain size increases rapidly at temperatures above 1300°C. A heat treatment at a temperature between 1100 and 1300°C would probably yield a satisfactory result.

To determine the desired starting microstructures, a trial heat treatment at 1200°C for 1 h was conducted in a vacuum below 1 μPa. Hardness was then measured after the heat treatment and tabulated in Table 5.1.1. Comparisons between the values for cold-worked (as-received) and annealed materials show a reduction of hardness value on annealing from about 25% for the alloys with added titanium to 33% for Vanstar-7. Annealed values are also in good agreement with those reported in the literature for fully recrystallized material. Metallography is under way to verify that the heat treatment is adequate. Additional annealing temperatures of 1100°C for V–20% Ti and of 1300°C for Vanstar-7 will be compared with the above results.

5.1.4.2 Status of Cyclic Fatigue Testing of Nb–1% Zr

A matrix of 12 cyclic fatigue tests of Nb–1% Zr (not the ADIP heat) has been initiated following two sucessful exploratory tests. These tests

will be performed at four strain ranges: 21.0, 20.5, t0.3, and ±0.15% and at three temperatures: 25 (room temperature), 550, and 650°C. All specimens were heat-treated at 1400°C for 1 h in a vacuum below 1 μPa.

During this reporting period three cyclic fatigue tests were performed at room temperature in a vacuum below 1 μPa. Tests were controlled by the uniaxial strain, fully reversed in tension and compression at a strain rate of 0.004/s. A symmetric triangular function beginning with compression was used.

A test cycled to ±1.0% strain led to failure at 3308 cycles. A second test at ±0.5% strain registered 31,402 cycles at rupture. These data along with those generated in earlier exploratory tests are plotted in Fig. 5.1.1. To facilitate comparison the average data curve of 20%-cold-worked type 316 stainless steel is also shown in Fig. 5.1.1.

Comparisons show that Nb-1% data at room temperature are about the same or slightly better than those of stainless steel except for the data point at ±0.25%, which shows higher cyclic life than the average value by a factor of about 4. It should be noted that specimens used in exploratory tests were in the as-received (cold-worked) condition.

A test cycled to 20.3% strain was interrupted because of instrument failure at 26,899 cycles. Repair of the system is under way.

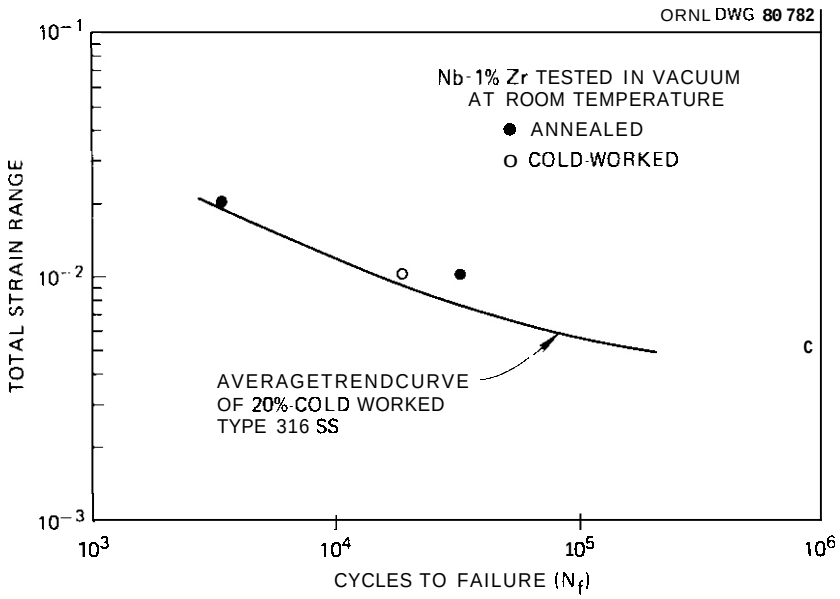

Fig. 5.1.1. Cyclic Fatigue Data of Nb-1% Zr Tested at Room Temperature and in Vacuum.

5.1.5 Conclusions

Limited test results from cyclic fatigue tests of Nb—1% Zr preclude making conclusions on fatigue behavior of the material as yet. However, it shows that Ntr-1% Zr is more fatigue resistant than 20%-cold-worked type 316 stainless steel tested at a high-cycle fatigue range.

5.1.6 References

1. R. E. Gold et al., *Technical Assessment of Vanadium–Base Alloys for Fusion Reactor Applications, Vol. II*, Westinghouse Electric Corporation, Pittsburgh, COO-4540-1 (April 1978).
2. G. A. Whitlow et al., *Vanadium Alloy Cladding Development*, Westinghouse Electric Corporation, Pittsburgh, WARD 3791-47 Final Report (November 1970).

5.2 MICROSTRUCTURE OF TITANIUM ALLOYS AFTER EBR-II IRRADIATION - J. W. Davis (McDonnell Douglas Astronautics Company - St. Louis) and S. M. L. Sastry (McDonnell Douglas Research Labs).

5.2.1 ADIP Task

Task Number 1.C.4 - Microstructure and Swelling in Reactive and Refractory Alloys (Path C).

5.2.2 Objective

To determine the response of titanium alloy microstructures to neutron irradiation.

5.2.3 Summary

Bulk annealing experiments performed on Ti-6A1-4V indicate that the beta precipitate observed, following irradiation, was dissolved after annealing for 24 hours at 650°C. The temperature where the precipitate dissolved was well below the beta transus and appears to support the contention that the precipitate is irradiation induced and not a result of supersaturation of the alpha phase. Instead the precipitate appears to be caused by the alpha solute seggregation at vacancy sinks. These sinks appear to act as traps for the vanadium atoms which have a high diffusion mobility as titanium because of its smaller atom size. The presence of a larger concentration of vanadium at the defect site results in alteration of the equilibrium concentration resulting in the precipitation of the beta phase. The near alpha alloys Ti-6242s and Ti-5621s use molybdenum as a beta stabilizer, however, because of its larger atom size and low concentration, it effectively suppresses the irradiation beta formation under these irradiation conditions.

5.2.4 Progress and Status

This work is a continuation of the study of irradiation titanium alloys. The specimens studied were part of a stress relaxation experiment performed by R. E. Nygren of HEDL.[1] The specimens were exposed in Row VII of EBR-II to a fluence of roughly 3×10^{21} n/cm^2 (E_n >0.1 MeV). The temperature during irradiation was maintained at 450°C $\pm$30. Subsequent

damage calculations performed by HEDL indicate that the titanium alloys received roughly 2.1 dpa's of damage. Examination of the samples after irradiation revealed a marked contrast between the alpha-beta alloy Ti-6Al-4V and the near alpha alloys Ti-6242s and Ti-5621s. Analysis of the Ti-6Al-4V microstructure revealed the presence of a fine precipitate of beta phase along with a high density of dislocation loops and debris. The precipitates, which are ellipsoidal in shape and roughly 100-200Å in size, obey the Burgers relationships and are found along low angle grain boundaries and along dislocations produced during the heat treatment (See Figure 5.2.1). Examination of the near alpha alloys, however, showed no evidence of the beta precipitate. The predominant features of the near alpha alloy defect structure are prismatic loops, stacking fault tetrahedra and spherically symmetrical defect clusters.

To determine the stability of the beta precipitates and to further understand the nature of the defect structure, a series of insitu and bulk annealing experiments were performed. The insitu annealing was accomplished by heating thin foils of Ti-6Al-4V and Ti-6242s on the hot stage of an electron microscope. Examination of the Ti-6Al-4V samples during heating revealed that for temperatures up to 500°C and exposure times of up to 10 minutes, no significant changes were observed in the defect microstructure other than a limited amount of defect annihilation. However, when the temperature was raised to 560°C there was a rapid annihilation of dislocation and dislocation loops which coalesced to form larger defects. Figure 5.2.2 shows the defect structure of the duplex annealed Ti-6Al-4V before and after annealing at 560°C. After annealing, the density of defects was considerably less than that of the as irradiated sample. However, the fine beta precipitate observed in the as irradiated specimen was still present after the insitu anneal.

Bulk annealing was accomplished by encapsulating the specimens in a quartz tube which was subsequently placed in an air furnace and soaked at temperature for 24 hours followed by air cooling to room temperature. Figure 5.2.3 shows the result of the bulk annealing experiments on the Ti-6Al-4V specimens. The results of annealing at 550°C are essentially the same as the 560°C insitu annealing experiment. However, increasing the bulk annealing temperature to 650°C resulted in the beta precipitate

13–3298

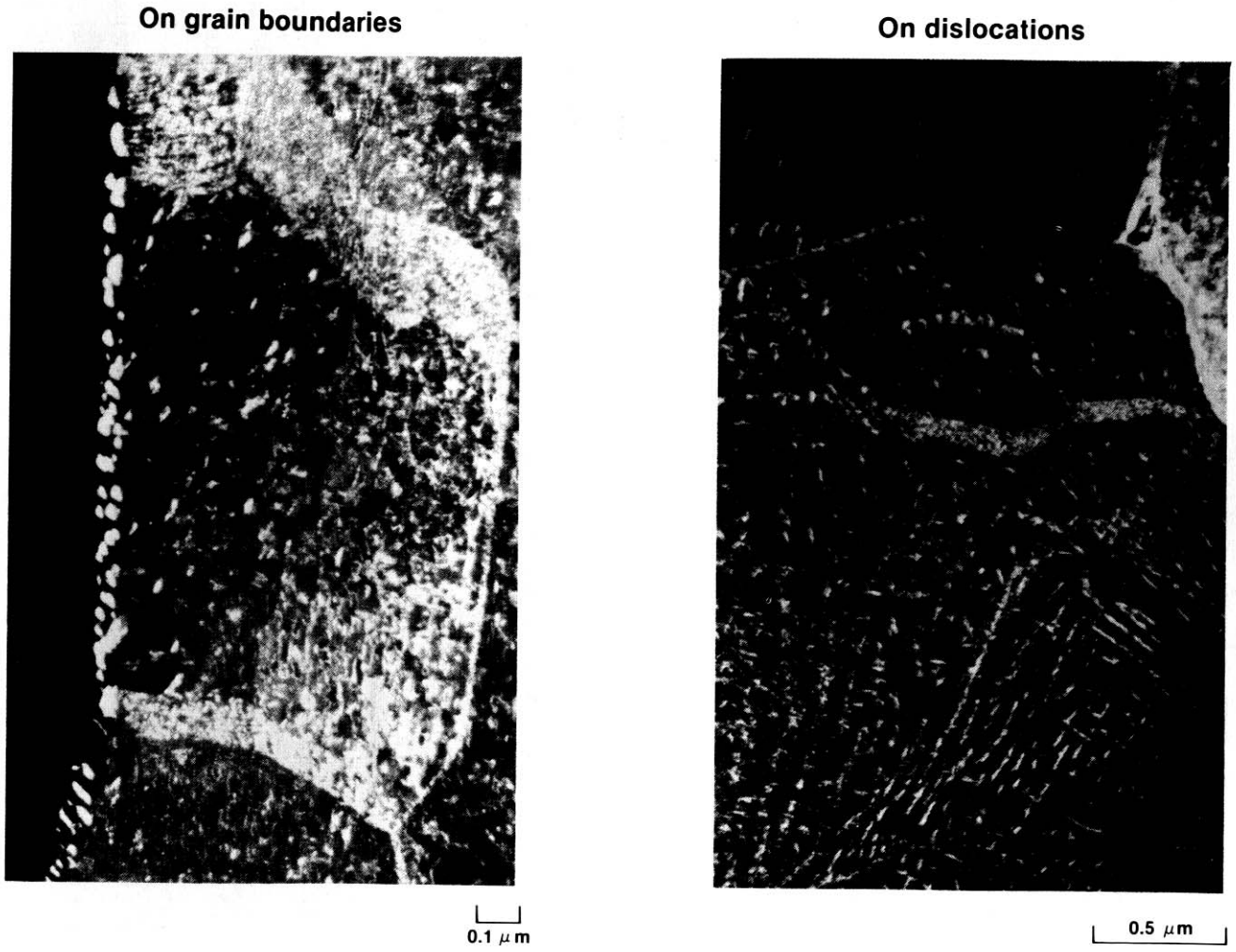

FIGURE 5.2.1 - PREFERENTIAL PRECIPITATION OF BETA IN IRRADIATED Ti-6Al-4V

13–3301

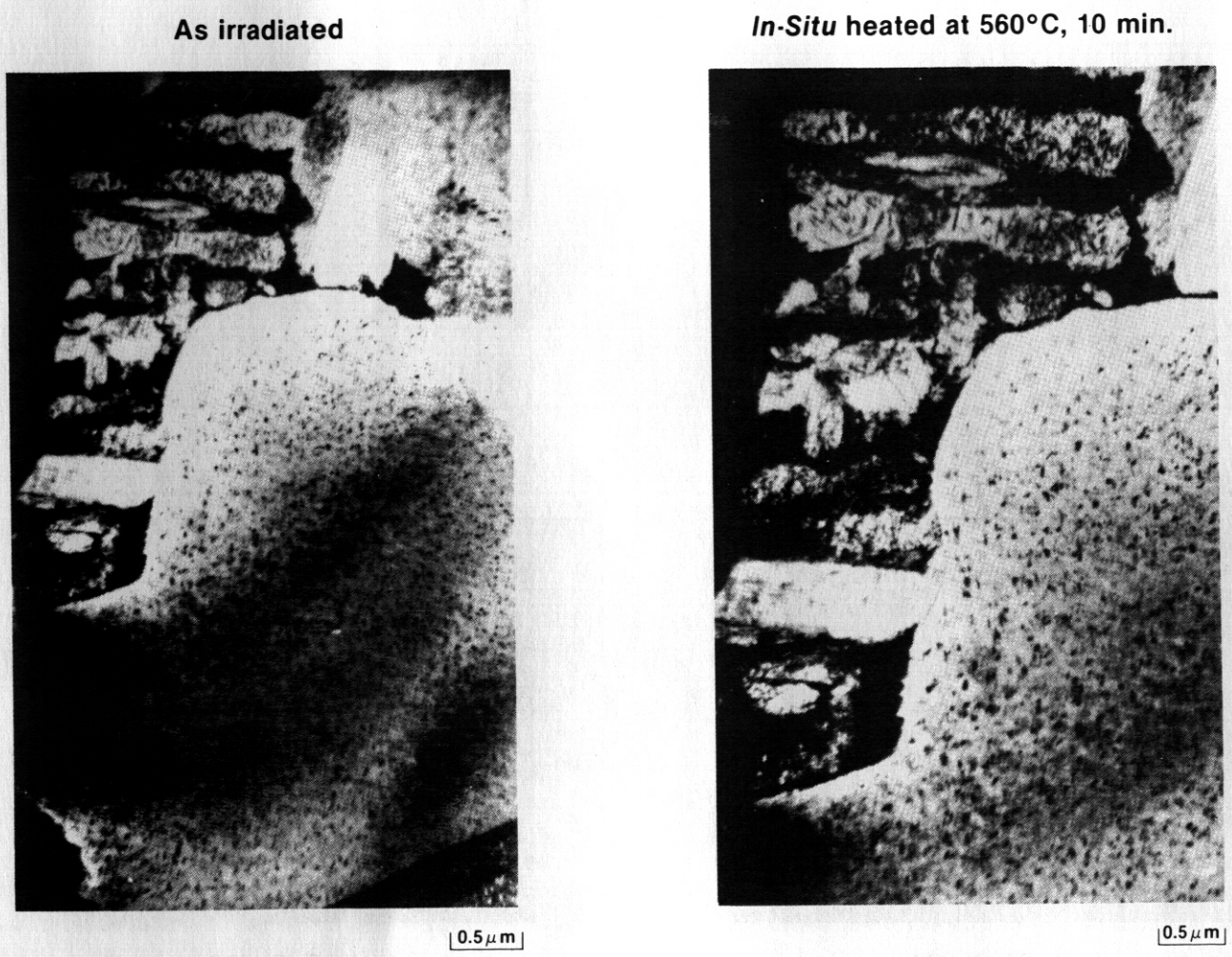

FIGURE 5.2.2 - ANNEALING OF DEFECT STRUCTURE IN IRRADIATED Ti-6Al-4V

13–3303

550°C, 24 h

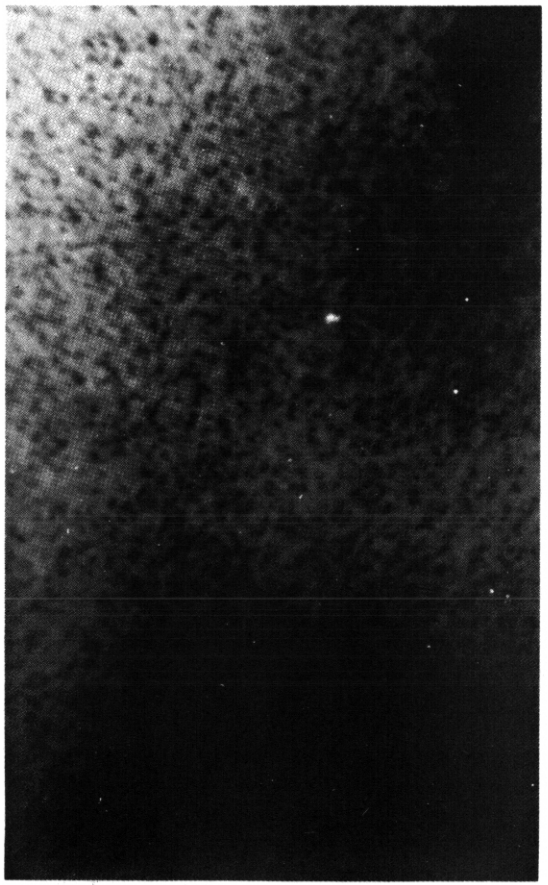

650°C, 24 h

FIGURE 5 Z 3 - ANNEALING OF DEFECT STRUCTURE IN IRRADIATED Ti-6Al-4V

dissolving. The temperature at which the precipitate dissolved is well below the beta transus and appears to confirm that the beta precipitate is radiation induced. It has been postulated that the precipitation of the beta phase was a result of supersaturation of the alpha phase of Ti-6Al-4V. However, examination of the phase diagram does not appear to support the supersaturation of vanadium in the alpha. Instead the precipitate appears to be a result of alpha solute segregation at vacancy sinks.

These sinks appear to act as traps for the vanadium atoms which have a high diffusion mobility due to its smaller atom size. The presence of a larger concentration of vanadium at the defect site results in an alteration of the equilibrium concentration resulting in the precipitation of beta. This contention appears to be supported by the observation of the precipit [illegible] angle grain boundaries. Upon anneali [illegible] and the vanadium atoms are free to migrate back to their original position resulting in the dislocation of the irradiation induced beta precipitate.

The near alpha alloys Ti-6242S and Ti-5621S are too lean in beta stabilizers to produce the bete precipitate. Observation of the microstructures after irradiation shows no preference for the precipitate. Subsequen [illegible] Ti-6242S at 550°C revealed no significant changes in defect structure (See Figure 5.2.4) and was essentially equ [illegible] easing the temperature [illegible] tructure. However, the results are not quite as dramatic as those observed in Ti-6Al-4V. The dislocation and dislocation loops have coalesced to form larger defects. Annealing at 750°C essentially resulted in complete annihiliation of the defects leaving a structure roughly equivalent to the unirradiated samples.

5.2.5 Conclusions and Future Work

This work essentially completes our analyses of the EBR-II irradiated titanium insofar as this irradiation is concerned. It is encouraging that no voids were observed but at this damage level voids are not observed in other materials either, and therefore the results are inconclusive until

13–3304

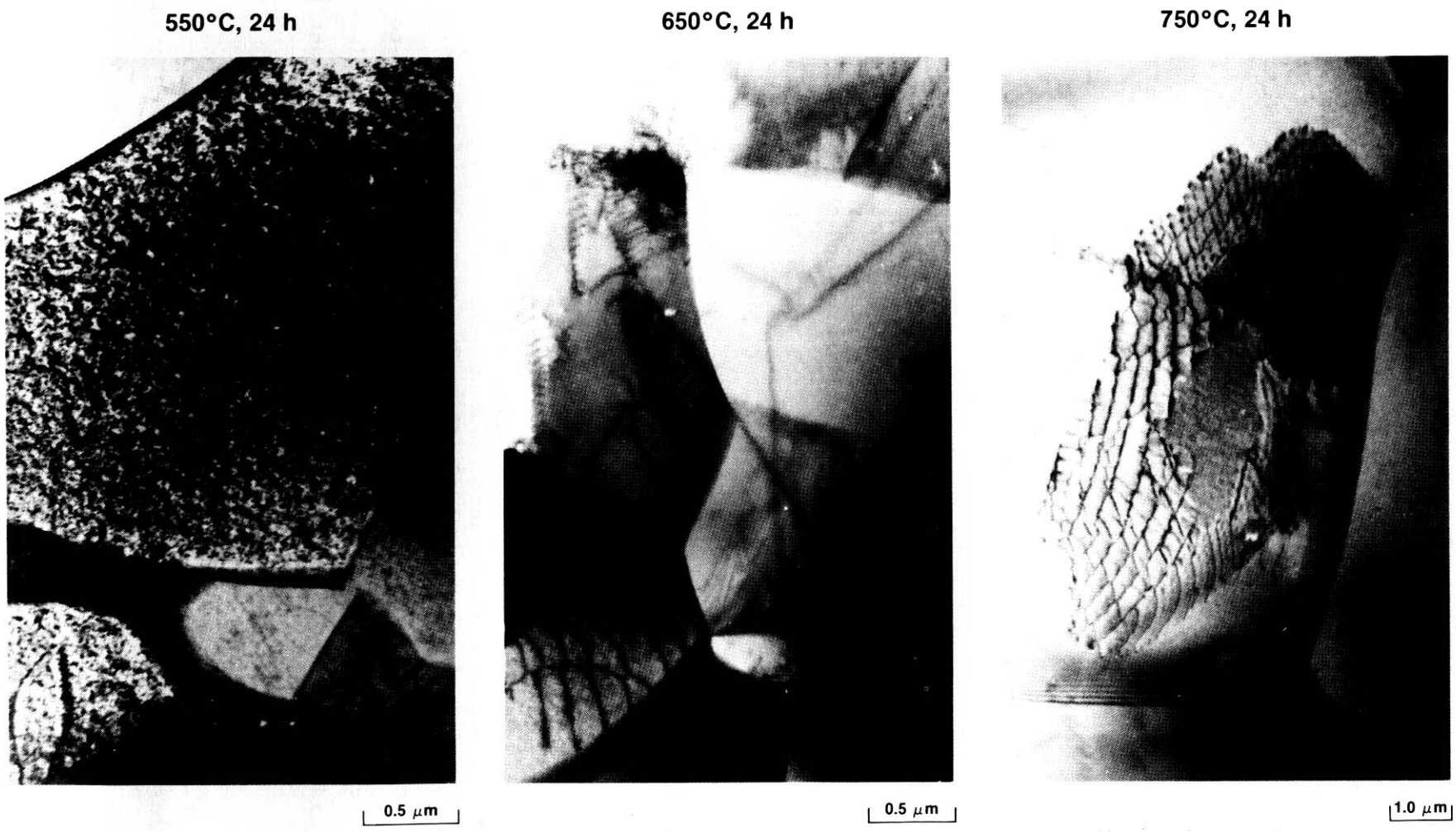

FIGURE 5.2.4 - ANNEALING OF DEFECT STRUCTURE IN IRRADIATED Ti-6242S

irradiations at higher damage levels are completed. A second irradiation of titanium alloys in EBR-II has been completed and the capsules sent to the hot cell for processing. These specimens should have roughly 33 dpa's of damage and should give a better perspective of the type of defects produced along with an indication as to whether or not titanium alloys are really resistant to radiation damages. We plan to examine these specimens when they are released from the hot cell.

5.2.5 References

1. R. E. Nygren, "Irradiation Creep Studies of Titanium Alloys" Journal of Nuclear Materials, Volumes 85 and 86, part B, 1979, pp 861–866.

5.3 EFFECT OF HYDROGEN ON FLAW GROWTH OF TITANIUM ALLOY Ti-6242s - G. W. Wille and P. S. Pao (McDonnell Douglas Astronautics Company - St. Louis).

5.3.1 ADIP Task

Task 1.B.3, Fatigue Crack Growth in Reactive/Refractory Alloys (Path C).

5.3.2 Objective

The objective of this study is to develop quantitative data to determine the effects of both internal and external hydrogen on fatigue crack growth of Ti-6242s alloy at temperatures and hydrogen pressures of interest for fusion reactors.

5.3.3 Summary

The planning of this study is complete. Modified wedge opening loading (modified WOL) specimens are being machined from 0.32 cm (0.125 inch) thick Ti-6242s. One half of the specimen blanks are being charged with hydrogen to a desired bulk level of 500 wppm with the hydrogen uniformly distributed throughout the samples.

5.3.4 Progress and Status

A review of effects of hydrogen on titanium alloys of interest for fusion reactors revealed a definite lack of pertinent information for the 10 to 10^{-1} Pa (10^{-1} to 10^{-3} torr) hydrogen pressures and 300 to 500°C temperatures expected in reactor.[1]

The existing data for hydrogen enhanced subcritical crack growth in titanium alloys is for low temperatures (less than 100°C) and relatively high hydrogen pressures 2 x 103 Pa (20 torr). It would be questionable to extrapolate the present data to the high temperature - low pressure regime predicted for fusion.

This task will perform a systematic study of the effect of both internal and external hydrogen on the fatigue behavior of Ti-6Al-2Sn-4Zr-2Mo-0.08Si (Ti-6242s) at temperatures to 500°C.

Ti-6242s was selected for evaluation because it is a high strength, creep resistant alloy that is included as an ADIP scoping alloy.

Internal hydrogen concentrations of approximately 50 and 500 wppm with external hydrogen test pressures from near zero to 10 Pa will be used to establish pressure dependence of crack growth and to study the combined effect of internal and external hydrogen on fatigue. The 500 wppm (23000 appm) is considered a realistic maximum equilibrium internal hydrogen concentration expected in reactor; 50 wppm (2300 appm) is an average concentration in commercial titanium alloys. Additional effects from external hydrogen, as perhaps added from plasma operation, will be evaluated by the external hydrogen pressure in the test chamber environment. Tests will be conducted at 27 to 500°C to determine the influence of temperature. Other variables to be examined are the frequency and R-ratio of the tests to ascertain that low or high strain rate effects are not overlooked.

The specimen design is shown in Figure 5.3.1. Charging of specimens with 500 wppm internal hydrogen is being performed by V. A. Maroni at Argonne National Laboratory.

5.3.5 Conclusions

1. Hydrogen charging and machining of the Ti-6242s specimens has begun.
2. Set up of the test equipment is in progress.

5.3.6 Reference

1. G. W. Wille, Hydrogen in Titanium Alloys, Section 5.4 of this ADIP report.

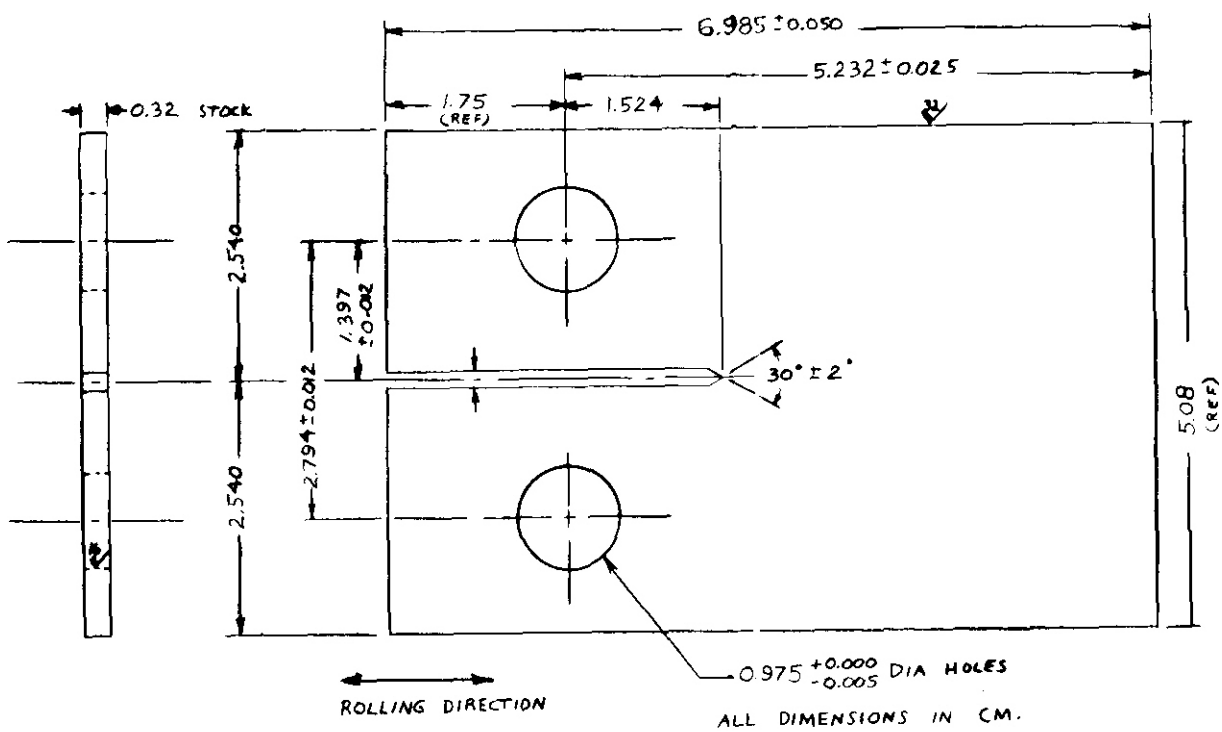

Fig. 5.3.1. Modified Wedge Opening Loading Specimen Design.

5.4 HYDROGEN IN TITANIUM ALLOYS – C. W. Wille (McDonnell Douglas Astronautics Company – St. Louis).

5.4.1 ADIP Task

ADIP Task I.A.I, Define material property requirements and make structural life predictions.

5.4.2 Objective

The objective of this task is to review and assess the current understanding of the effects of hydrogen on mechanical properties of titanium alloys being considered for use in fusion reactors; make predictions of the effects related to fusion reactor applications, where possible; and to identify areas where sufficient information is lacking.

5.4.3 Summary

A review of current knowledge concerning the effects of hydrogen on the mechanical properties of titanium has provided minimal data directly applicable to fusion reactor useage. Although no definite conclusions have been drawn as yet, it presently appears that because of the large number of interdependent variables associated with hydrogen interactions it may be impractical to predict with any degree of certainty the embrittlement effects, if any, for the alloys of interest for fusion energy. There are some indications that titanium alloys may not be adversely degraded in the elevated temperature, low hydrogen pressure conditions in the reactor.

5.4.4 Progress and Status

The potential effects of hydrogen on the mechanical properties of titanium and its alloys is of major concern to the fusion community for determination of the usefulness of titanium as a candidate material for first wall and blanket structures.

There are many papers discussing the potential degrading effects of hydrogen on titanium, with evidence that under certain conditions

there is a degradation of mechanical properties due to hydrogen. The most widely publicized is that of hydrogen embrittlement. The hydrogen embrittlement can effect either the impact properties or the normal tensile properties depending upon whether the titanium is single phase alpha or beta or an alpha-beta structure.

When one reviews the overall hydrogen embrittlement phenomena it becomes rather complex because the effects and reactions have many inter-dependent variables. The factors that appear to be most significant are the temperature dependence of the hydrogen solubility in alpha and beta titanium; the hydrogen partial pressure around the titanium; and the alloy composition. Other facets that enter into the embrittlement phenomena in more subtle ways are the relative amounts of alpha and beta phases present; the prior mechanical and thermal history of the material; the stress-state and loading rate; test temperature; and the amount of hydrogen present within the titanium as well as in the surrounding region.

The early investigations of hydrogen embrittlement dealt primarily with effects of internal hydrogen on room temperature properties of titanium and its alloys of interest in the 1950's. Since that time many investigations have been conducted to explain and predict the hydrogen embrittlement phenomena, however, the major portion of this data does not scope the conditions expected to exist in the fusion environment.

The early work on mechanical properties did not cover the alloys that are commercially available now and also tended to investigate higher pressure external hydrogen 10^5 Pa (760 torr), or greater, rather than the 10 to 10^{-1} Pa (10^{-1} to 10^{-3} torr) for fusion. The high pressure external hydrogen pressures would, at equilibrium, correspond to higher internal concentrations than anticipated in the first wall of the reactor. The work that was done with lower hydrogen pressures tended to be of either commercial or high purity titanium and not alloys of interest.

The fusion environment at the first wall blanket area is predicted to have operating temperatures of 300 to 600°C with hydrogen pressures of 10 to 10^{-1} Pa. The temperature of the blanket is not expected to fall

below perhaps 200°C after the reactor is in operation, therefore low or room temperature phenomena is not expected in reactor.

Look and Baskes[1] have performed calculations that predict hydrogen isotope concentrations in the first wall of approximately 1000 appm under proposed EPR and NUWMAK operating conditions. This value of 1000 appm corresponds to 22 wppm hydrogen, 44 wppm deuterium or 66 wppm tritium. These concentrations of hydrogen and its isotopes are well below the allowable maximum limit ot 150 wppm (6800 appm) hydrogen in present material specifications. Therefore, hydrogen at these predicted concentrations would not embrittle the titanium. However, other investigators believe that the hydrogen concentrations will be higher than 1000 appm. Davis and Smith[2] have predicted equilibrium D-T concentrations in titanium as shown in Table 1-1. The maximum concentration of 50,000 appm corresponds to 1100 wppm hydrogen. The 2700 wppm in the table is for a deuterium and tritium mixture.

Table 5.4.1 Equilibrium Hydrogen (D-T) concentration in Titanium resulting from interaction with D-T plasma

Parameter	Burn	Off-Cycle
Temperature °C	400	300
Hydrogen Pressure, Pa	10^{-3}	10^{-1}
D-T Concentration		
appm	1200	50,000
wppm	65	2,700

There is a limited amount of data that suggests that at elevated temperatures and low hydrogen pressures there may be no deleterious hydrogen damage to the titanium. The low hydrogen pressure in the reactor controls the absorption and solubility of hydrogen in the titanium. The 10^{-1} Pa hydrogen pressures would correspond to an approximate hydrogen content in titanium at 500°C of approximately 100 wppm. At this level, it is doubtful that hydrogen would degrade the mechanical properties.

A brief summary of the potential effects of hydrogen on titanium is given below. This is presented primarily as a review and not as predictions to susceptibility in the first wall.

Alpha titanium is susceptible to impact embrittlement, thus properties that are effected are those which are notch and/or strain rate sensitive. Hydrogen concentrations exceeding the solubility may cause a decrease in the notched impact strength, but effects of hydrogen diminish as strain-rate is decreased; normal tensile properties are only effected at relatively high hydrogen concentrations.

Alpha-beta alloys are susceptible to slow-strain-rate embrittlement, thus normal tensile properties may be adversely affected. Some tests indicate that at least for Ti-140A alloy (Ti-2Mo-2Fe-2Cr) the embrittlement effect disappears above 100°C. Tests with Ti-6Al-4V at 350°F have shown that higher (1000 vs. 0 ppm) hydrogen content increased the ultimate strength and had no effect on the elongation at strain rates of 0.05 to 0.005. The yield strength at 178°C was apparently increased by the 1000 ppm hydrogen when tested at 0.05 strain rate, whereas it decreased when tested at 0.005 strain rate.

Beta alloys are susceptible to changes in mechanical properties because of hydrogen. The effects are very dependent upon the composition of the alloy. For example, for a Ti-13.1 Mo alloy it was reported that impact and tensile properties were unaffected by a hydrogen concentration of 1900 wppm. Ti-3Al-8V-6Cr-4Mo-4Zr alloy showed an increase in yield stress and proportional limit at 27°C with increasing hydrogen concentration. Investigations on Beta I, VT 15, and Beta III alloys showed a decrease in elongation with increasing hydrogen concentrations; the amount necessary for embrittlement was dependent upon the alloy. The Beta III was not embrittled until a hydrogen concentration greater than 4000 ppm was reached. Also revealed in the same investigation was that Beta III was embrittled, as evidenced by a decrease in elongation, at hydrogen concentrations of less than 500 ppm when cathodically charged after solution heat treating at 850°C for 15 minutes and aging at 510°C for 8 hours. In sharp contrast to this, was the increase in elongation of Beta III at hydrogen concentrations up to 4000 ppm when the hydrogen was charged during aging at 510°C for 8 hours, as compared with cathodically charging after aging. This condition of charging during the aging process would very closely duplicate the expected mode

for entrance of hydrogen into the first wall blanket. This data is for room temperature and not the 300–500°C expected in service, however it does indicate that the Beta III may not embrittle under reactor environment.

Although there is much information concerning the effects of hydrogen on titanium, it became apparent that because of the large number of interdependent variables associated with the phenomena it is impractical to attempt to predict with any degree of certainty the embrittlement effects, if any, for the alloys of interest for fusion reactors.

5.4.5 Conclusions

At this time, no definite conclusions have been made. It is apparent that there is a definite lack of directly applicable data corresponding to the first wall environment.

5.4.6 Refernces

1. G. W. Look, and M. I. Baskes, Hydrogen Profiles in Tokamak Fusion Reactor First Walls. Journal of Nuclear Materials, Vol. 85 & 86 (1979) Part A, p. 995.
2. J. W. Davis, and D. L. Smith, The Impact of Hydrogen in a Fusion Reactor Environment on Titanium Alloys. Journal of Nuclear Materials, Vol. 85 & 86 (1979) Part A, p. 71.

5.5 EXAMINATION OF TITANIUM ALLOY SPECIMENS IRRADIATED IN EBR-II-

R. J. Puigh and E. K. Opperman (Hanford Engineering Development Laboratory).

5.5.1 ADIP Task

The Department of Energy (DOE)/Office of Fusion Energy (OFE) has cited the need for these data under the following ADIP Program Plan Tasks:[1] I.B.3, Fatigue Crack Growth in Reactive/Refractory Alloys (Path C); I.B.7, Stress/Strain Controlled Fatigue of Reactive/Refractory Alloys (Path C); I.B.15, Tensile Properties of Reactive/Refractory Alloys (Path C); I.C.4, Microstructures and Swelling in Reactive/Refractory Alloys (Path C); and I.C.8, Irradiation Creep of Reactive/Refractory Alloys (Path C).

5.5.2 Objective

The objective of the AD-1 irradiation experiment is to provide baseline, high-fluence data at several elevated temperatures on materials which have been suggested for the first wall of a fusion power reactor. Specifically, the experiment is designed to provide data concerning temperature and radiation effects upon mechanical properties such as fatigue, crack growth, tensile strength and creep. Characterization of the radiation effects upon microstructure and swelling will also be performed.

5.5.3 Summary

The AD-1 experiment consists of three uninstrumented pins containing microstructural and mechanical property specimens made from titanium alloys. These three pins were designed for irradiation temperatures of 394°C, 450°C and 500°C and have been irradiated in EBR-II until fluences greater than $4 \times 10^{22} n/cm^2$ (E>0.11 MeV) have been attained. Evidence of corrosion was observed on several specimens contained in the subcapsule designed for an irradiation temperature of 500°C. The subsequent opening of the other two subcapsules has been delayed until more information has been obtained concerning this corrosion.

5.5.4 Progress and Status

5.5.4.1 Introduction

Titanium alloys have been considered viable candidates for the first wall application in a fusion power reactor because they have a better strength to weight ratio and better thermal stress properties than found in stainless steel.[2] Also, the long term radioactivity of certain titanium alloys is very low which, therefore, allows the possibility of recycling the first wall material after storage times of less than 50 years.[3] Although titanium alloys appear to be promising because of the reasons outlined above, their relative resistance to radiation damage is unknown at the fluence and temperature levels expected in a fusion power reactor. To provide baseline data, the AD-1 experiment has been performed. EBR-II was chosen for the irradiation site because of its high flux and available irradiation volume.

5.5.4.2 Description of Experiment

The AD-1 experiment consists of three B-7c pins, each of which has been designed to contain one isothermal subcapsule. The desired irradiation temperature of each subcapsule is 394°C (742°F), 450°C (842°F), and 500°C (932°F), respectively. These irradiation temperatures are attained by profiling the gas gap between the subcapsule wall and B-7c pin wall in conjunction with the gamma heating profile in EBR-II to give a controlled heat flow. The maximum subcapsule temperature is recorded by thermal expansion device (TED) monitors located with the specimens inside the subcapsule. NaK is used as the subcapsule thermal bonding agent.

The alloys chosen for investigation in this experiment are given in Table 5.1.1. These alloys and their heat treatments have been recommended by ADIP for the Path C scoping studies.[4] Each subcapsule contains tensile strength, pressurized tube blanks (biaxial creep), Grodzenski fatigue, crack growth blanks, and transmission electron microscopy specimens. The specimen loadings for each level within the subcapsule are given in Table 5.1.2. Each of the three pins has the same level loadings. The test matrix for the AD-1 experiment is given in Table 5.1.3. In addition to the titanium alloys investigated in this experiment, each pin also contained

thirty (30) tensile strength specimens made from Fe-Cr-Ni ternary alloys which are being irradiated for the DAFS program.

The three pins were irradiated in EBR-II until goal fluences of $4 \times 10^{22} n/cm^2$ (E>0.1 MeV) were accumulated. The three pins are now at HEDL for specimen examination and postirradiation testing.

Table 5.5.1 Recommended Titanium Alloys and Heat Treatments for Scoping Studies

Alloy Designation	Composition % By Weight	Condition
Ti-6-4	Ti-6Al-4V	Mill Anneal (M)
		Duplex Anneal (D)
		Beta Anneal (B)
Ti-6242s	Ti-6Al-2Sn-4Zr-2Mo-0.09Si	Duplex Anneal
Ti-5621s	Ti-5Al-6Sn-2Zr-1Mo-0.25Si	Duplex Anneal
Ti-38644	Ti-3Al-8V-6Cr-2Mo-4Zr	Solution Treat & Age

5.5.4.3 Status of the Experiment

The three pins containing the titanium alloy specimens began their irradiation at EBR-II in August, 1978. Figure 5.1.1 shows the irradiation schedule which each pin underwent. All three pins were irradiated in a Row II position in EBR-II for cycles 96 through 98. Cycle 99 was missed. Because of the relatively low priority of the AD-1 experiment and limited available space, the pin designed for a subcapsule temperature of 394°C (742°F) was reinserted into a Row IV position for Cycles 100 through 102. The other two pins were reinserted into a Row II position for Cycles 100 through 103. Based upon calculations for the EBR-II core and test pin loadings, the fluences realized by the three pins are shown in Table 5.1.4.

All three pins have been returned to HEDL and the pin designed for an irradiation temperature of 500°C (932°F) has been opened. After cleaning the NaK from the specimens, evidence of corrosion of several of the specimens was observed. Opening of the other two pins and the subsequent testing of the titanium alloy specimens has been delayed until the nature of this corrosion is better understood.

Table 5.5.2

LEVEL LOADING FOR EACH PIN OF AD-1 IRRADIATION EXPERIMENT

	Level No.	Distance Between Center of Level and Core Midplane (in.)	Specific Alloy Loading
30T	0	7.80	30 Fe-Cr-Ni T
5P 5c 1TED	1	5.85	1-5 Condition P 1-5 Condition C
6P 5c	2	3.90	1-5 Condition P 1-T-6-4(B)P 1-5 Condition C
20F 2P	3	1.95	3-4 Condition F 4-2 Condition F 1 Ti-6-4(B)P 1 Ti-5621s P
16F 2D 1TED	4	0.0	3-4 Condition F 2-2 Condition F 2 Disc Packets
30T	5	-1.95	5-6 Condition T
30T	6	-3.90	5-6 Condtion T
5P 5c 1TED	7	-5.85	2 Ti 5621S P 2 Ti-6-4(D) P 1 Ti-6-4(B) P 2 Ti-6-4(D) C 1 Ti-6-4(B) C 1 Ti-5621s C 1 Ti-38644 C

*T = Tensile strength
F = Grodzenski fatigue
C = Crack growth blank
P = Pressurized tube blank
D = TEM disc packets containing 60 TEM discs

Table 5.5.3

TEST MATRIX FOR AD-1 IRRADIATION EXPERIMENT

Materials	Test Matrix* (394°C, 450°C,500°C)
Ti-6Al-4V (M)	10T, 6F, 2C, (3,3,2)P**, 10M
Ti-6Al-4V (D)	10T, 6F, 3C, 4P, 10M
Ti-6Al-4V (B)	10T, 6F, 3C, 5P, 10M
Ti-6242s (Dup)	10T, 6F, 2C, -, 10M
Ti-5621s (Dup)	10T, 6F, 3C, (5,5,6)P**, 10M
Ti-38644 (STA)	10T, 6F, 2C, 1P, 10M
Fe-Cr-Ni Ternary Alloys:	30T
Ni: 25-45%	
Cr: 7.5-20%	
Titanium Alloys:	60M
Al, Sn, V, Nb: 3-20%	

*Types of specimens:

T = Tensile strength
F = Grodzenski fatigue
C = Crack growth blanks
P = Pressurized tube blanks
M = TEM discs

**Numbers in parentheses correspond to number of pressurized tube blanks in each of the three pins (394°C, 450°C, and 500°C), respectively.

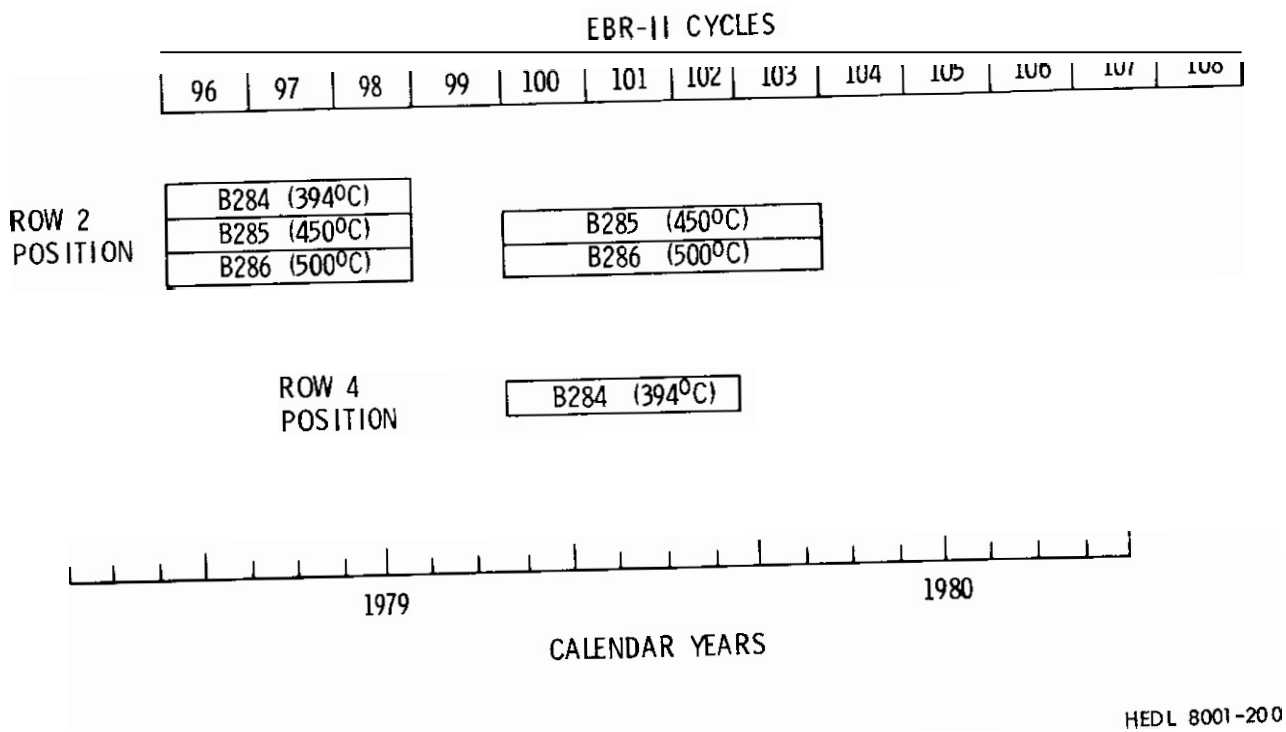
EBR-II CYCLES
96
97
98
99
100
101
102
103
104
105
106
107
108
ROW 2
POSITION
B284 (394°C)
B285 (450°C)
B286 (500°C)
B285 (450°C)
B286 (500°C)
ROW 4
POSITION
B284 (394°C)
1979
1980
CALENDAR YEARS
HEDL 8001-200

5.5.1 Ir e

Table 5.5.4 Fluences Attained in AD-1 Experiment

Pin Designation (Temperature)	Fluence* (n/cm^2, E>0.1 MeV
B284 (394°C)	4.2×10^{22}
B285 (450°C)	5.0×10^{22}
B286 (500°C)	5.0×10^{22}

*This is the maximum fluence at the core midplane and is based upon Pre-run and post run information provided by Argonne.

5.5.4.4 Investigation of Titanium Alloy Corrosion

The evidence for corrosion of the titanium alloy specimens was observed on all specimen types. Several specimens were found to be partially eroded. Other specimens such as tensile strength and Grodzenski fatigue specimens also exhibited "clean" fracturing of the specimen into two pieces. In most instances, the visible evidence for corrosion attack appeared to be very localized. For example, a majority of the tensile strength and Grodzenski fatigue specimens exhibiting evidence of corrosion were broken into two pieces. Each piece had smooth surfaces and sharp edges and only in the break region was there, in some instances, evidence for erosion corrosion.

An inventory of specimens was made after they were ultrasonically cleaned in an alcohol bath. For each titanium alloy, Table 5.1.5 lists the number of each type of specimen which exhibited evidence of corrosion. Also listed in Table 5.1.5, is the percentage of specimens lost in the experiment. As seen from this table, evidence of corrosion attack is most prevalent for the pressurized tube blanks which contain the thinnest material sections. One can also see from the table that all titanium alloys were effected. This would tend to rule out the possibility that the nature of the corrosion was associated with a particular phase of the titanium alloy. Also, none of the tensile strength specimens made from the Fe-Cr-Ni ternary alloys showed any evidence of corrosion.

After the inventory of the specimens had been made, three mechanisms for the observed corrosion were suggested. First, the specimens could have corroded in the sodium and potassium hydroxide solutions formed in the cleaning process to remove the NaK from the specimens. This cleaning

Table 5.5.5

SPECIMEN INVENTORY OF
500°C (932°F) PIN FROM AD-1 EXPERIMENT

Alloy	Specimen Loading*	No. of 'Good' Specimens**	% of Specimens Lost
Ti-6Al-4V	11P	6P	45%
	30T	24T	20%
	18F	18F	0%
	8C	6C	25%
Ti-6242s	-P	-P	-
	10T	9T	10%
	6F	4F	33%
	2c	1C	50%
Ti-5621s	6P	3P	50%
	10T	8T	20%
	6F	5F	17%
	3c	3c	0%
Ti-38644	1P	0P	100%
	10T	7T	30%
	6F	5F	1%
	2C	2C	0%

*P = Pressurized tube blank, T = Tensile strength, F = Grodzenski fatigue
C = Crack growth blank.

**'Good' refers to specimens which do not exhibit any visible damage.

process involves passing argon gas mixed with water vapor over the specimens and NaK which have been placed in a surgical pan. The argon gas plus water vapor mixture is brought into the cell and onto the specimens in a plastic tube. There is considerable water condensation along the tube walls which leads to water drops also being added to the specimens and NaK. The reaction is very active and lasts approximately one-half hour. At the end of this time, the specimens are in a very basic solution and are rinsed off with water.

To investigate the possibility of titanium alloy corrosion in the hydroxide solutions, the following experiments were performed. Mill annealed Ti-6Al-4V alloy rod stock was cut into 25 mil thick discs to be used as specimens. These specimens were weighed and then placed into varying concentrations of hydroxide solutions for exposure times as long as six hours. Sodium and potassium hydroxide solutions containing 5%, 10% and 50% by weight of anhydrous hydroxide with respect to water were investigated for solution temperatures from 60°C (140°F) to 80°C (176°F). Elevated temperatures were investigated since a large amount of heat is liberated in the reaction between the NaK and water. The most prolific reaction between the specimen and hydroxide solution occurred for the 5% and 10% solutions of KOH. In these reactions bubbles formed on the specimen surface for approximately one-half hour, then stopped. The weight of the specimen was found to increase a maximum of 0.2% in a *h* hour period for the 5% KOH solution. In this time period, the color of the specimen changed to a dark, dull gray. Based upon these observations, it appears that the predominant reaction is the oxidation of the material's surface. It is important to note that no erosion corrosion of the specimen was observed. Similar experiments were performed by McDonnel-Douglas Astronautics Company and they obtain qualitatively the same results.[5] It is, therefore, unlikely that the hydroxide solutions alone are responsible for the observed corrosion.

A second mechanism which has been suggested for the corrosion is the reaction of the NaK with water drops in the presence of the specimens. This mechanism is consistent with the observed localization of the

corrosion in many instances. In the caustic fusion of 73% anhydrous NaOH with pure titanium, the corrosion attack is reported to be greater than 50 mpy (mils per year) in the temperature range of 121–538°C.[6] It is not inconceivable that temperatures in the lower part of this range are achieved locally in the NaK reaction with water. Whether fused caustics are formed at this concentration in the reaction, is not clear at this time.

A third mechanism for the corrosion which has been suggested, is the corrosion of the specimens by the NaK in the subcapsule when the pin was in EBR-II. There is very little published information concerning the corrosion to titanium alloys by liquid alkalis. It is known that at temperatures above 598°C (1110°F) the corrosion rate for pure titanium in liquid Na is 2–20 mpy.[7] However, it is difficult to explain the localized attack observed in the specimens by this mechanism. One would expect, for this mechanism, a uniform attack of the specimens on all its surfaces exposed to NaK.

5.5.5 Conclusions

The three pins comprising the AD-1 experiment were irradiated at EBR-II for approximately one year and have been returned to HEDL for post-irradiation testing of the specimens. The subcapsule which is designed for an irradiation temperature of 500°C (932°F) has been opened and several specimens from this subcapsule have exhibited evidence of corrosion. Based upon chemical experiments which have been performed at HEDL and McDonald Douglas, the corrosion does not appear to be due solely to the hydroxide solutions formed in cleaning the NaK from the specimens. A more likely mechanism for the corrosion is the actual reaction of the NaK with water. However, the possibility of corrosion of the specimens by the NaK itself while the pin was at an elevated temperature in EBR-II or by some other mechanism cannot be ruled out at this time.

5.5.6 Future Work

The two other subcapsules of the AD-1 experiment need to be opened. The corrosion which has been observed does not appear to be due to the hydroxide solutions formed in cleaning the NaK from the specimens. The other mechanism which is involved in removing the specimens from the subcapsule and which may be responsible for the observed corrosion is the reaction of the NaK with the water. In order to minimize the possible corrosive effects of the NaK plus water reaction, the amount of NaK to be cleaned away from the specimens must be minimized. A procedure for accomplishing this has been developed. Once the specimens have been removed from the subcapsules and cleaned, postirradiation mecahnical testing of the specimens will be initiated.

The mechanism involved in the corrosion of several of the titanium alloy specimens must be understood. Metallography on the corroded specimens is planned. To investigate the possibility of corrosion of the specimens in the NaK environment within the subcapsule, three rings, 1/4 inch in length, have been cut from the subcapsule at vertical positions corresponding to the centers of levels 1, 4, and 7 given in Table 5.1.2. While the solubility of Ti in K is less than 4 ppm (parts per million) by weight at temperatures between 747°C (1377°F) and 1067°C (1953°F),[8] galvanic mass transfer between the specimens and the subcapsule wall is possible due to a temperature gradient between them. Diffusion of titanium into the inside wall of the subcapsule will be looked for using either an electron beam microprobe or a chemical etching technique. Also planned is an experiment where unirradiated titanium alloy is placed in NaK and then the NaK is reacted away using drops of water. Once the results of these tests are obtained, further investigation will proceed as required to understand the observed corrosion of specimens in the AD-1 experiment.

5.5.7 References

1. J. O. Stiegler, et al, "Alloy Development for Irradiation Performance," *The Fusion Reactor Materials Program Plan*, July, 1978.
2. J. W. Davis and G. L. Kulcinski, "Assessment of Titanium for Use in the First Wall/Blanket Structure of Fusion Power Reactors," *Elec-*

tric Power Research Institute, *EPRI-836 (Project 472-l)*, April, 1971.

3. J. W. Davis, G. L. Kulcinski, and T. Y. Sung, "Recycling Potential of Titanium Alloys," *ADIP Quarterly Report*, January-March, 1978.

4. J. W. Davis, "Selection of Titanium Alloys for Path C Scoping Studies," *ADIP Quarterly Report*, January-March, 1918.

5. Personal Communication, J. W. Davis, McDonnel-Douglas Astronautics Company - St. Louis, to R. J. Puigh, HEDL, January 16, 1980.

6. L. L. Shreir, *Corrosion*, published by George Newnes Ltd., Towne House, London, 1963, p *540.*

7. F. L. Laque and H. R. Copson, *Corrosion Resistance* of *Metals and Alloys*, published by the Reinhold Publishing Corporation, New York, 1963, p 659.

8. J. E. Draley and J. R. Weeks, *Corrosion* by *Liquid Metals*, published by Plenum Press, New York, 1970, p 609-610.

6. PATH D ALLOY DEVELOPMENT — INNOVATIVE MATERIAL CONCEPTS

6.1 DEVELOPMENT OF IRON-BASE ALLOYS WITH LONG-RANGE-ORDERED CRYSTAL STRUCTURE — C. T. Liu (ORNL)

6.1.1 ADIP Task

ADIP Task I.B.12, Stress-Rupture Properties of Special and Innovative Materials, and Task I.B.16, Tensile Properties of Special and Innovative Materials.

6.1.2 Objective

The objective of this study is to develop a unique class of high-temperature alloys — ductile long-range-ordered (LRO) alloys based on $(Fe,Ni)_3V$ and $(Fe,Ni,Co)_3V$ systems – and to evaluate their potential for use as structural materials for fusion energy systems. Samples of LRO alloys will be included in alloy development irradiation experiments to assess the effects of irradiation on tensile properties and stability.

6.1.3 Summary

A series of iron-base long-range-ordered (LRO) alloys with compositions $(Fe,Ni,Co)_3V$ are being developed for fusion energy applications. The alloys form a cubic ordered structure similar to $AuCu_3$ below their critical ordering temperature (T_c). The alloys in the ordered state are ductile, with total elongation in excess of 30% at room temperature. Tensile tests of the LRO alloys at elevated temperatures indicate an unusually attractive mechanical behavior. Their strength, instead of decreasing as with conventional alloys, increases with temperature because of ordering. The ordered alloys also exhibit excellent creep strength. Their creep rate at 650°C is lower than that of type 316 stainless steel by more than three orders of magnitude.

6.1.4 Progress and Status

6.1.4.1 Introduction

The structural material used for construction of the first wall in fusion energy systems requires good high-temperature mechancial properties, resistance to irradiation-induced degradation of properties, and good

compatibility with low-pressure hydrogen, lithium, and coolants.[1] To meet these requirements a wide variety of alloys based on Fe, Ni, Ti, V, and Nb are being studied as possible candidate materials. Alloys that form long-range order below a critical temperature (T_c) offer potential advantages over the conventional or disordered alloys for high-temperature fusion reactor applications.' This is because unusual dislocation motion characteristics of the ordered lattice provide the LRO alloys with excellent high-temperature strength and fatigue resistance. Also, kinetic processes involving diffusion, such as creep or migration of point defects, are reduced in the ordered lattice. It is thus possible that the alloys with LRO crystal structure can be more resistant to irradiation-induced property degradation.[3,4]

The main disadvantage that has limited the use of LRO alloys is their tendency to be brittle in the ordered state. However, our recent work[5] on cobalt-base ordered alloys with compositions $(Co,Fe,Ni)_3V$ has overcome this limitation. We have demonstrated that the ductility of the ordered alloys can be controlled by adjusting the compositions and the ordered crystal structure. The alloys with cubic ordered structure have more than 30% elongation at room temperature. For fusion reactor applications lowering the cobalt content (<25%) may be advantageous because of its high neutron absorption cross section, which lowers the tritium breeding rate. In this study the alloy compositions are modified for fusion energy applications for temperatures up to 700°C.

6.1.4.2 Alloy Preparation and Fabrication

A series of ordered alloys was prepared with base compositions of Fe_3V, where Fe is partially replaced with Ni and Co. These were substitued to raise T_c and control the ordered structure. Table 6.1.1 lists the nominal composition of the alloys we prepared.

The alloys LRO-15, -16, -17, and -20 were prepared by arc melting or electron-beam melting and drop casting into a 25 by 13 by 140-mm rectangular mold. The ingots were clad in molybdenum cover sheets and rolled to a total reduction of 80% at 1100°C. After breakdown by hot rolling, the alloy plates were cold rolled from 2.5 to 0.76 mm with an intermediate

Table 6.1.1. Composition, Ordered Structure, and Critical Ordering Temperature (T_c) of $(Fe,Ni,Co)_3V$ Ordered Alloys

Alloy	Composition (wt %)	Crystal Structure	T_c (°C)
Fe_3V	Fe—23 V	Disordered	
LRO–16	Fe—31 Ni—23 V	Ordered	670
LRO–17	Fe—30 Ni—8 Co—23 V	Ordered	700
LRO–20	Fe—40 Ni—23 V	Ordered	710
LRO–15	Fe—20 Ni—21 Co—23 V	Ordered	760

anneal at 1100°C. The as-rolled sheets were of good quality, with no indication of edge or end cracks. Chemical analysis of the final sheets shows about 200 to 400 ppm total of interstitial impurities, mainly O, C, and N.

6.1.4.3 Ordered Structure and Phase Relation

The phase relation and ordered structure in these alloys were determined by quenching and aging in the temperature range 300 to 1200°C. The disordered face-centered cubic (fcc) solid solution (alpha phase) existing in the alloys at high temperatures was retained at room temperature on quenching from above 1100°C. The alpha phase decomposes into $a + \sigma$ at temperatures below 1100°C. Analysis by x-ray diffraction indicates that the sigma phase has the tetragonal structure, with a lattice parameter close to the sigma phase in Fe–V, Co–V, and Ni–V alloy systems. At lower temperatures atomic ordering takes place in the alloys through the proeutectoid reaction $\sigma + a \rightarrow d$ The d can also be produced by aging the quenched a at temperatures below the ordering temperature. The cubic ordered phase a', which is the thermodynamically stable phase, is formed on the fcc lattice with ordered structure similar to $AuCu_3$ ($L1_2$ type). The superlattice lines of d are clearly visible in these alloys when examined with chromium $K\alpha$ radiation. Few inclusions are observed in the

alloys in both disordered and ordered states; those observed are probably interstitial compounds containing vanadium.

The ordering temperature was determined by aging-quenching treatment and measurement of thermal expansion. Thermal expansion shows a discontinuity with temperature near T_c. The T_c of the LRO alloys appears to increase with increasing nickel and cobalt concentration (Table 6.1.1). Alloy LRO-15, which contains a total of 41 wt % Co and Ni, has the highest T_c (760°C). So far ordering has not been detected at composition Fe_3V. This is probably because T_c is possibly below 400°C, and ordering is extremely sluggish.

In some heats of LRO-16 the disordered body-centered cubic (bcc) phase is detected by x-ray diffraction on quenching from above 1050°C. This may indicate that the composition of LRO-16 is close to an fcc/(fcc + bcc) phase boundary and that small variations in Fe, Ni, and V contents may affect the stability of the bcc phase.

6.1.4.4 Tensile Properties

Tensile tests were performed on an Instron testing machine at a crosshead speed of 2.5 mm/min. Effect of atomic ordering on the room temperature tensile properties is shown in Table 6.1.2. Atomic ordering has a small effect on the yield strength (a_Y) but significantly increases ultimate tensile strength (σ_t). This significant increase in σ_t (30 to 50%) is a result of a high work hardening rate in the ordered state. Formation of long-range order causes a moderate reduction in ductility; however, all the alloys remain ductile in the ordered state, as shown in Table 6.1.2. The alloys in the cubic ordered state had 30 to 50% elongation at room temperature.

The tensile properties of the ordered alloys at elevated temperatures are shown in Fig. 6.1.1. The striking result in Fig. 6.1.1(a) is that σ_Y of the ordered alloys increases with test temperature rather than decreasing like that of conventional alloys. The a_Y increases substantially with temperatures above 400°C and reaches a maximum around T_c. The strength

Table 6.1.2. Room Temperature Tensile Properties of Long-Range-Ordered Alloys in the Ordered and Disordered States

Alloy	State	Strength, MPa		Total Elongation (%)
		Yield	Tensile	
LRO-16	Disordered	393	820	38.6
LRO-16	Ordered	414	1071	30.3
LRO-17	Disordered	305	711	57.5
LRO-17	Ordered	287	1085	45.0
LRO-20	Disordered	289	703	58.5
LRO-20	Ordered	309	1055	43.8
LRO-15	Disordered	394	881	41.6
LRO-15	Ordered	354	1329	48.5

drops sharply above T_c as a result of disordering. The ordered alloys are much stronger than annealed type 316 stainless steel. The σ_y of the ordered alloys reached approximately 450 MPa, which is four times that of annealed type 316 stainless steel at 600°C.

In contrast to σ_y, σ_t decreases with test temperature, as shown in Fig. 6.1.1(b). The decrease apparently results from the recovery from strain hardening effects at elevated temperatures. However, the σ_t of the ordered alloys is two to three times that of solution-annealed type 316 stainless steel. The total elongation of the ordered alloys is not sensitive to test temperatures below 600°C. Above that temperature their ductility decreases with temperature and reaches a minimum of about 20% around T_c.

Scanning electron fractographs typical of the ordered alloys at room temperature and 650°C are shown in Fig. 6.1.2. The LRO-15 alloy showed ductile rupture characterized by dimples at these temperatures. The dimples are essentially asymmetric, indicating that the final rupture proceeded by shearing.

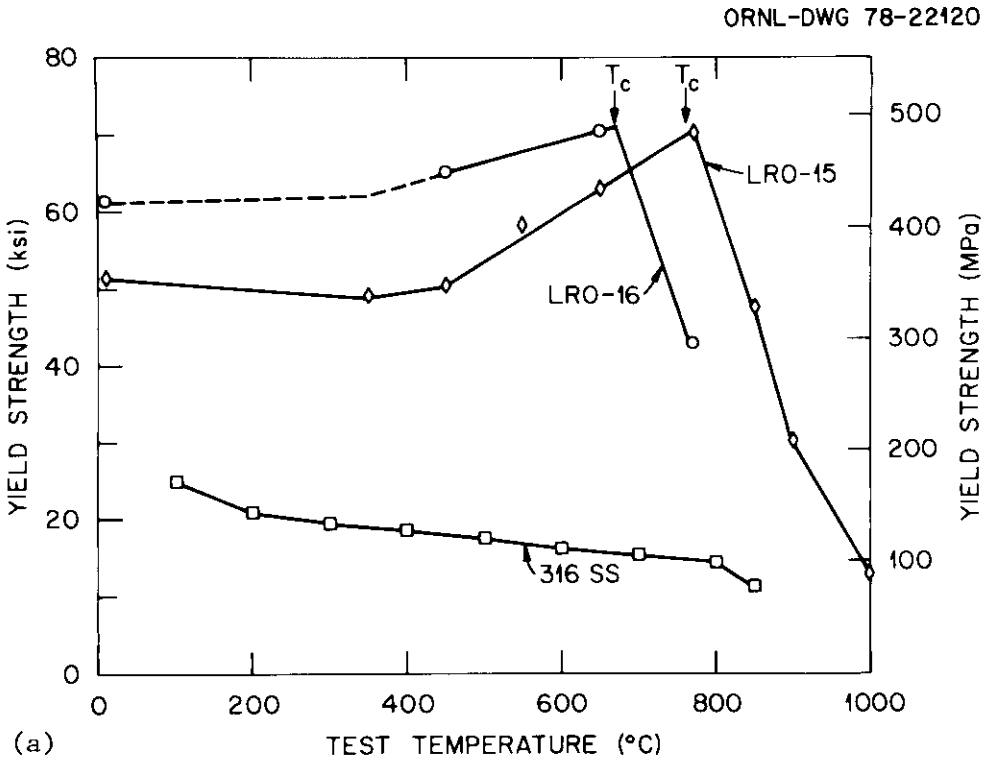

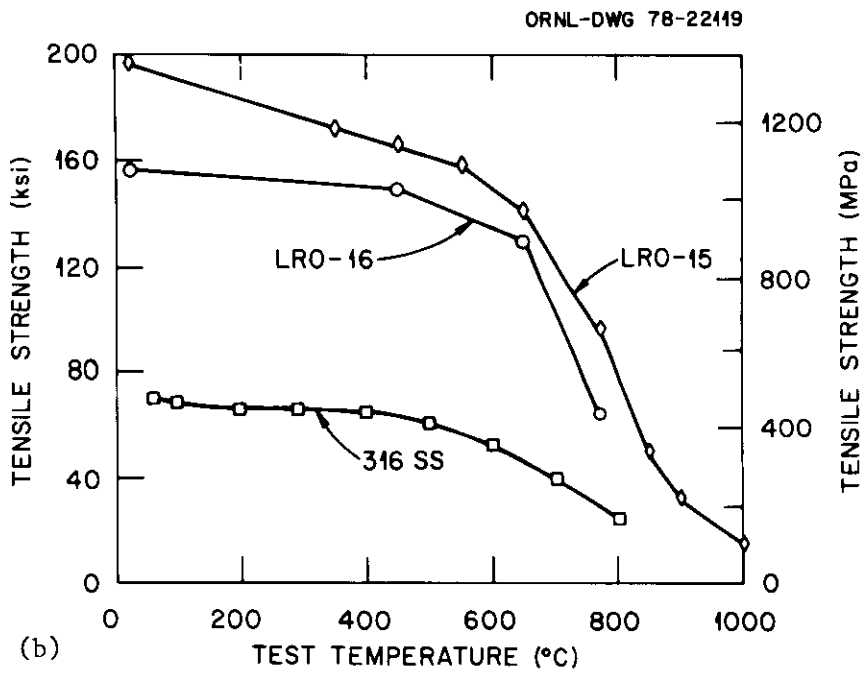

Fig. 6.1.1. Comparison of (a) Yield Strength, σ_y, and (b) Ultimate Tensile Strength, σ_t, of the Ordered Alloys LRO-15 and -16 with Type 316 Stainless Steel at Both Room and Elevated Temperatures.

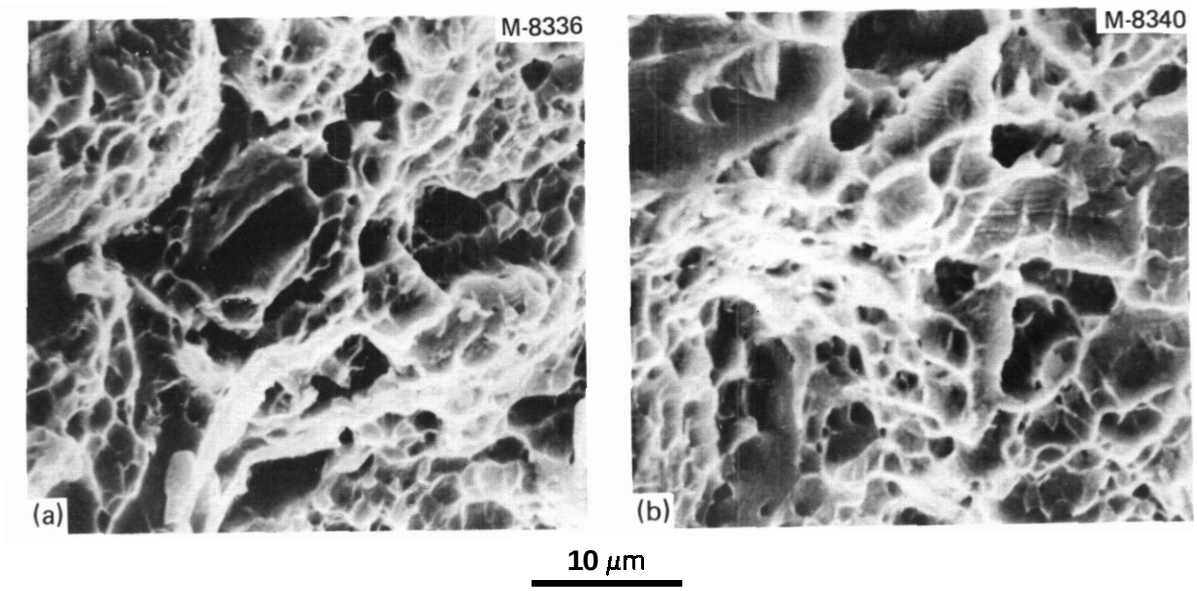

Fig. 6.1.2. Scanning Electron Fractograph of LRO-15 Specimens Fractured at (a) Room Temperature and (b) 650°C.

6.1.4.5 Creep Properties

The creep properties of the ordered alloys were determined at 650°C and 276 MPa. The results are compared in Table 6.1.3 with type 316 stainless steel. The creep rate increases with iron content, which lowers the T_c of the ordered alloys. The minimum creep rate of the ordered alloys is

Table 6.1.3. Comparison of Creep Behavior of Long-Range-Ordered Alloys with Type 316 Stainless Steel at 650°C and 276 MPa

Alloy	Condition	Minimum Creep Rate (1/h)	Rupture Life (h)
LRO-16	Ordered	9×10^{-6}	>1000[a]
LRO-17	Ordered	4×10^{-6}	>1000[a]
LRO-20	Ordered	3×10^{-6}	>1000[a]
LRO-15	Ordered	2×10^{-6}	>1000[a]
Type 316 Stainless steel	Annealed	1×10^{-2}	20

[a]Test was stopped after 1000 h.

lower than that that of type 316 stainless steel[6] by more than three orders of magnitude. In addition, type 316 stainless steel ruptured after a test of 20 h, while the ordered alloys did not fracture after 1000 h.

6.1.5 Conclusions and Future Work

Four iron-base ordered alloys with compositions listed in Table 6.1.1 are being developed for possible fusion energy applications. The alloys form a long-range-ordered crystal structure similar to $AuCu_3$ below their critical ordering temperature (670 to 760°C). The alloys in the ordered state are ductile, with total elongation in excess of 30% at room temperature. The study to date has demonstrated the very attractive mechanical properties of the iron-base LRO alloys. Their yield strength, instead of decreasing like that of conventional alloys, increases with test temperature and reaches a maximum around T_c. As a result the ordered alloys are much stronger than solution-annealed type 316 stainless steel, particularly at elevated temperatures. The ordered alloys are extremely resistant to creep deformation. Their creep rates are lower than that of type 316 stainless steel by at least three orders of magnitude.

Our program is continuing to develop and to characterize these iron-base ordered alloys for fusion energy applications.

6.1.6 References

1. J. L. Scott, "Materials for Fusion Reactors," *Met. Prog.* 114(2): 40–49 (1978).
2. N. S. Stoloff and R. G. David, "The Mechanical Properties of Ordered Alloys," *Prog. Mater. Sci.* 13(1): 1–84 (1966).
3. G.J.C. Carpenter and E. M. Schulson, "The Disordering of Zr_3Al by 1 MeV Electron Irradiation," *J. Nucl. Mater.* 23: 180–89 (1978).
4. E. M. Schulson, "Order Strengthening as a Method for Reducing Irradiation Creep: An Hypothesis," *J. Nucl. Mater.* 66: 322–24 (1977).
5. C. T. Liu and H. Inouye, "Control of Ordered Structure and Ductility of $(Fe,Co,Ni)_3V$ Alloys," *Metall. Trans.* A 10A(10): 1515–25 (1979).
6. V. K. Sikka, M. K. Booker, and C. R. Brinkman, *Use of Ultimate Tensile Strength to Correlate and Estimate Creep and Creep Rupture Behavior of Types 304 and 316 Stainless Steel,* ORNL-5285 (October 1977).

7. PATH E ALLOY DEVELOPMENT — FERRITIC STEELS

7.1 WELDING AND FABRICATION OF CANDIDATE FERRITIC STEEL

S. N. Rosenwasser, L. D. Thompson, R. D. Stevenson,
T. A. Lechtenherg, B. E. Thurgood and K. H. Holko
(General Atomic Company)

7.1.1 ADIP Task

ADIP tasks are not defined for ferritic stainless steel in the 1978 Program Plan.

7.1.2 Objective

The primary objective of this study is to establish the feasibility and develop the procedures for the welding and fabrication of 9-12 Cr steel in first wall and blanket structures. An additional objective is to develop the methodology for the management of fracture safe design in the use of ferritic steels in fusion, including the generation and analysis of pertinent unirradiated property data.

7.1.3 Summary

The logic and overall approach in the program was developed to meet the objectives of making firm recommendations regarding the ferritic steel fabrication/welding procedures and fracture management scheme for ETF components. Candidate sources were evaluated and a procurement plan for a 30,000 lb program heat of 12 Cr steel was developed. A chemical composition specification was formulated. A preliminary study to establish welding procedures for specimens to be exposed in the near term EBR II and HFIR irradiation was initiated and test panel welding was completed. The microstructural features of conventional gas-tungsten arc (GTA) and advanced laser weldments of HT9 were evaluated and compared. Preliminary evidence indicates that laser welding may be a promising method for producing 12 Cr weldments.

7.1.4 Progress and Status

During this reporting period the overall program logic which will result in firm recommendations concerning ferritic fabrication/welding procedures and a fracture management scheme for ETF components was completed. The logic diagram is shown in Figure 7.1.1. An assessment of potential melters/fabricators of a 30,000 lb 12 Cr DINX20CrMoWV121 (HT9) heat for use in the material program was completed and the alloy chemistry specifications were established. The microstructural features associated with initial gas-tungsten arc and laser welds are compared. A preliminary welding program directed at determining a suitable welding procedure for preparing specimens for EBR-II and HFIR irradiations was initiated and test weld panels were produced.

7.1.4.1 12 Cr Heat Procurement

A detailed review of potential melters and fabricators of a large 12 Cr-1 Mo-0.3V heat for use in the remainder of the national fusion ferritic program was completed, and a procurement plan consistent with available funding was recommended. A summary of the plan is shown in Table 7.1.1. Both of the recommended producers, Carpenter Steel Division, Reading, Pa. and Electralloy Corporation, Oil City, Pa. were judged the most qualified of the available vendors to melt the required 30,000 lb Argon-Oxygen Decarburized (AOD) heat and could meet the required schedule. Carpenter is a commercial supplier of 12 Cr steels (i.e., Type 422) and have produced both the U.S. FBR cladding and duct program HT9 heat and the ORNL developmental 9 Cr-1 Mo alloy large heat. Electralloy are respected specialty alloy melters in the steel industry and are experienced at producing 12 Cr steels. The final selection of a producer will he made after formal quotations are received.

The plan is to produce only AOD stock this year, including electrodes which can be Electro-Slag Remelted (ESR) if desired and fabricated in FY81 with additional funds. It is not clear at this time that the more expensive AOD/ESR process is superior to the AOD process for large heats. Commercial practice on 12 Cr steels is air melting or AOD. The relative

GA FERRITICS FOR FUSION PROGRAM LOGIC

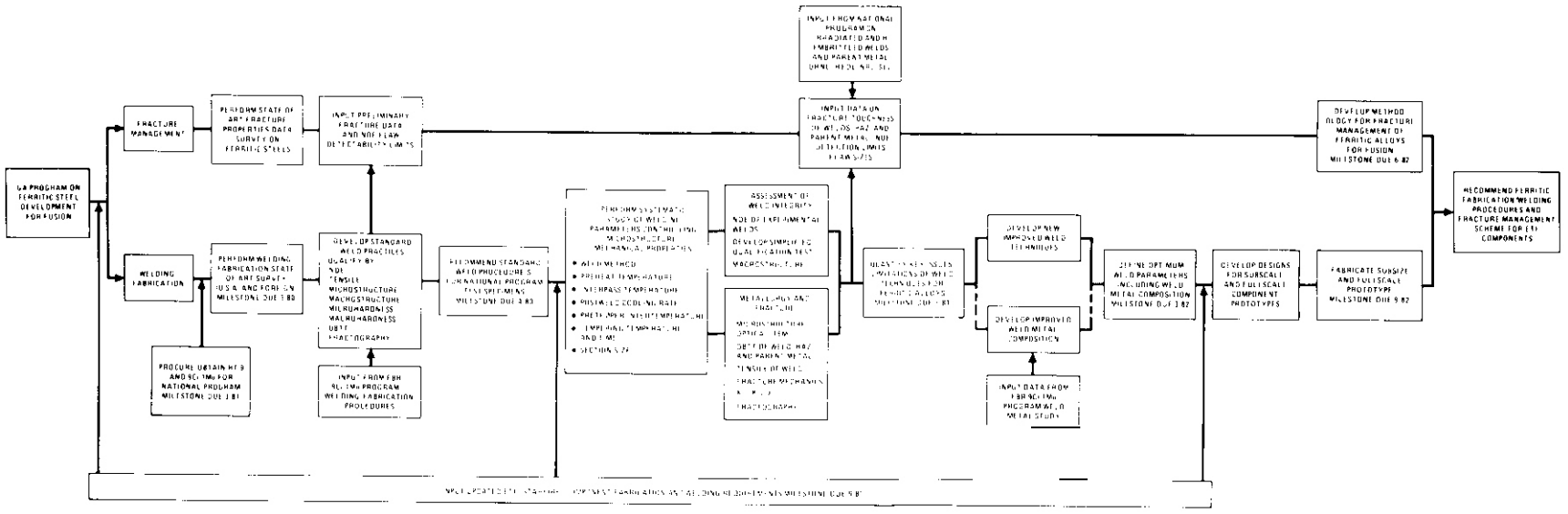

Fig. 7.1.1. Logic Diagram for GA Program Addressing Welding Fabrication and Fracture Management Issues

Table 7.1.1. Recommended Procurement Plan for Fusion Program
12 Cr Ferritic Steel Procurement

FY	Order (Date)	Vendor	Delivery Date
80	AOD melt and pour ~30,000 lb heat (2/30/80) including: 2 slabs or 3 ingots (14,000-16,500 lbs) 2 ESR electrodes (16,000 lbs)	Electralloy or Carpenter	4/30/80
	Fabricate 9-10,000 lb plate stock (3/30/80) store ESR electrodes	Jessop	6/30/80
81	ESR up to 16,000 lb (10/30/80)	Carpenter or Guterl	1/30/80
	Fabricate up to 16,000 lb (1/30/80) tube and/or flat stock	Carpenter Jessop	4/30/81

merits of AOD vs. AOD/ESR are being evaluated in the ORNL 9 Cr program and that information will be available to the fusion program to factor into the decision. By retaining about 1/2 of the total material in ingot form, it will be possible to fabricate forms (tubes, pipes, etc.) consistent with ETF design requirements during FY81. Jessop Steel will fabricate sheet and plate this fiscal year. The proposed alloy chemistry specification, shown in Table 7.1.2, (consistent with German material specification DINX20CrMoWV121 Material 1.4935) is based upon discussions with vendors, HEDL, and V. Sikka, principal investigator of the ORNL 9 Cr program.

7.1.4.2 Development of Welding Procedures for Near Term Irradiation Experiments

A limited investigation to determine suitable procedures for producing weldments to be exposed in EBR II and HFIR irradiation experiments during FY80 was initiated. Variables in gas-tungsten arc (GTA) and shielded metal arc (SMA) processes were evaluated as shown in Table 7.1.3.

Procedures within the range of GTA welding parameters recommended by European fabricators were evaluated by varying preheat and interpass temperatures. A single SMA weld was included for comparative purposes. For each weld parameter combination, two plates, 30 cm x 10 cm x 0.56 cm, were welded lengthwise in the fully restrained condition with HT9 wire. The plates were fabricated at GA from Sandvik (Sweden) HT9 pipe, with the following chemistry (vendor values): 11.3 Cr, 0.85 Mo, 0.50 W, 0.27 V, 0.22 C, 0.5 Ni, 0.52 Mn, 0.38 Si, 0.019 P, and 0.006 S percent by weight. Plate thickness was 0.56 cm.

Several techniques were employed to qualify the welds. Standard ASME Sections III and IV, Nuclear Boiler Code acceptance tests served as a basis for comparison. These tests included NDE, tensile, root bends, and face bends, as well as macro- and micro-hardness tests and optical metallography. In addition, Charpy V-notch impact testing was performed to study the fracture behavior of the weldments (V-notch centered in the weld metal) and to determine the ductile-to-brittle transition temperatures.

Table 7.1.2. Chemical Composition Specification for Fusion 12 Cr **Steel** Procurement

	Range	Target
C	0.20/0.23	0.22
Si	0.10/0.50	0.25
Mn	0.30/0.EO	0.55
P	0.02 (max)	0.01
S	0.01 (max)	0.006
Cr	11.0/12.5	11.5
Mo	0.80/1.20	1.0
Ni	0.40/0.60	0.50
V	0.25/0.35	0.30
W	0.40/0.60	0.50
N	0.02/0.06	0.04
Al		0.04 (max)
Ti		0.01 (max)
cu		0.10 (max)
O_2		0.02 (max)
co		0.05 (max)
AS		0.01 (max)
B		0.001 (max)
Bi		0.001 (max)
Pb		0.001 (max)
Sb		0.001 (max)
Sn		0.001 (max)
Cb		0.001 (max)

All welds have been prepared and have passed the dye penetrant and magnetic particle non-destructive evaluations. All GTA welds passed the X-ray examinations while small areas of incomplete penetration were detected in the SMA welds. These areas were removed from the SMA weldments. The remaining mechanical test/metallography specimens have been prepared and are either being tested or the data is being reduced and analyzed.

7.1.4.3 Comparison of GTA and Laser HT9 Weldments

At the inception of the FY80 program, preliminary weldments were prepared to become familiar with the microstructural features produced by the conventional GTA and the advanced laser welding procedures. As discussed earlier, the GTA method will be used for the near term irradiation experiments and subsequently will be the basic process for the weld parameter sensitivity study. The laser method will be more fully evaluated later in the program in the improved weld method development study.

The base material was the flattened HT9 pipe described in Section 7.1.4.2. For the gas-tungsten arc weld, a typical European industrial procedure involving a preheat and a post-weld heat treatment was used. The laser weld was made in a single pass with a square butt joint preparation using no preheat or postheat. The welding parameters used in the two welds are summarized in Table 7.1.4. The difference in welding speeds produced marked differences in heat input for the two processes. For the GTA weld, heat inputs from 8,000 to 9,000 joules per centimeter were calculated as compared to 2,400 joules per centimeter for the laser weld. The material was welded in the solution-annealed and tempered condition.

Figure 7.1.2 shows macrosections of the as-welded plates. Table 7.1.5 lists the hardness measured for the weld metal, heat-affected zone, and parent metal. In the case of laser welding, as-welded values, in addition to measurements made following a temper or a solution-anneal and temper heat treatment are listed. Since the GTA weld specimen was never cooled to room temperature, only hardness measurements following the tempering treatment were made.

Table 7.1.3. Test Matrix for the Investigation of HT9 Weld Procedures for Near Term Irradiation Experiments

Process[a]	Number of Weldments	Preheat	Interpass Range	Temperature Before PWHT[b]	PWHT[c]
GTAW	2	343°C	288-343°C	93°C ± 14°C	730°C ± 14°C/1 h
GTAW	2	205°C	149-205°C	93°C ± 14°C	780°C ± 14°C/1 h
GTAW	2	93°C	93-149°C	93°C ± 14°C	780°C ± 14°C/1 h
GTAW	2	R.T.	R.T.-52°C	R.T.	780°C ± 14°C/1 h
GTAW	2	R.T.	R.T.-52°C	R.T.	780°C ± 14°C/1 h

(a) GTAW - Gas-Tungsten Arc Welding
SMAW - Shield Metal Arc Welding

(b) Cool in still air

(c) Heating and cooling rates: 93°C to 593°C at ≈ 222°C/h
593°C to 760°C at ≤ 167°C/h

Tempering after welding was effective in reducing the high as-welded hardness for the weld metal and heat-affected-zones to values more representative of the parent metal for both laser and CTA welds. As-welded weld-metal hardnesses were fairly high (R_c 45-50) for the laser welds. From Fig. 7.1.2, heat-affected-zone (HAZ) widths were significantly different for weldments made by the two processes. Both metallographic observations and microhardness traverses showed that the HAZ was approximately 0.05 cm wide for the laser welds and approximately 0.35 cm wide for the GTA welds. The significance of this observation is that welding processes such as laser welding and electron beam welding, that produce welds in hardenable materials with narrow heat-affected-zones, usually have a lower preheat temperature requirement as compared to other welding processes. The weldments were found to be free of any significant cracks by standard NDE weldment inspection techniques. An important variable between the two processes was the type of restraint. For the GTA weld, the base metal plates were fillet welded to a thick steel plate prior to welding while the laser weld plates were only restrained by clamping. To make a complete comparison, the laser weld plates would have to be fully restrained. The inherent differences in weldment characteristics for the two processes are still considered valid despite the discrepancy.

Figure 7.1.3 shows the pertinent microstructural features of the tempered GTA weld. The whitish phase present in patches is believed to he delta ferrite and was found to he significantly softer than the adjacent tempered martensitic matrix by microhardness testing. Large proportions of delta ferrite were present in both the weld metal and heat-affected zone microstructures and probably results from the high heat input levels associated with the GTA welding process. Table 7.1.4 indicates that the hardness levels across the weld were fairly uniform and the slightly higher hardness of the parent metal was associated with the smaller proportion of delta ferrite present in the microstructure.

Figure 7.1.4 shows the as-welded microstructure of the laser weldment. The weld metal consisted of a dendritic substructure and

Table 7.1.4. Welding Parameters Used in Preliminary Gas-Tungsten Arc and Laser Welds in HT9 Plate

GAS TUNGSTEN ARC WELD	LASER WELD
V-Groove Joint Preparation	Square Butt Joint Preparation
Four Passes	Single Pass
13 cm/min	127 cm/min
HT9 Filler Added	No Filler Added
Preheated at 343°C	No Preheat
Postheated at 760°C/1 Hr.	No Postheat

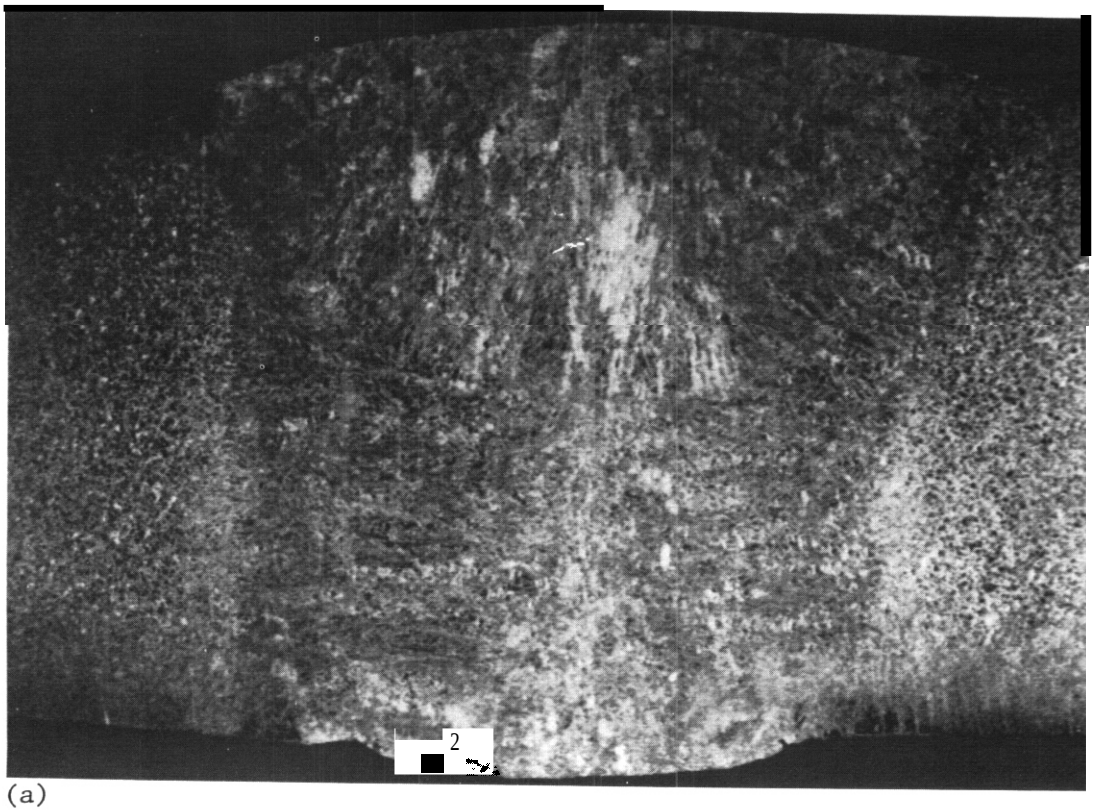

(a)

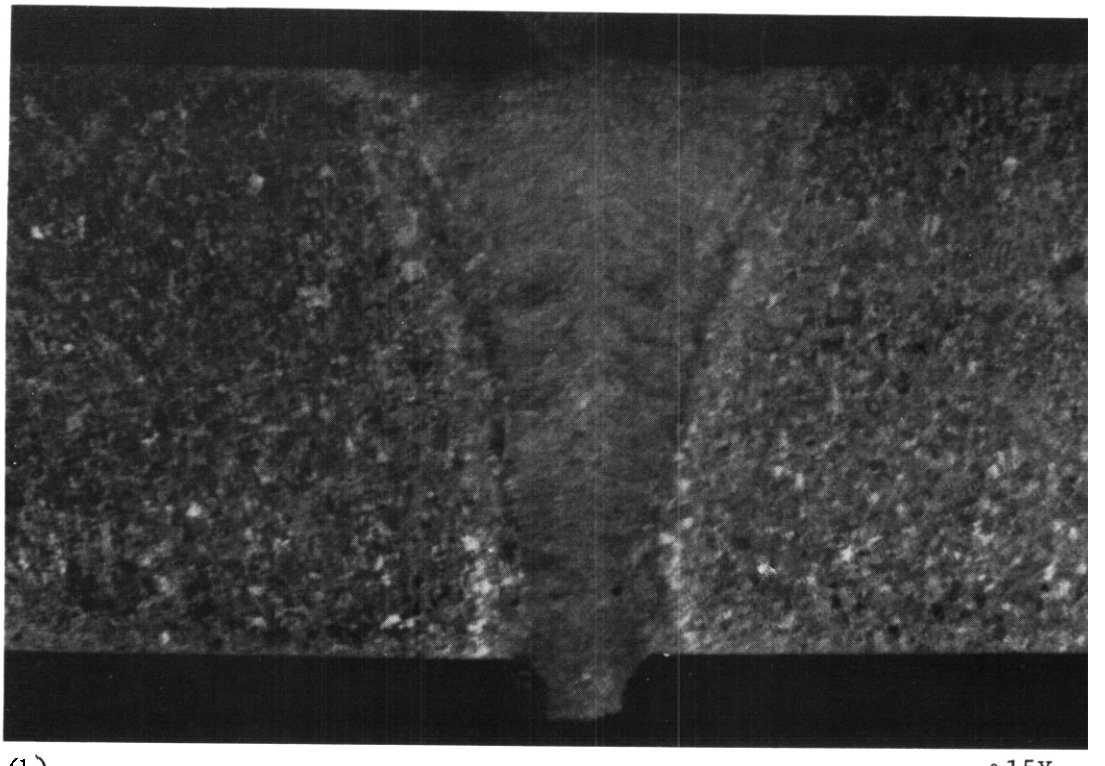

(b) ∿15X

Fig. 7.1.2. Optical Micrographs Comparing the As-Welded Conditions for HT9 Weldments Prepared by (a) Gas-Tungsten Arc Welding, and (b) Laser Welding.

Table 7 1.4. Hardness Data from HT9 GTA and Laser Weldments

Sample No.	Welding Process	Preheat	Postheat	Rockwell Hardness[a]		
				Parent Metal	HAZ	Weld Metal
5A	Laser	None	None	Rb 94.7	Rb 100	Rc 45
5B	Laser	None	None	Rb 96.2	Rb 99	Rc 44.3
5B	Laser	None	T[b]	Rb 99	Rb 98	Rb 98
5C	Laser	None	None	Rb 99.2	Rc 25	Rc 47
5C	Laser	None	SAT[c]	Rb 98.2	Rb 98	Rb 95
M2	Gas-Tungsten Arc	650°F	T	Rb 98.2	Rb 94.7	Rb 96.2

(a) Average of at least three readings

(b) T - Temper--760°C/1 hour

(c) SAT - Solution Anneal + Temper - 1050°C/0.5 hours + 780°C/2.5 hours

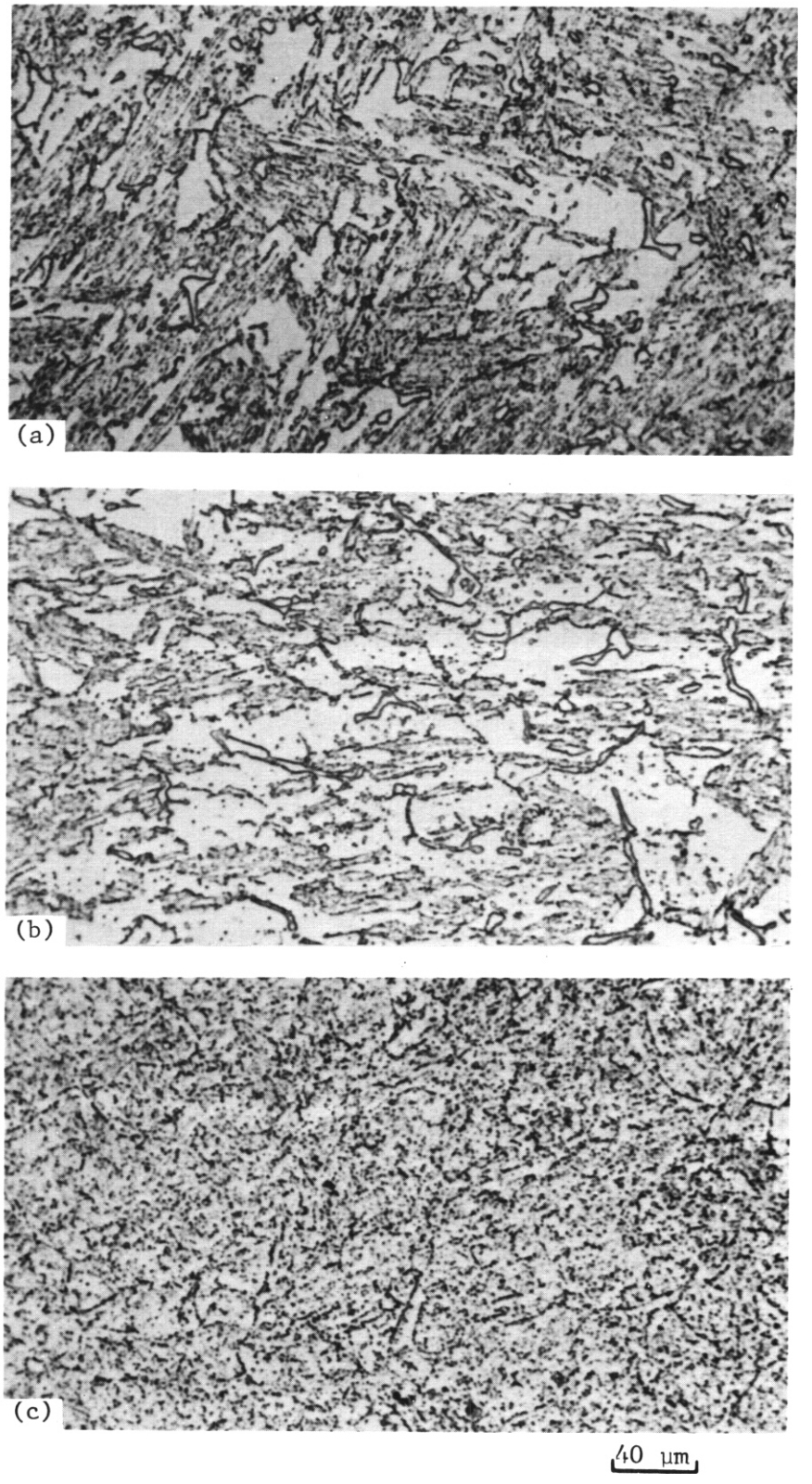

Fig. 7.1.3. Optical Micrographs Showing Characteristic Microstructures Observed Following Gas Tungsten Arc Welding and Tempering; (a) Weld Metal, (b) Heat-Affected-Zone, and (c) Parent Metal

from microhardness measurements was probably untempered martensite. Good fusion was observed across the weld with the heat-affected-zone being quite thin. The laser weld was given either a tempering treatment or a full solution-anneal and tempering treatment. Figure 7.1.5 shows macrosections of the laser weldments following these two heat treatments. In both cases the weldment appeared sound and free of defects. Figures 7.1.6 and 7.1.7 show the microstructures observed for both cases. The tempering treatment was very effective in producing a uniform microstructure relatively free of delta ferrite. As shown in Fig. 7.1.6(b), a smooth microstructural transition was observed between the weld metal and the heat-affected-zone for the tempered laser weld. For the weldment given the solution-anneal and temper, the heat-affected-zone appeared to contain substantially higher levels of ferrite, although hardness levels were similar across the weldment. The solution-anneal and temper restored the weld metal and heat-affected-zone to microstructures similar to that of the parent metal, as would be expected. This latter heat treatment would present problems in the fabrication of engineering structures and justification for its use could only be made if the mechanical properties of more conventional welds were unacceptable.

Laser welding appeared to offer significant advantages over gas-tungsten arc welding of HT9, at least in the low restraint condition studied. The heat input, volume of material melted, and heat-affected-zone size were smaller than those of the GTA weld. In addition, no preheat was employed for the laser welding which alone is a very significant feature. Because of these potential benefits it is evident that laser welding should be further evaluated later in the program. However, more conventional processes, such as the GTA method, should be emphasized simply because fabrication of ETF components and other fusion structures will necessitate the use of well established techniques for a variety of difficult joint configurations, and low-accessibility situations.

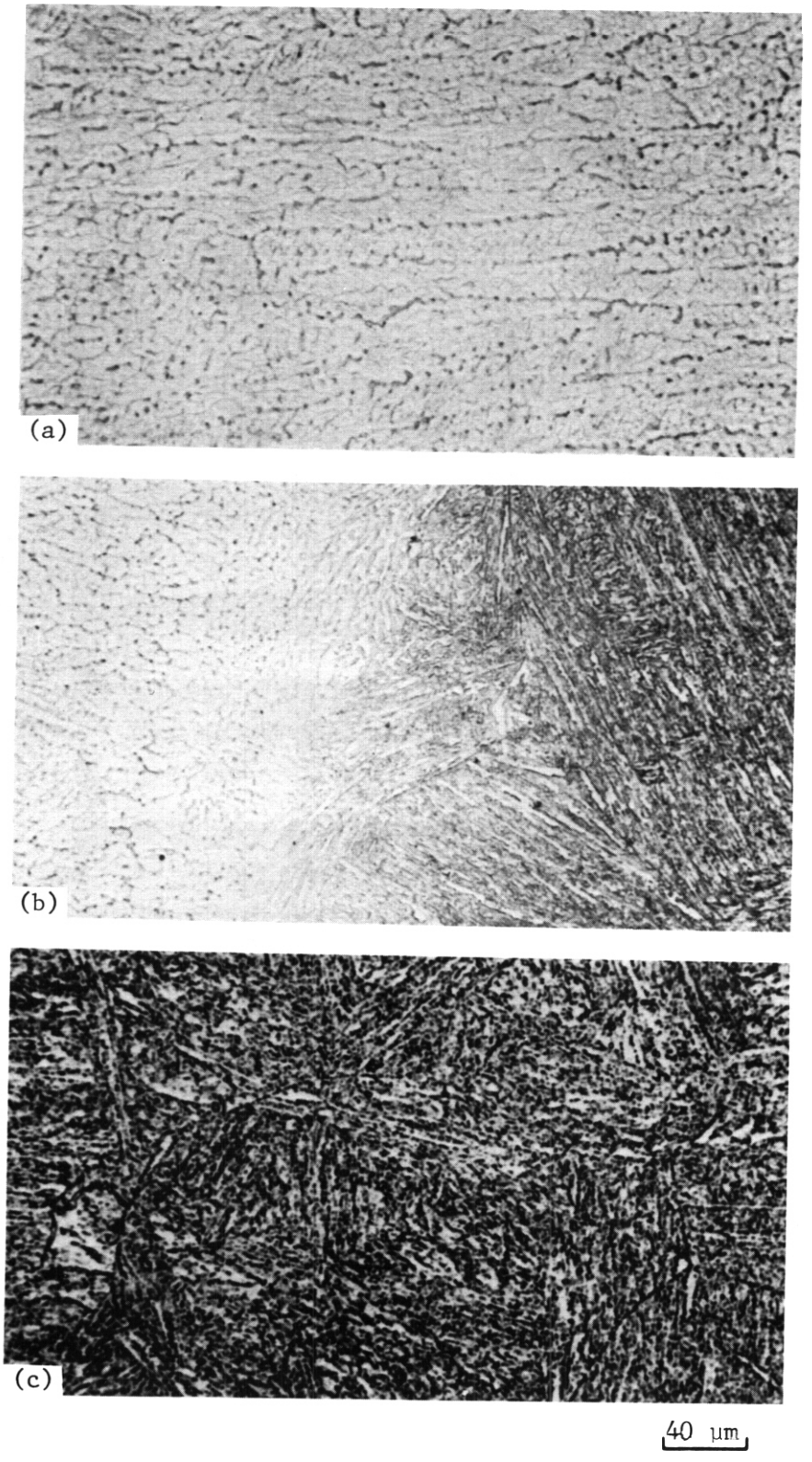

Fig. *7.1.4.* Optical Micrographs Showing Characteristic Microstructures Observed for the As-Laser-Welded Plate Weldment; (a) Weld Metal, (b) Weld Metal/Heat-Affected Zone, and (c) Parent Metal

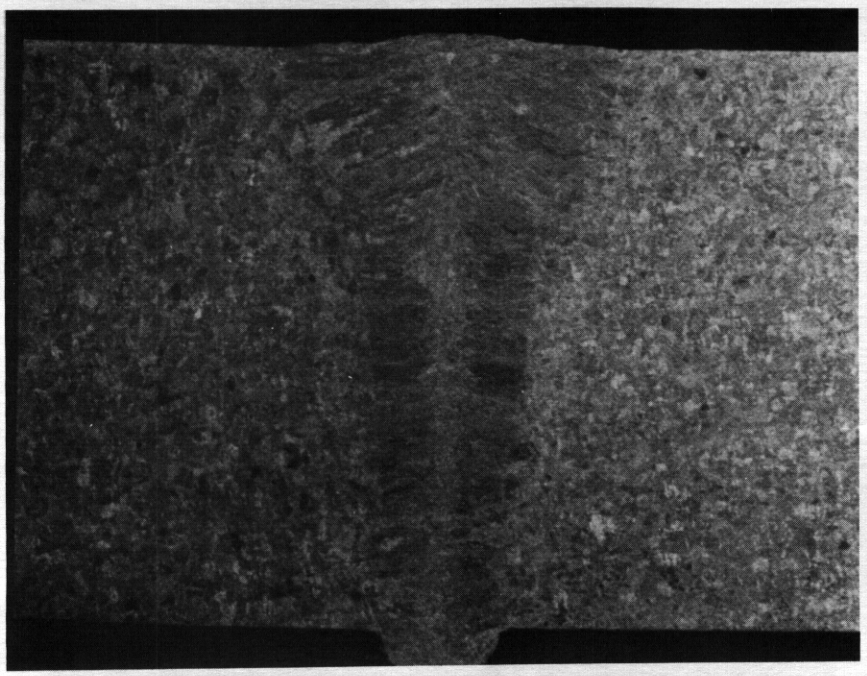

(a)

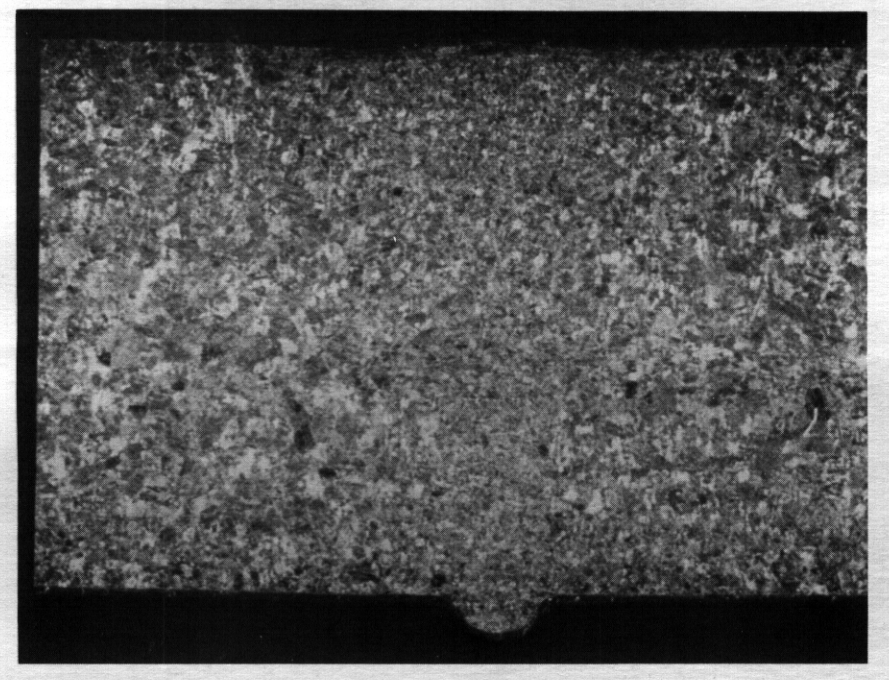

(b) 12X

Fig. 7.1.5. Optical Micrographs Comparing Laser Weldments Following (a) a Post-Weld Tempering Treatment and (b) a Post-Weld Solution-Anneal and Tempering Treatment

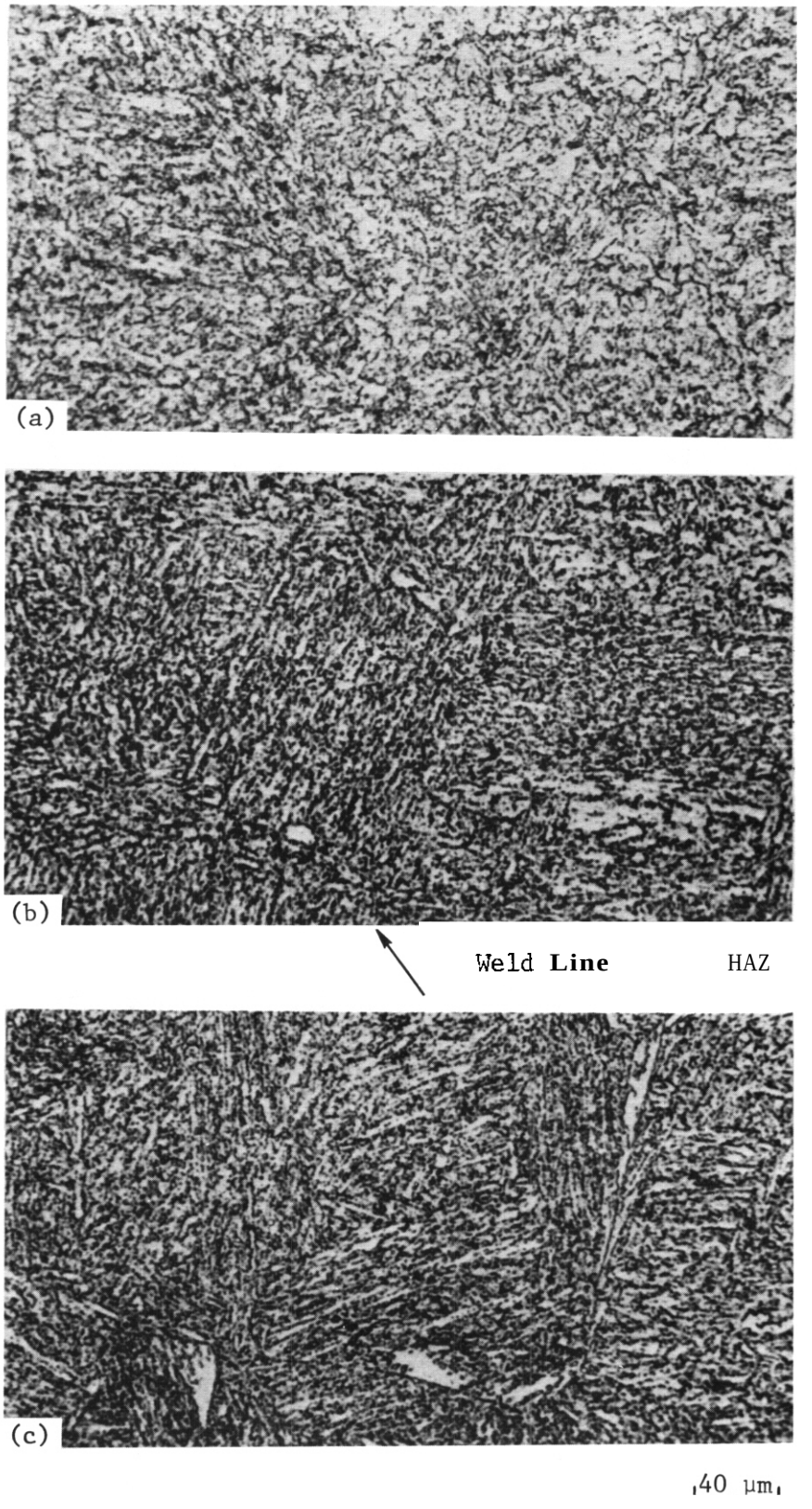

Fig. 7.1.6. Optical Micrographs Showing Characteristic Microstructures Observed Following Laser Welding and Tempering; (a) Weld Metal, (b) Weld Metalheat-Affected Zone, and (c) Parent Metal

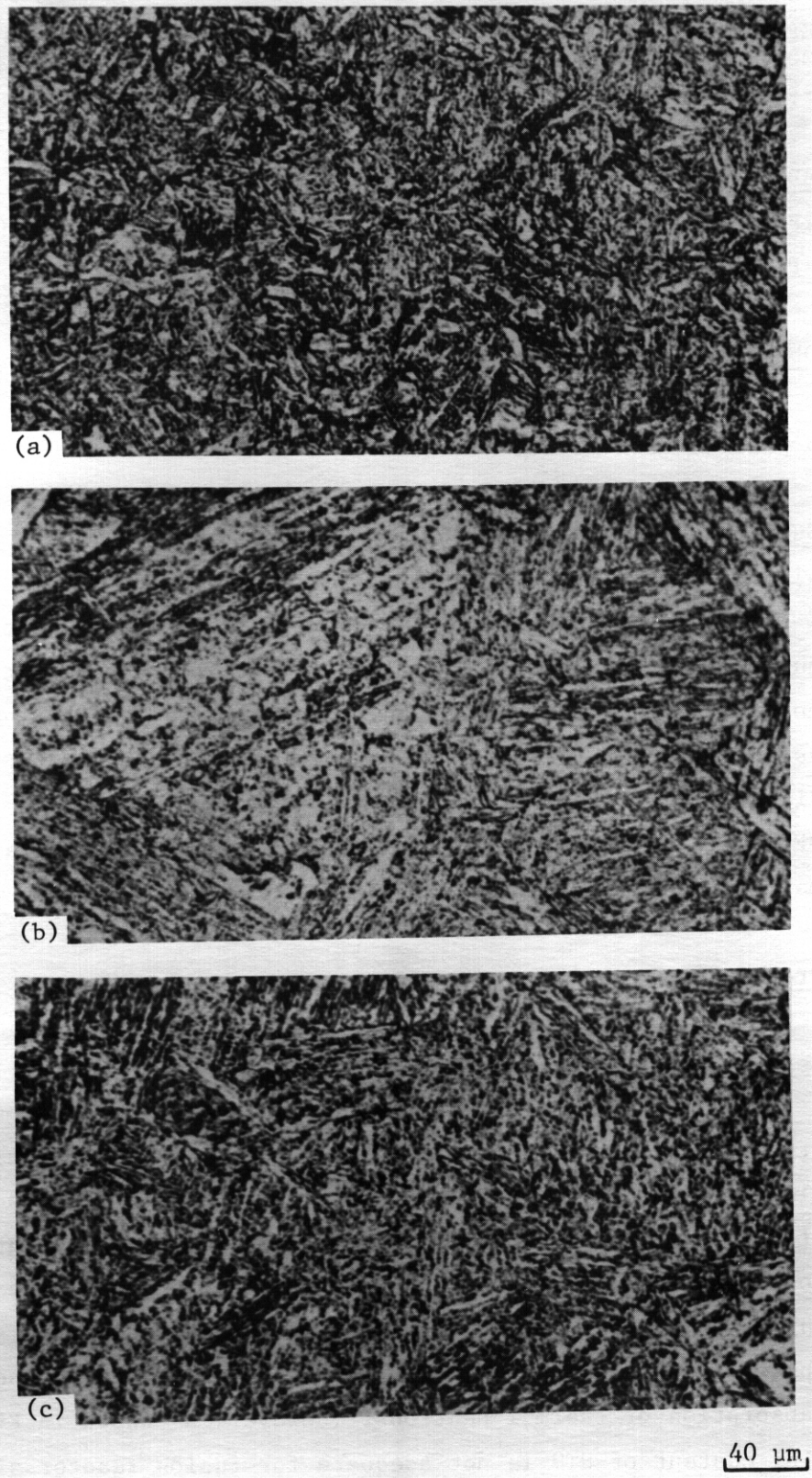

Fig. 7.1.7. Optical Micrographs Showing Characteristic Microstructures Observed Following Laser Welding, Solution-Annealing and Tempering; (a) Weld Metal, (b) Heat-Affected Zone, and (c) Parent Metal

7.2 PREPARATION OF NICKEL-DOPED FERRITIC ALLOYS FOR HFIR IRRADIATION TO PRODUCE HELIUM – M. L. Grossbeck, V. K. Sikka, T. K. Roche, and R. L. Klueh (ORNL)

7.2.1 ADIP Task

ADIP Tasks are not defined for Ferritic Stainless Steels in the 1978 Program Plan.

7.2.2 Objective

The goal of this project is to prepare ferritic steels for irradiations to produce transmutation helium.

7.2.3 Summary

Small heats of HT9 and 9 Cr-1 Mo steels have been prepared containing 1 and 2% Ni. An additional heat of each alloy was prepared with 2% Ni but with adjustments in the carbide-forming elements to restore the chromium equivalent to a value near that of the original alloy. Tensile and transmission electron microscope (TEM) specimens of these materials will be irradiated in the High Flux Isotope Reactor (HFIR). The thermal flux in the HFIR will result in the formation of helium in concentrations approximating those produced in fusion reactor service.

7.2.4 Progress and Status

7.2.4.1 Introduction

The inherent physical properties and irradiation damage resistance of ferritic steels, such as Sandvik HT9, have led to consideration of these alloys for use as fusion reactor first walls. Since an adequate source of 14-MeV (2.2-pJ) neut'rons is not available, an alternative method for simulating 14-MeV neutron irradiation, including the transmutation helium production, must be used. For austenitic stainless steels there is sufficient nickel to produce more than enough helium through absorption of thermal neutrons. However, as shown in Fig. 7.2.1, the 0.5% Ni content of HT9 is not adequate for fusion reactor simulation, and 9 Cr-1 Mo steel contains even less nickel. However, alloys containing

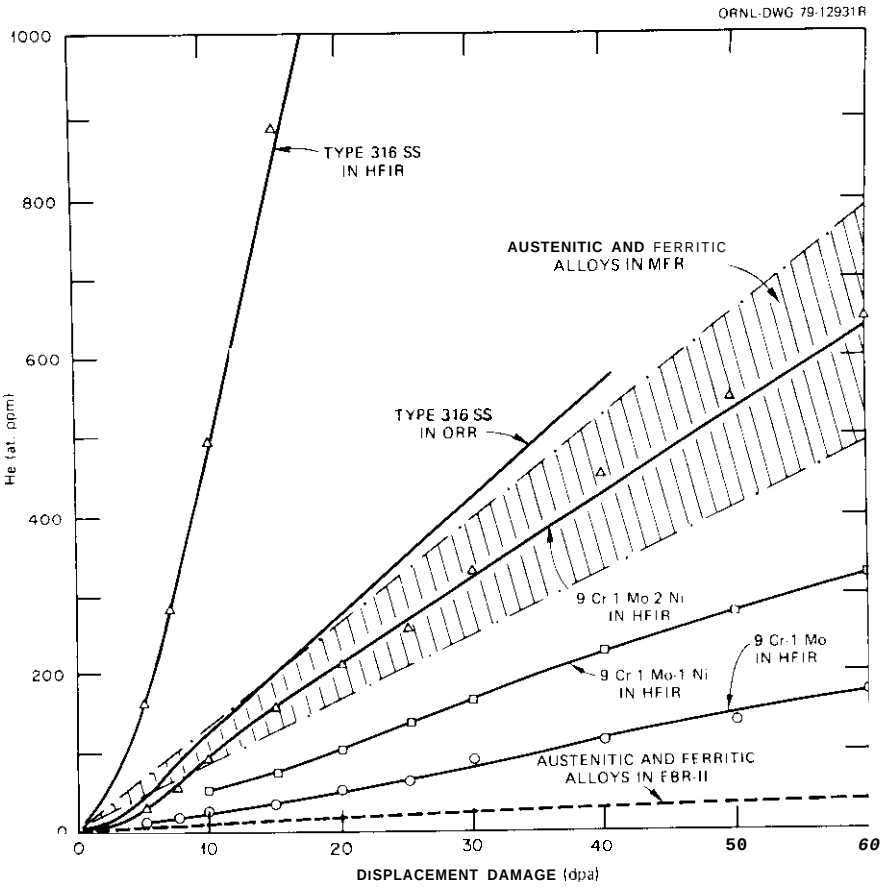

Fig. 7.2.1. Relationship Between Helium Production and Displacement Damage €or Different Alloys and Test Environments.

2%Ni irradiated in the HFIK would achieve approximately the same helium production rate as the original alloys in fusion reactor service for a neutronic wall loading near 3 MW/m^2. The rate of displacement damage production is also appropriate €or this wall loading.

7.2.4.2 Experimental Procedure

Four heats of HT9 and three of 9 Cr-1 Mo steel were prepared by Combustion Engineering by electroslag remelting. First, four heats of HT9, which were composed similarly to heat 91354 from the breeder reactor stockpile, were prepared. One heat was left unchanged, another was doped with 1%Ni, and two were doped with 2% Ni. Chromium, molybdenum, and tungsten were added to one 2%Ni heat to increase the chromium equivalent (Table 7.2.1), as calculated by the following equation:'

Table 7.2.1. Chromium Equivalent of Experimental Heats of Ferritic Alloys

Alloy	Heat	Chromiun Equivalent
HT-9 breeder	91354	11.3
HT-9	MA-3587	8.9
HT-9 + 1%Ni	XAA-3588	7.2
HT-9 + 2% Ni	XAA-3589	2.3
HT-9 + 2% Ni adjusted	MA-3592	8.4
9 Cr-1 Mo breeder	30182	10.9
9 Cr-1 Mo	XA-3590	9.4
9 Cr-1 Mo + 2% Ni	XA-3591	2.2
9 Cr-1 Mo + 2% Ni adjusted	XA-3593	9.1

$$\text{Chromium Equivalent} = \%\,Cr + b(\%\,Si) + 4(\%\,Mo) + 1.5(\%\,W) + 11(\%\,V) + 5(\%\,Nb) - 40(\%\,C) - 2(\%\,Mn) - 4(\%\,Ni) - 2(\%\,Co) - 30(\%\,N)\ .^{*}$$

However, each of these elements was increased only a small amount to remain within the composition range of HT9. Therefore, except for nickel, all four heats may he considered HT9. The compositions are shown in Table 7.2.2.

Similarly, three heats of 9 Cr-1 Mo comparable to those prepared for the Advanced Alloy Technology Project for the Breeder Reactor Program were prepared. Two of the heats were doped with 2% Ni. The third heat had 2% Ni plus additional chromium and molybdenum. The molybdenum remains close to the specification for 9 Cr-1 Mo steel, but the chromium is higher.

All seven alloys were prepared in 25-kg heats, and a sample of each was rolled into 3.2-mm plate. This plate was further rolled into 0.254 and 0.762-mm sheet for specimen fabrication.

---

* Compositions used in this equation are in weight percent.

Table 7.2.2. Composition of Heats of Doped Ferritic Steels

Element	Alloy Content,[a] wt %								
	HT-9 Breeder (91354)	HT-9 (XAA-3587)	HT-9 + 1% Ni (XAA-3588)	HT-9 + 2% Ni (XAA-3589)	HT-9 + 2% Ni Adjusted (XAA-3592)	9 Cr-1 Mo Breeder (30182)	9 Cr-1 Mo (XA-3590)	9 Cr-1 Mo + 2% Ni (XA-3591)	9 Cr-1 Mo + 2% Ni Adjusted (XA-3593)
C	0.20	0.21	0.20	0.20	0.15	0.088	0.09	0.064	0.067
Mn	0.47	0.50	0.47	0.49	0.32	0.37	0.36	0.36	0.36
P	0.004	0.011	0.010	0.011	0.008	0.011	0.008	0.008	0.008
S		0.004	0.004	0.004	0.004	0.004	0.004	0.004	0.004
Si	0.31	0.18	0.13	0.14	0.07	0.19	0.08	0.08	0.10
Ni	0.54	0.43	1.14	2.27	2.30	0.09	0.11	2.17	2.24
Cr	11.2	11.99	11.97	11.71	13.60	8.47	8.62	8.57	12.30
Mo	0.96	0.93	1.04	1.02	1.59	0.88	0.98	0.98	1.70
V	0.31	0.27	0.31	0.31	0.30	0.21	0.209	0.222	0.29
Nb		0.018	0.015	0.015	0.016	0.07	0.063	0.066	0.074
Ti		0.003	0.003	0.003	0.002	0.001	0.002	0.002	0.002
Co	0.02	0.017	0.015	0.021	0.018	0.017	0.013	0.015	0.017
Cu	0.04	0.05	0.05	0.05	0.05	0.03	0.03	0.04	0.03
Al	0.03	0.030	0.017	0.028	0.018	0.009	0.013	0.015	0.016
B	0.0007	<0.001	<0.001	<0.001	<0.001	0.0006	<0.001	<0.001	<0.001
W	0.5	0.54	0.53	0.54	0.64	<0.01	0.01	0.01	0.01
As	0.01	<0.001	0.002	<0.002	<0.002	<0.001	<0.001	<0.001	<0.001
Sn	0.01	0.002	0.001	0.002	0.002	0.002	0.003	0.003	0.003
Zr		<0.001	<0.001	<0.001	<0.001	<0.001	<0.001	<0.001	<0.001
N		0.020	0.016	0.017	0.014	0.054	0.050	0.053	0.059
O		0.005	0.007	0.007	0.007	0.008	0.007	0.006	0.007

[a]Balance Fe.

7.2.4.3 Discussion and Future Experiments

Tensile specimens and TEM discs are being prepared for insertion into reactor irradiation experiments HFIR-CTR-30, -31, -32, and -33. Work is progressing normally with the exception that the HT9 with 2% Ni (unadjusted) was rather brittle. This brittleness is now being investigated.

7.2.5 Reference

1. D. L. Newhouse, C. J. Boyle, and R. M. Curran, "A Modified 12-Percent Chromium Steel for Large High-Temperature Steam Turbine Rotors," paper presented at ASTM 68th Annual Meeting, Lafayette, Indiana, June 13-18, 1965.

7.3 TEST PLAN FOR THE INVESTIGATION OF IRRADIATION EFFECTS UPON EECHANICAL PROPERTIES OF FERRITIC ALLOYS - R. J. Puigh and B. A. Chin (Hanford Engineering Development Laboratory)

7.3.1 ADIP Task

The Department of Energy (DOE)/Office of Fusion Energy (OFE) has cited the need for these data under the ADIP Program task, Ferritic Material Development (Path E).

7.3.2 Objective

The objective of the fusion AD-2 experiment is to provide baseline, high fluence data at several temperatures for ferritic alloys HT-9 and 9Cr-1Mo. Developmental 2¼Cr-1Mo will also be scoped in this experiment. Specifically, the *AD-2* experiment is designed to yield data concerning the radiation effects upon the mechanical properties such as fatigue, fracture toughness, tensile strength and weld properties for these alloys. Characterization of the radiation effects upon their microstructure will also be performed.

7.3.3 Summary

The AD-2 experiment **will** consist of six, uninstrumented B-7c pins containing microstructure and mechanical property specimens made from ferritic alloys. Alloy selection, irradiation temperatures and the test matrix **have** been specified and approved by the Alloy Development for Near Term Applications Working Group. Approval in principle has been granted by DOE for the AD-2 experiment' and irradiation will begin at EBR-II in June, 1980.

7.3.4 Progress and Status

7.3.4.1 Introduction

A data base assessment of HT-9 and developmental 9Cr-1Mo martensitic stainless steels has indicated that these ferritic alloys exhibit desirable mechanical properties when considered for application as materials for the first wall/blanket of a fusion power reactor.[2] On the basis of irradiation test results from the National Clad/Duct Materials Development

Program, HT-9 has been chosen as one of the six prime advanced candidate materials for use in fast breeder reactors. When compared to 316 stainless steel, HT-9 has been found to have comparable strength and better thermal stress resistance for temperatures less than 500°C.[3] The void swelling in HT-9 is an order-of-magnitude less than the void swelling observed in 20% cold worked 316 (20 CW 316),[4] and HT-9 exhibits higher in-reactor creep resistance than 20 CW 316.[5] Although the ferritic stainless steels are ferromagnetic, measurements of some of the magnetic properties of HT-9 and the results of rough calculations indicate that the magnetic effects of ferritic materials in a fusion reactor are relatively minor and can be accommodated in the reactor design.[3]

Except for irradiation creep, relatively little information has been gathered concerning the irradiation effects at high fluences upon the mechanical properties of ferritic alloys. Of particular concern are the fatigue initiated crack growth for these materials and their weld properties. The AD-2 experiment is designed to provide such baseline data. EBR-II has been chosen for the irradiation site because of its high fluence and available irradiation volume.

7.3.4.2 Description of Experiment

The AD-2 experiment consists of six B-7c pins each of which has been designed to contain one isothermal subcapsule. The irradiation temperatures chosen for investigation in this experiment are 390°C (743°F), 450°C (842°F), 500°C (932°F), and 550°C (1022°F). These desired irradiation temperatures are obtained by profiling the gas gap between the subcapsule and B-7c pin walls to give a controlled heat flow. The maximum subcapsule temperature will be recorded by thermal expansion device (TED) monitors located with the specimens inside the subcapsule. NaK will be used as the subcapsule thermal bonding agent.

To fully utilize available EBR-II reactor space, three pins will be irradiated with the National Clad/Duct AA-IIf experiment and the other three pins will be irradiated with the National Clad/Duct AA-XIV experiment. Both of these experiments are part of the Breeder Reactor Materials Development Program. Therefore, three pins designed for subcapsule temperatures of 390°C (743°F), 500°C (932°F), and 550°C (1022°F) will be inserted into

EBR-II at the beginning of Cycle 108; and the other three pins designed for subcapsule temperatures of 390°C (743°F), 450°C (842°F) and 500°C (932°F) will be inserted into EBR-II at the beginning of Cycle 109. The irradiation schedule is shown in Fig. 7.3.1.

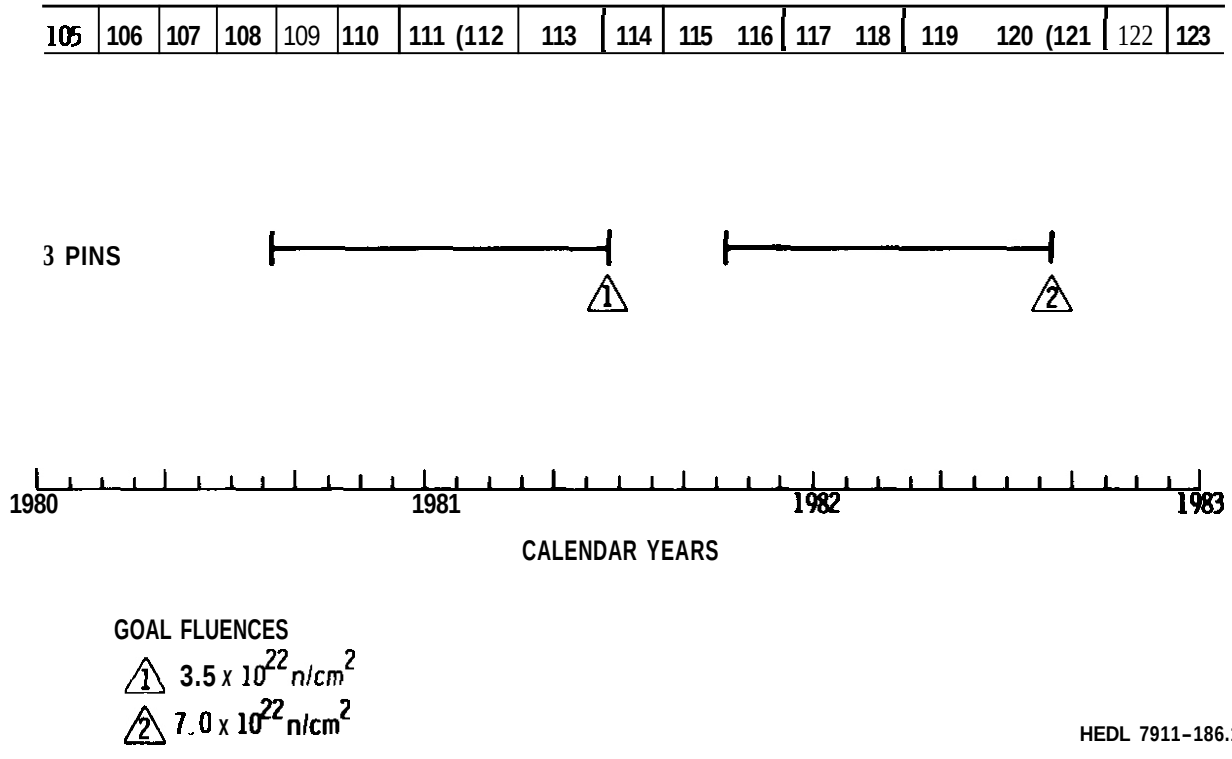

Fig. 7.3.1. Irradiation Schedule.

The anticipated examination schedule for the AD-2 experiment is also given in Fig. 7.3.1. Interim examination of the specimens is planned after goal fluences of 3.5 x 10^{22} n/cm^2 (E > 0.1 MeV). Interim examination and reencapsulation of the three pins inserted into Cycle 108 will occur after 112, and Cycle 113 will be missed. Interim examination and reencapsulation of the three pins inserted into Cycle 109 will occur after 113, and Cycles 114 and 115 will be missed. Final examination of the specimens is planned after fluences of 7.0 x 10^{22} n/cm^2 (E > 1.0 MeV) have been obtained.

The alloys chosen for investigation in the AD-2 experiment are given in Table 7.3.1. Each subcapsule will contain fatigue initiation, crack growth,

crack growth of welds, fracture toughness, fracture toughness of welds, Charpies, Charpies of welds, Grodzenski fatigue, tensile strength and transmission electron (TEM) disc specimens. The specimen loadings for each level within a subcapsule for the three pins to be inserted into Cycle 108 are given in Table 7.3.2 and the test matrix for these three pins is given in Table 7.3.3. Similarly, the specimen loadings for each level within a subcapsule for the three pins to be inserted into Cycle 109 are given in Table 7.3.4 and the test matrix for these three pins is given in Table 7.3.5.

7.3.4.3 Status of Experiment

Approval in principle has been granted for the AD-2 experiment by the Department of Energy.[1] Design of the B-7c pin hardware is complete and is in the process of being reviewed. Specimen and capsule hardware fabrication have been initiated.

Table 7.3.1. Alloy Selection for AD-2 Experiment

AD-2 Alloys	
Major Alloys	
HT-9 HT #1	1050°C/.5 Hr/AC + 780°C/2.5 Hr/AC
9Cr-1Mo	1040°C/1 Hr/AC + 760°C/1 Hr/AC
Minor Alloys	
HT-9 HT #2	1040°C/5 Min/AC + 760°C/30 Min/AC
2¼Cr-1Mo	To Be Determined

Table 7.3.2. Specimen Matrix for Insertion into EBR-II Cycle 108 Three B-7c Pins at 390°C(743°F), 500°C(932°F), and 550°C(1022°F)

	Level #	Distance From Center of Level to Core Midplane (in)	Specific Alloy Loading
3 FI 8 T 1 TED	1	6.22	3 FI HT-9 (HT #1) 5 T HT-9 (HT #2) 3 T 2¼Cr-1Mo
6 FT 6 FT(W)	2	4.27	6 FT HT-9 (HT #1) 6 FT(W) HT-9 (HT #1)
24 CG(W) 2 D	3	2.19	18 CG(w) HT-9 (HT #1) 6 CG(w) 9Cr-1Mo 2 D Disc Packets
26 CG 1 TED	4	0.0	11 CG HT-9 (HT #1) 5 CG HT-9 (HT #2) 5 CG 9Cr-1Mo 5 CG 2¼Cr-1Mo
8 C 5 T 2 D	5	-2.07	8 C HT-9 (HT #1) 5 T HT-9 (HT #1) 2 D Disc Packets
4 c 4 C(W) 7 GF 3 T	6	-4.02	4 C 9Cr-1Mo 4 C(W) HT-9 (HT #1) 5 GF HT-9 (HT #1) 2 GF 9Cr-1Mo 3 T 9Cr-1Mo
3 FI 8 T 1 TED	7	-5.97	3 FI 9Cr-1Mo 5 T HT-9 (HT #1) 3 T 9Cr-1Mo

Table 7.3.3. Table of Specimen Matrix For Fusion Materials Experiment AD-2 In EBR-II

3 B-7c Pins scheduled for insertion into Cycle 108

Temperatures: 390°C(743°F), 500°C(932°F), and 550°C(1022°F)

Major Alloys	Total Number of Specimens per Pin
HT-9 HT #1	8C, 4C(w), 11CG, 18CG(w), 3FI, 6FT, 6FT(w), 5GF, 10T*, 1½D (90 TEM)
9Cr-1Mo	4C, 5CG, 6CG(w), 3FI, 6T, 2GF, 1D (60 TEM)
Minor Alloys	
HT-9 HT #2	5CG, 5T, ½D (30 TEM)
2¼Cr-1Mo	5CG, 3T

*Each pin will contain one additional disc packet which will contain TEM discs from MIT.

C = Charpy
C(w) = Charpy of Weld
CG = Crack Growth
CG(w) = Crack Growth of Weld
FI = Fatigue Initiation
FT = Fracture Toughness
FT(w) = Fracture Toughness of Welds
GF = Grodzenski Fatigue
T = Tensile

Table 7.3.4. Specimen Matrix for Insertion into EBR-II Cycle 109
Three B-7c Pins at 390°C(743°F), 450°C(842°F), and 500°C(932°F)

	Level #	Center of Level to Core Midplane (in)	Specific Alloy Loading
3 FI 8 T 1 TED	1	6.22	3 FI HT-9 (HT #1) 5 T HT-9 (HT#2) 3 T 2¼Cr-1Mo
12 FT(w)	2	4.27	12 FT(w) HT-9 (HT #1)
6 FT 6 FT(w)	3	2.19	6 FT HT-9 (HT #1) 6 FT(w) 9Cr-1Mo
26 CG 1 TED	4	0.0	11 CG HT-9 (HT #1) 5 CG HT-9 (HT #2) 5 CG 9Cr-1Mo 5 CG 2¼Cr-1Mo
8 C 5 T 2 D	5	-2.07	8 C HT-9 (HT #1) 5 T HT-9 (HT #1) 2 D Disc. Packets
4 c 4 C(w) 5 GF 2 D	6	-4.02	4 C 9Cr-1Mo 4 C(w) HT-9 (HT #1) 5 GF HT-9 (HT #1) 2 D Disc Packets
3 FI 8 T 1 TED	7	-5.97	3 FI 9Cr-1Mo 5 T HT-9 (HT #1) 3 T 9Cr-1Mo

Table 7.3.5. Table of Specimen Matrix for Fusion Materials Experiment AD-2 *in* EBR-II

3 B-7c Pins scheduled for insertion into Cycle 109

Temperatures: 390°C(743°F), 450°C(842°F), and 500°C(932°F)

Major Alloys	Total Number of Specimens per Pin
HT-9 HT #1	8C, 4C(w), 11CG, 3FI, 6FT, 12FT(w), 5GF, 10T, 2½D (150 TEM)
9Cr-1Mo	4C, 5CG, 3FI, 6FT(w), 3T, 1D (60 TEM)
Minor Alloys	
HT-9 HT #2	5CG, 5T, ½D (30 TEM)
2¼Cr-1Mo	5CG, 3T

C = Charpy
C(w) = Charpy of Welds
CG = Crack Growth
CG(w) = Crack Growth of Welds
FI = Fatigue Initiation
FT = Fracture Toughness
FT(w) = Fracture Toughness of Welds
GF = Grodzenski Fatigue
T = Tensile

7.3.5 Conclusions and Future Work

The fusion AD-2 experiment has become well defined in the past few months. HT-9 has been chosen as the primary alloy under investigation. Irradiation temperatures have been agreed upon, and the test matrix has been specified. Design of the B-7c pins and their associated hardware has also been completed.

The future work necessary in this experiment is outlined in the schedule given in Table 7.3.6. Work is now progressing to insure that this schedule is kept.

Table 7.3.6. Schedule for AD-2 Experiment

	Cycle 108 Insertion	Cycle 109 Insertion
Design Complete	1/18/80	2/27/80
Fabrication Complete	4/2/80	5/28/80
Ship to EBR-II	5/1/80	6/25/80
Begin Irradiation	6/16/80	8/11/80
Remove for Interim Examination	3/15/81	6/7/81
Continue Irradiation	6/15/81	10/6/81
End Irradiation	3/82	8/82

7.3.6 References

1. Letter from D. K. Magnus (RRT) to C. S. Carlisle (HEDL) dated January 14, 1980.
2. L. D. Thompson and S. N. Rosenwasser, "Ferritic Stainless Steels for Fusion Applications," *ADIP Quarterly Progress Report*, June 30, 1979.
3. S. N. Rosenwasser, P. Miller, J. A. Dalessandro, J. M. Rawls, W. E. Toffolo, and W. Chen, "The Application of Martensitic Stainless Steels in Long Lifetime Fusion Wall/Blankets," *J. Nucl. Mater.* 85 & 86 (1979), p. 177-182.

4. F. A. Smidt, P. R. Malmberg, J. A. Sprague and J. G. Westmoreland, "Swelling Behavior of Commercial Ferritic Alloys, EM-12 and HT-9, as Assessed by Heavy Ion Bombardment," *Irradiation Effects on the Microstructure and Properties* of *Metals*, ASTM STF #61, American Society for Testing Materials, (1976) p. 227.

5. B. A. Chin, E. R. Gilbert, M. M. Paxton and J. L. Straalsund, "A Comparison of the In-Reactor Creep Behavior of Selected Commercial Alloys at a Temperature of 593°C," presented at the 9th ASTM International Symposium on the Effects of Irradiation on Structural Materials, Richland, WA July 1978.

7.4 ENVIRONMENTAL EFFECTS ON PROPERTIES OF FERRITIC STEELS - D. L. Smith, O. K. Chopra, and R. R. Schlueter (Argonne National Laboratory)

7.4.1 ADIP Task

Task I.A. 3. Corrosion and Compatibility

7.4.2 Objective

The objective of this work is to develop a data base on the corrosion, compatibility, and the influence of chemical environment on the mechanical properties of ferritic steels (including welds) under environmental conditions proposed in fusion reactor applications.

This program is part of a more comprehensive program to investigate the potential of ferritic steels for fusion reactor first-wall blanket structures. Test environments to be investigated include lithium, water, and helium with appropriate impurities as well as candidate solid breeding materials and neutron multipliers. Emphasis will be placed on the combined effect of stress and chemical environment. Initial tests will focus on the Sandvik Alloy HT-9 and a developmental Fe-9Cr-1Mo alloy.

7.4.3 Progress and Status

This program was initiated in the first quarter of FY 1980 with initial phases of the program focused on (1) combined effects of stress and coolant environment on the properties of ferritic steels and (2) the compatibility of ferritic steels with candidate solid tritium-breeding materials and neutron multipliers. The first experiments include determination of the effects of a liquid lithium environment on the fatigue properties of the Sandvik HT-9 alloy and tests on the compatibility of candidate ferritic steels with Li_2O and Li_2SiO_3.

Modification of existing equipment for fatigue testing ferritic steels in a lithium environment is in progress. The system to be used is similar to the systems used previously for fatigue testing in liquid sodium.' The system consists of a servocontrolled, hydraulic actuated MTS fatigue machine with an associated liquid metal loop. The loop is constructed of stainless steel and is equipped for control and measurement

of nonmetallic element concentrations in the lithium. The lithium will be circulated through hot traps or cold traps as desired to establish oxygen, nitrogen, carbon, and hydrogen concentrations within limits of capability.

The grips of the fatigue machine have been modified to accommodate the small test specimens to be used. Figure *7.4.1* shows the geometry and dimensions of the test and calibration specimens to be used in the present investigation. The specimen size has been made similar to that used at ORNL for the irradiation tests in HFIR.[2] The diameter of the corrosion test specimens is slightly smaller than the irradiation test specimens because the available HT-9 ferritic alloy material was in the form of 6.4-mm-diameter (0.25 in.) rod. Preliminary tests have been run with small size Type 304 stainless steel and HT-9 specimens in sodium to check out the test ranges for load and strain and to qualify the test procedures. Results will be compared with previous tests to ensure the validity of results obtained with the small sample geometry,

The second phase of the program that has been initiated involves the compatibility testing of ferritic steels with candidate solid breeding materials. Corrosion specimens have been fabricated from Fe-9Cr-1Mo and Fe-2¼Cr-1Mo. Samples will be fabricated from HT-9 when material becomes available from General Atomic Company through the Ferritic Steel Development Program. The compatibility tests will he performed in cooperation with the Solid Breeder Development Program conducted in the Chemical Engineering Division. Initial tests will be with Li_2O and Li_2SiO_3 at 600°C.

7.4.4 Conclusions

A program was initiated in the first quarter of FY 1980 to investigate the effects of a lithium environment on the fatigue properties of ferritic steels.

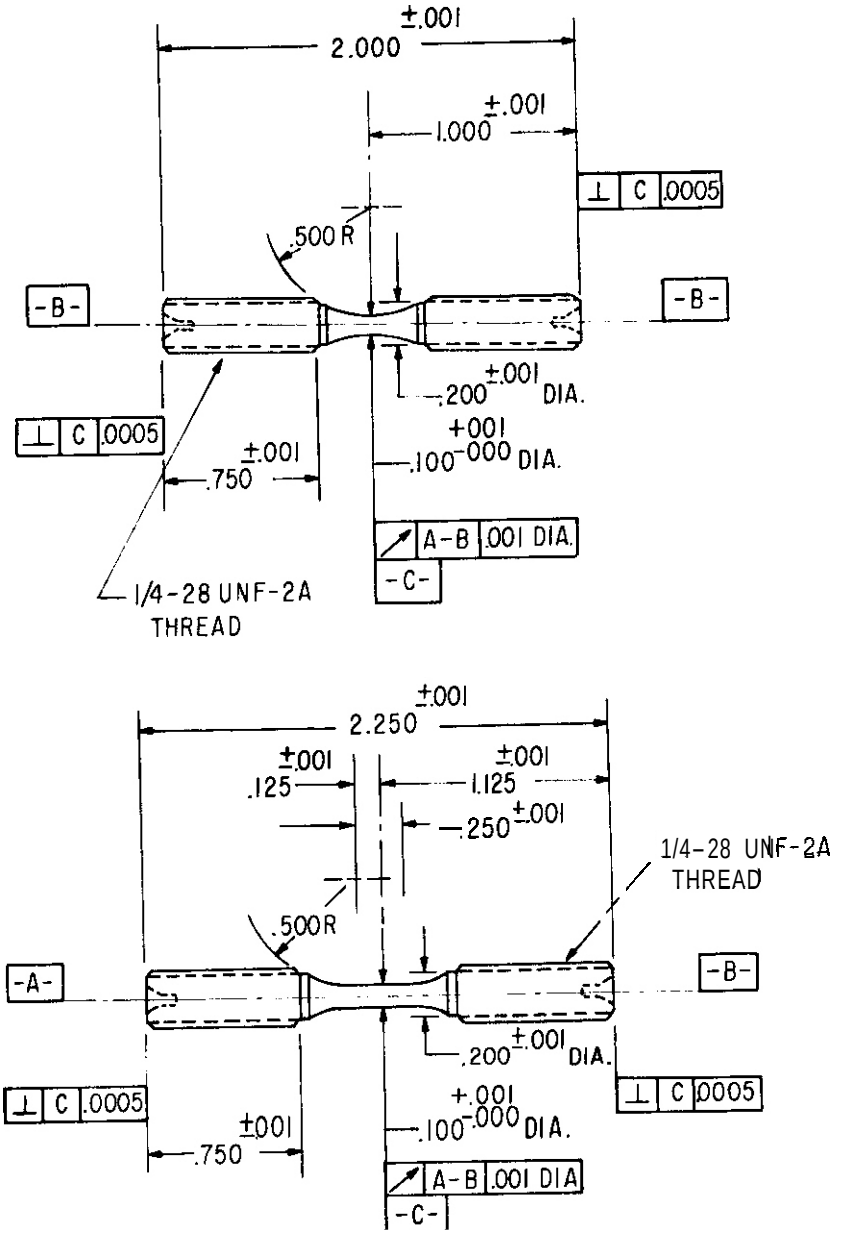

Fig. 7.4.1. Gauge Length and Hourglass Fatigue Specimens. All dimensions are in inches. Conversion factor: 1 in. = 25.4 mm.

References

1. D. L. Smith et al., "Effects of Sodium on the Low-Cycle Fatigue Behavior of Austenitic Stainless Steel," Proc. ASME Symp. on Structural Materials for Service at Elevated Temperatures in Nuclear Power Generation, MPC-1, pp. 290-301, American Society of Mechanical Engineers (1975).

2. M. L. Grossbeck and M. J. Kania, "HFIR Irradiation of Hourglass Fatigue Specimens," ADIP Quarterly Progress Report, March 31, 1978, DOE/ET-0058/2, pp. 20-35.

8. STATUS OF IRRADIATION EXPERIMENTS AND MATERIALS INVENTORY

8.1 IRRADIATION EXPERIMENT STATUS AND SCHEDULE

The following bar charts show the irradiation experiment schedule, including experiments completed, in progress, and planned. Experiments are presently under way in the ORR and the RFIR, which are mixed-spectrum reactors, and in the EBR-II, which is a fast reactor.

Specimens from EBR-II subassembly X287 are being sorted and shipped to participating laboratories. Pin B284 of subassembly X217D was removed from the EBR-11 in October.

ORR-MFE-2 and HFIR-CTR-26, -27, -28, and -29 are in the ORR and HFIR, respectively, and are performing satisfactorily.

Components for ORR-WE-4 are being manufactured, and some completed components are being bench tested.

Experiment Designation	Major Objective
A. Oak Ridge Research Reactor	
ORR-MFE-1 / ORR-MFE-2	Experiments to scope the effects of composition and microstructure on the tensile, fatigue, and irradiation creep of representative path A, B, and C alloys.
ORR-MFE-3	Effects of irradiation on postirradiation fatigue crack growth in representative path A, B, and C alloys.
ORR-MFE-4	Effect of irradiation on tensile, fatigue, and irradiation creep of path A PCA (Prime Candidate Alloy) and path B base research alloys. Spectral tailoring to maintain correct He/dpa ratio. Irradiation on continuing basis.

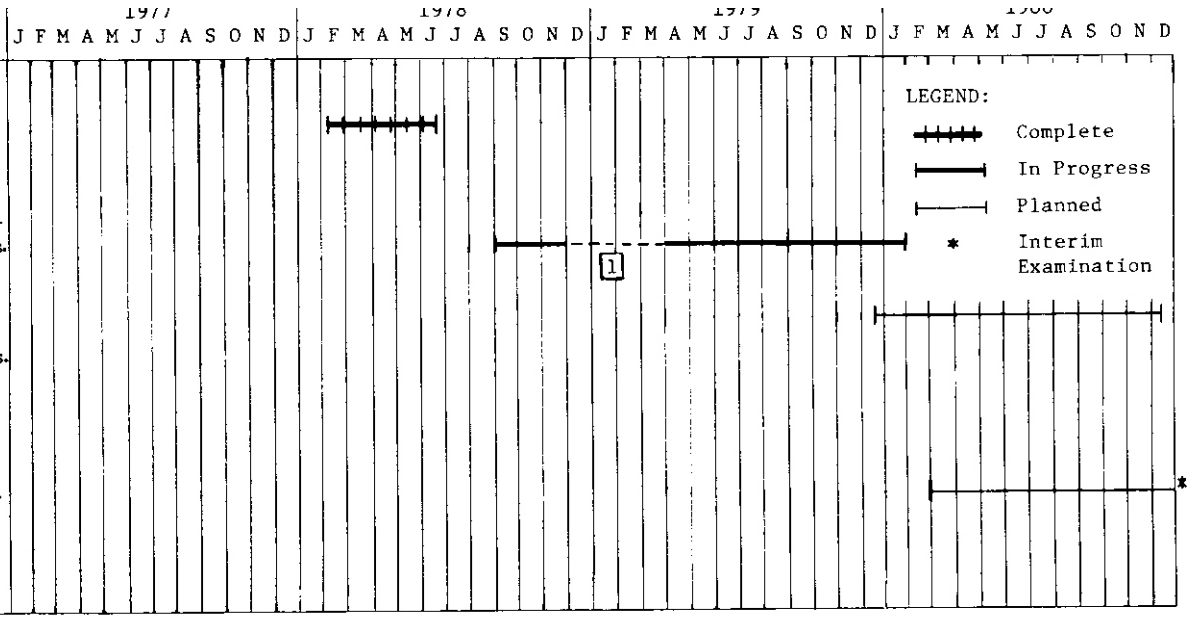

[1] MFE-2 out of reactor for repair of a small leak.

Experiment Designation	Major Objective
ORR-MFE-5	In-reactor fatigue crack growth experiment
B. Experimental Breeder Reactor II	
Subassembly X 264	Effect of preinjected helium (2—200 at. ppm) on microstructure and tensile properties of 316 SS, PE-16, V and Nb alloys. Fluence $\leq 2.3 \times 10^{26}$ n/m^2, 500—825°C.
Subassembly X 287	Effect of preinjected helium (2—200 at. ppm He) on microstructure and tensile properties of 316 SS, PE-16, V and Nb alloys. Fluence $\leq 4 \times 10^{26}$ n/m^2, 400—700°C.
Subassembly X 217D	Stress relaxation Ti Alloys
See footnotes [1] [2] and [3]	Effect of irradiation on swelling, tensile, fatigue, and crack growth properties of Ti scoping alloys. 370, 450, and 550°C, fluence 4.5—5.5 × 10^{26} n/m^2.

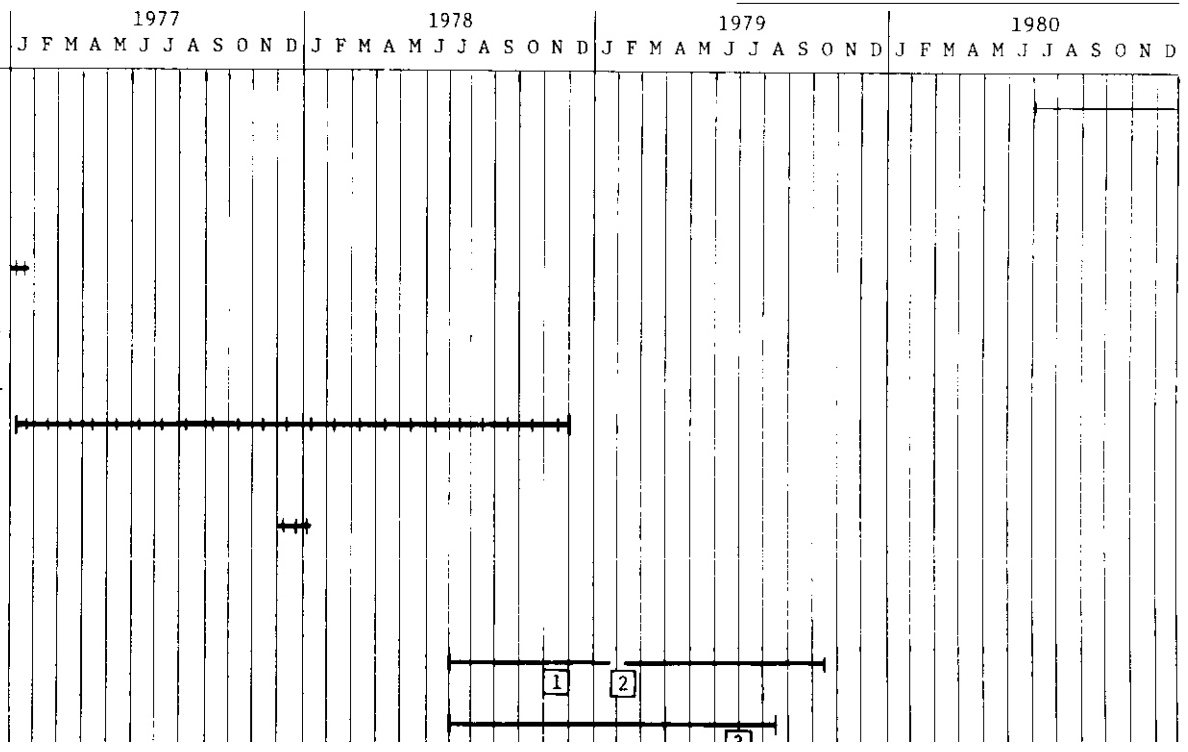

[1] EBR-II, row 2, pins B285 and B286.

[2] Subassembly removed for EBR-II run 99.

[3] Pin B284, row 2 for runs 96—98; row 4 for runs 100—102.

Experiment Designation	Major Objective
Experiment plan depends on alloy availability. EBR-II space not yet identified.	Effect of Irradiation on swelling, tensile, fatigue, and crack growth properties of V and Nb scoping alloys. 370, 450, 550, and 650°C. Position in reactor not finalized, therefore no fluence estimate. [1]
C. High Flux Isotope Reactor (HFIR)	
HFIR-CTR-4	PE-16 for swelling and tensile properties, 300–700°C 2.2–4.5 dpa, 100–350 at. ppm He
HFIR-CTR-7	PE-16 for swelling and tensile properties, 300–700°C 9–18 dpa, 1250–3000 at. ppm He
HFIR-CTR-8	duplicate of -7
HFIR-CTR-9	316 and 316 + Ti for swelling and tensile properties, 280–680°C, 9–18 dpa, 400–1000 at. ppm He

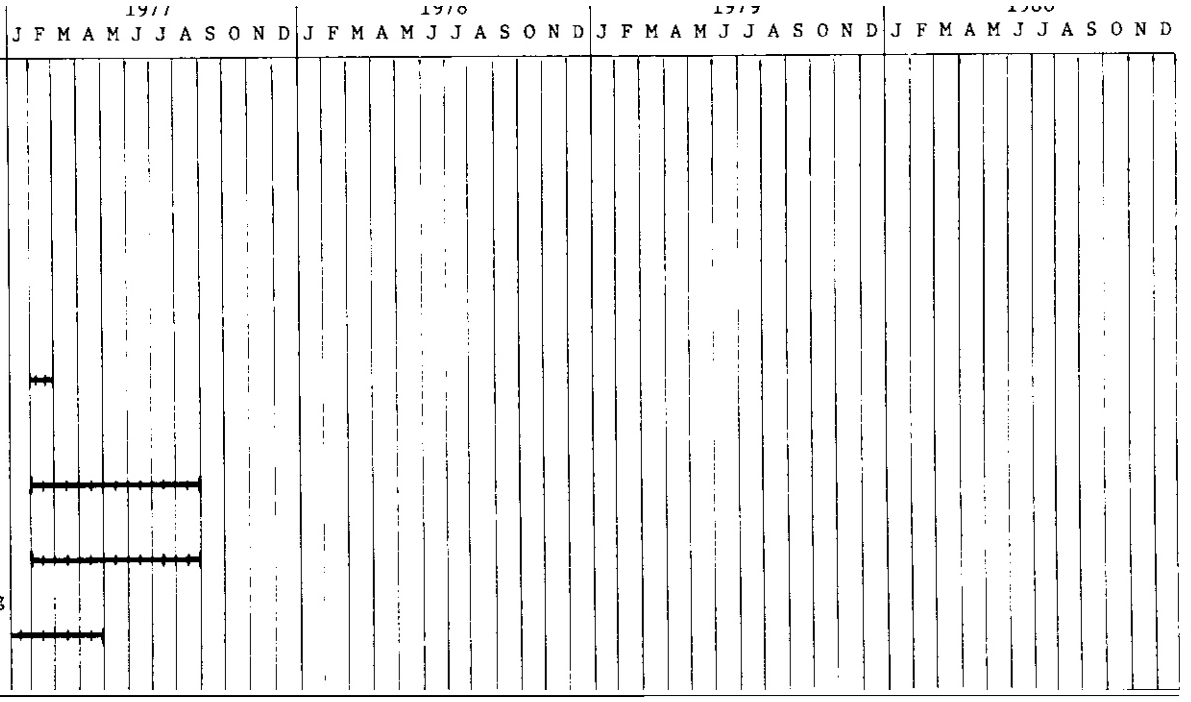

[1] Delayed for undetermined period.

Experiment Designation	Major Objective
HFIR-CTR-10	duplicate of -9
HFIR-CTR-11	duplicate of -9
HFIR-CTR-12	316 and 316 + Ti for swelling and tensile properties, 280–680°C, 5.5–11 dpa, 200–500 at. ppm He
HFIR-CTR-13	duplicate of -12
HFIR-CTR-14	20%-CW 316 for fatigue testing 300°C. 9–18 dpa, 400–1000 at. ppm He
HFIR-CTR-15	20%-CW 316 for fatigue testing 500°C, 5.5–11 dpa, 200–500 at. ppm He
HFIR-CTR-16	316, welds, PE-16, and Inconel 600 for swelling and tensile properties, ~55°C, 5.5–11 dpa, 150–2700 at. ppm He (depending on alloy)
HFIR-CTR-17	Type 316 welded with 16-8-2 filler metal for tensile properties and failure analysis, 280–620°C, 6.7–13 dpa, 180–460 at. ppm He in weld metal

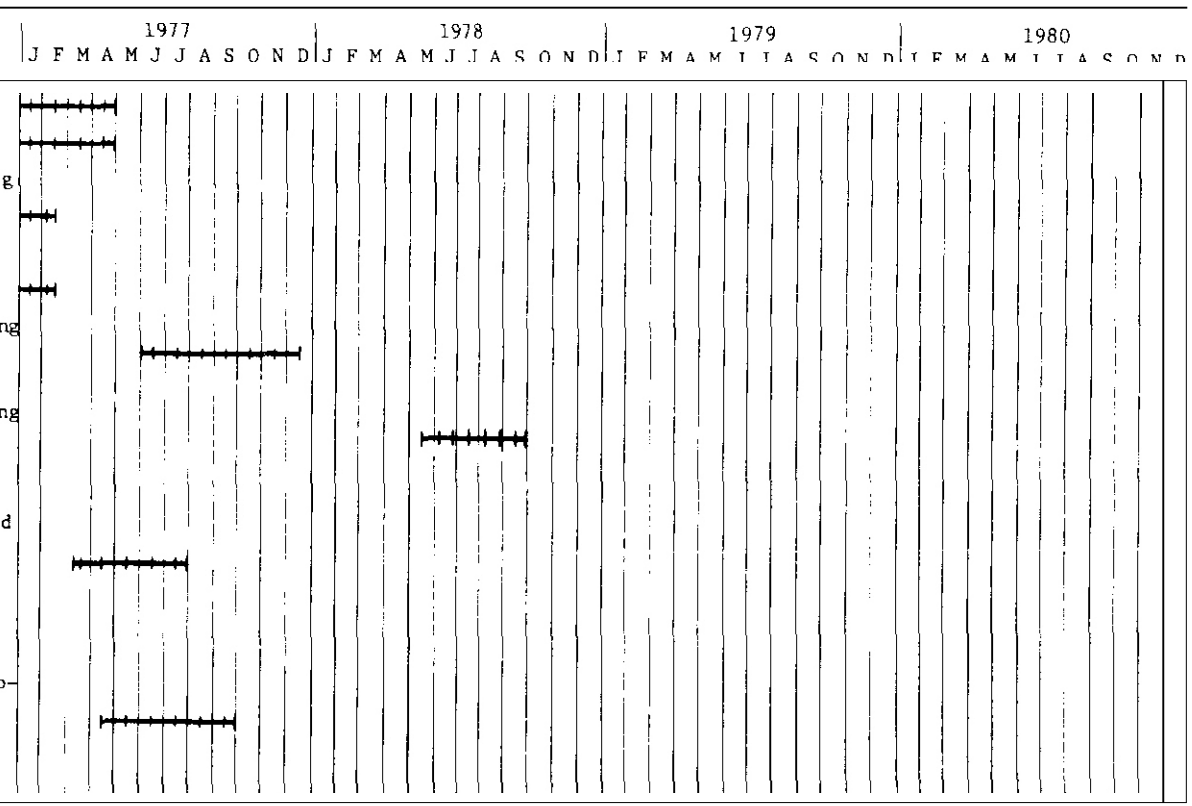

Experiment Designation	Major Objective
HFIR-CTR-18	PE-16 and 20%-CW type 316 for swelling and tensile properties, 280–700°C, PE-16: 17–27 dpa, 3400–5600 at. ppm He 316: 27–34 dpa, 1600–2100 at. ppm He
HFIR-CTR-19	316 welded with 316 filler metal for tensile properties, 280–620°C, 5.5–11 dpa, 200–500 at. ppm He
HFIR-CTR-20	20%-CW 316 for fatigue testing, 300°C, 5.5–11 dpa, 200–500 at. ppm He
HFIR-CTR-21	20%-CW 316 for fatigue testing, 500°C, 9–18 dpa, 400–1000 at. ppm He
HFIR-CTR-22	duplicate of -20
HFIR-CTR-23	PE-16 for fatigue testing, 300°C, 4.4–9 dpa, 370–1000 at. ppm He

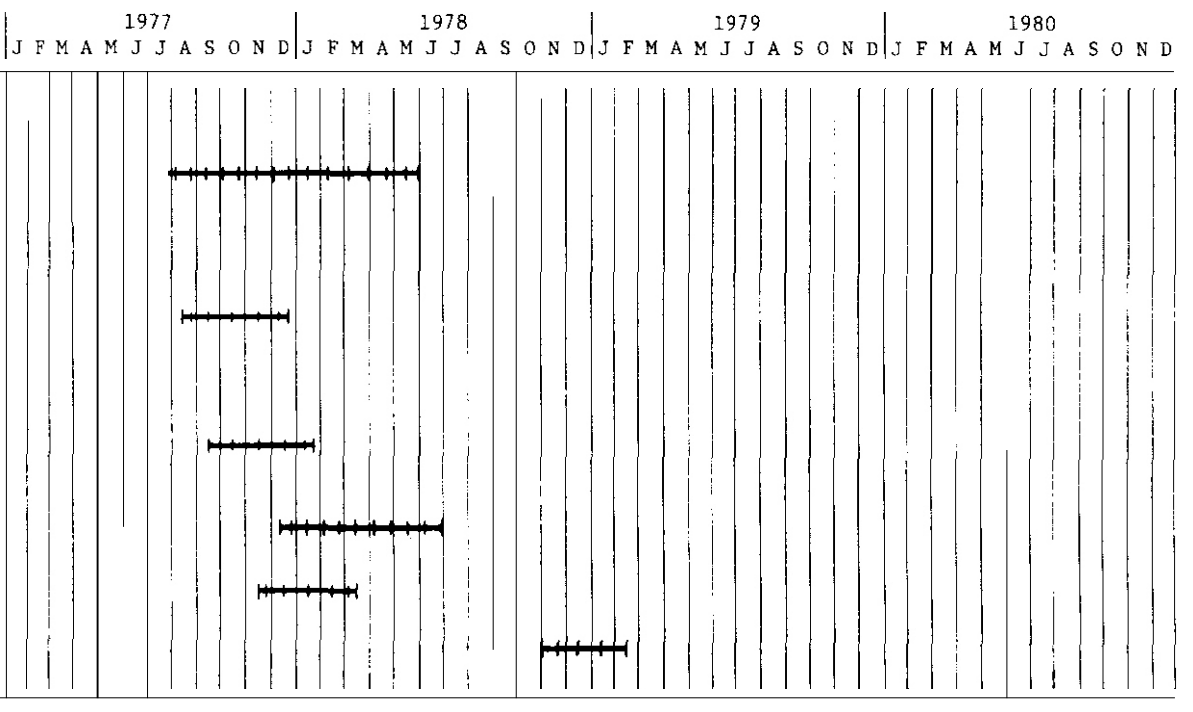

Experiment Designation	Major Objective
HFIR-CTR-24	Temperature calibration, tensile properties of MFE ref. 316, 2.25 dpa, 30 at. ppm He
HFIR-CTR-25	Temperature calibration, tensile properties of MFE ref. 316, 2.25 dpa, 30 at. ppm He [1]
HFIR-CTR-26	Swelling and tensile properties of MFE ref. 316, 32 dpa, 1900 at. ppm He
HFIR-CTR-27	Swelling and tensile properties of MFE ref. 316, 56 dpa, 3450 at. ppm He
HFIR-CTR-28	Swelling and tensile properties of MFE ref. 316, 32 dpa, 1900 at. ppm He
HFIR-CTR-29	Swelling and tensile properties of MFE ref. 316, 56 dpa, 3450 at. ppm He
HFIR-CTR-30	Swelling and tensile properties, Paths A, B, and D microstructural variations, 40 dpa, 2500 at. ppm He (Path A)
HFIR-CTR-31	Swelling and tensile properties, Paths A, B and D microstructural variations, 20 dpa, 1200 ppm He (Path A)
HFIR-CTR-32	Swelling and tensile properties, Paths A, B and D microstructural variations, 10 dpa, 500 ppm He (Path A)

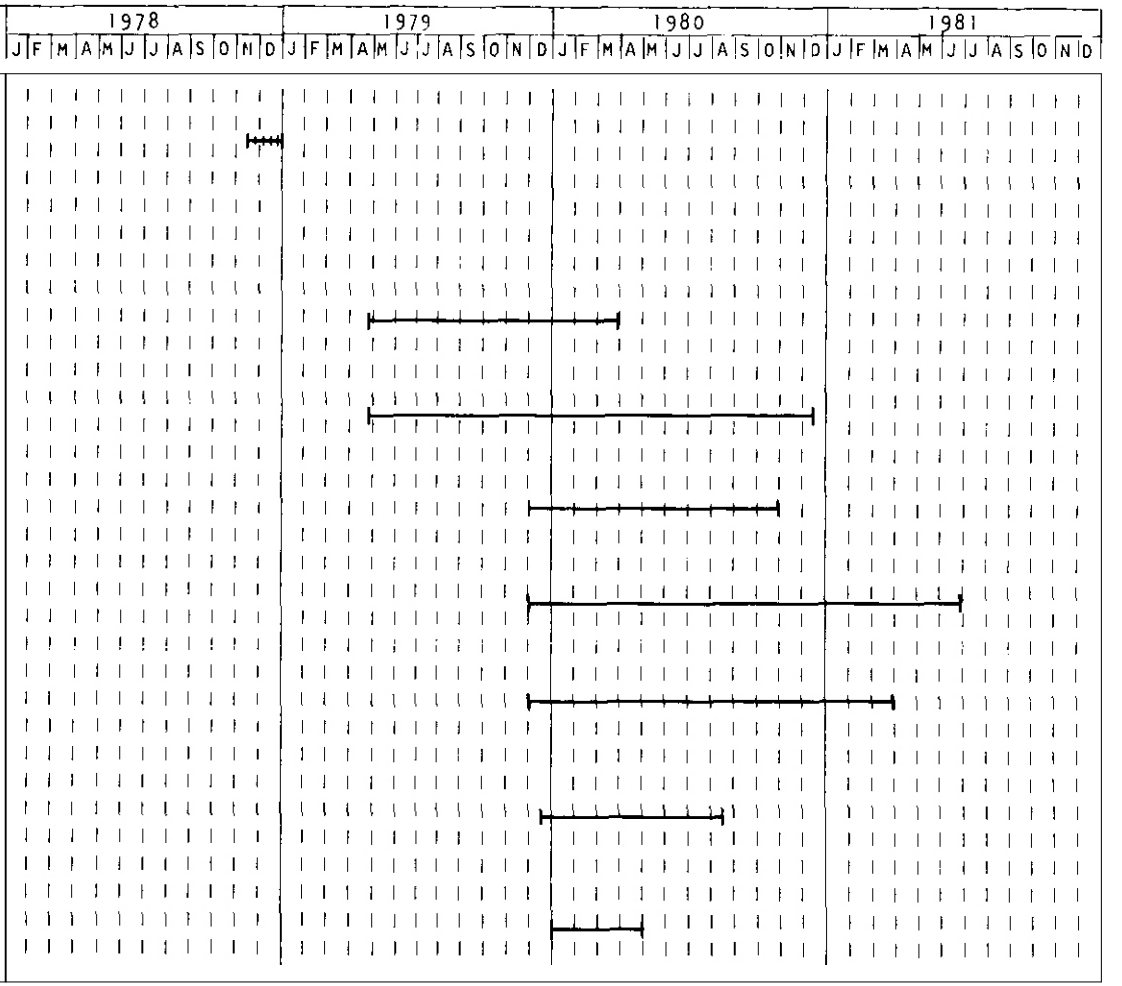

[1] Delayed for undetermined period.

8.2 ETM RESEARCH MATERIALS INVENTORY — F. W. Wiffen, T. K. Roche (ORNL) and J. W. Davis (McDonnell Douglas)

8.2.1 ADIP Task

ADIP Task I.D.l, Materials Stockpile for MFE Programs.

8.2.2 Purpose and Scope

The Office of Fusion Energy has assigned program responsibility to ORNL for the establishment and operation of a central inventory of research materials to be used in the Fusion Reactor Materials research and development programs. The objective is to provide a common supply of materials for the Fusion Reactor Materials Program. This will minimize unintended materials variables and provide for economy in procurement and for centralized recordkeeping. Initially this inventory is to focus on materials related to first-wall and structural applications and related research, but various special purpose materials may be added in the future.

The use of materials from this inventory for research that is COOKdinated with or otherwise related technically to the Fusion Reactor Materials Program of DOE, but which is not an integral or directly funded part of it, is encouraged.

8.2.3 Materials Requests and Release

Materials requests shall be directed to ETM Research Materials Inventory at ORNL (Attention: F. W. Wiffen). Materials will be released directly if:

(a) The material is to be used for programs funded by the Office of Fusion Energy, with goals consistent with the approved Materials Program Plans of the Materials and Radiation Effects Branch.

(b) The requested amount of material is available, without compromising other intended uses.

Materials requests that do not satisfy both (a) and (b) will be discussed with the staff of the Materials and Radiation Effects Branch, Office of Fusion Energy, for agreement on action.

8.2.4 Records

Chemistry and materials preparation records are maintained for all inventory material. All materials supplied to program uses will be accompanied by summary characterization information.

8.2.5 Summary of Current Inventory and Material Movement in Period Oct. 1, 1978, to Dec. 31, 1979

A condensed, qualitative description of the content of materials in the ETM Research Materials Inventory is given in Table 8.2.1. This table indicates the nominal diameter of rod or thickness of sheet for product forms of each alloy and also indicates by weight the amount of each alloy in larger sizes available for fabrication to produce other product forms as needed by the program. Table 8.2.2 lists materials received into the inventory in the 15-month period covered. Materials distributed from the inventory are listed in Table 8.2.3.

Alloy compositions and more detail on the alloys and on alloy procurement and/or fabrication are given in earlier ADIP quarterly progress reports.

Table 8.2.1. Summary Status of Material Availability in the ETM Research Materials Inventory

Alloy	Product Form			
	Ingot or Bar,[a] Weight (kg)	Rod,[b] Diameter (mm)	Sheet,[c] Thickness (mm)	Thin-Wall Tubing, Wall Thickness (mm)
		Path A Alloys		
316 SS	900	16 and 7.2	13 and 7.9	0.25
PCA	490	12	13	0
		Path B Alloys		
PE-16	140	16 and 7.1	13 and 1.6	0.25
B-I	180	0	0	0
B-2	180	0	0	0
B-3	180	0	0	0
B-4	180	0	0	0
B-6	180	0	0	0
		Path C Alloys		
Ti-64	0	0	0.76	0
Ti-6242s	0	0	0.76	0
Ti-5621s	0	0	6.3, 2.5, and 0.76	0
Ti-38644	0	0	0.76	0
Nb-1% Zr	0	6.3	2.5, 1.5, and 0.76	0
V-20% Ti	0	6.3	2.1, 1.5, and 0.76	0
V-15% Cr-5% Ti	0	6.3	2.5, 1.5, and 0.76	0
Vanstar-7	0	6.3	2.5, 1.5, and 0.76	0
		Path D Alloys — No Material in Inventory		
		Path E Alloys		
HT-9	0	0	4.5	0
HT-9 + 1% Ni	0	0	4.5	0
HT-9 + 2% Ni	0	0	4.5	0
HT-9 + 2% Ni + Cr adjusted	0	0	4.5	0
T-9 modified	0	0	4.5	0
T-9 modified + 2% Ni	0	0	4.5	0
T-9 modified + 2% Ni + Cr adjusted	0	0	4.5	0

[a] Greater than 25 mm, minimum dimension.

[b] Less than 25 mm in diameter. Some Path A and Path B alloys are available in two different diameters.

[c] Less than I5 mm thick. Some Path A, Path B, and Path C alloys are available in two or three different thicknesses.

Table 3 2 2 ETM Research Materials Inventory, Fusion Reactor Program, Receipts — 10-1-78 to 12-31-79

	Heat[a]	Product Form[b]	Dimensions (mm)	Dimensions (in.)	Quantity (kg)	Quantity (lb)	Quantity (m)	Quantity (ft)	Quantity (m^2)	Quantity ($in.^2$)	Quantity (pieces)	Source
			Path A Alloys — Austenitic Stainless Steels									
	X-15893	Tubing (20% cold worked)	4.57 OD × 0.254 wall	0.180 OD × 0.010 wall			25	82			15	Carpenter Technology
		Tubing (45% cold worked)	4.57 OD × 0.254 wall	0.180 OD × 0.010 wall			24	80			14	Carpenter Technology
	K-280	RCS bar	130 × 130 × 13	5 × 5 × 0.5							1	Teledyne Allvac
		Round bar	100	4	417	920						Teledyne Allvac
		Round bar	33	1 5/16	74	164	11	35				Teledyne Allvac
		Round bar	12.06	0.475	63	138	69	227				Teledyne Allvac
		Plate	13 thick × 130 wide	0.5 × 5	70	154	4.6	15				Teledyne Allvac
			Path B Alloys — High-Strength Fe-Ni-Cr Alloys									
PE-16	TC 1747	Tubing (20% cold worked)	4.57 OD × 0.254 wall	0.180 OD × 0.010 wall		12	41				10	Carpenter Technology
		Tubing	4.57 OD × 0.254 wall	0.180 OD × 0.010 wall		14	45				11	Carpenter Technology
B-1	J-270-1, -2	RCS bar	100	4	93	204					2	Teledyne Allvac
	J-271-1, -2	RCS bar	100	4	91	200					2	Teledyne Allvac
B-2	J-268-1, -2	RCS bar	100	4	98	217					2	Teledyne Allvac
	J-269-1, -2	RCS bar	100	4	99	219					2	Teledyne Allvac
B-3	J-266-1, -2	RCS bar	100	4	92	202					2	Teledyne Allvac
	J-267-1, -2	RCS bar	100	4	93	204					2	Teledyne Allvac
B-4	J-264-1, -2	RCS bar	100	4	92	202					2	Teledyne Allvac
	J-265-1, -2	RCS bar	100	4	93	204					2	Teledyne Allvac
B-6	J-262-1, -2	RCS bar	100	4	89	197					2	Teledyne Allvac
	J-263-1, -2	RCS bar	100	4	83	184					2	Teledyne Allvac

Table 8.2.2. (Continued)

Alloy	Heat[a]	Product Form[b]	Dimensions (mm)	Dimensions (in.)	(kg)	(lb)	(m)	(ft)	(m^2)	($in.^2$)	(pieces)	Source
			Path C Alloys — Reactive and Refractory Alloys									
V–20 Ti	832 Top	Rod	.35 diam	0.250			9.3	30'7"			18	Westinghouse
	832 Bot,833	Sheet	6 wide × 2.5 thick	3 × 0.10					0.15	235.9	14	Westinghouse
		Sheet	76 wide × 1.5 thick	3 × 0.06					0.20	308.1	6	Westinghouse
		Sheet	76 wide × 0.76 thick	3 × 0.03					0.21	330.2	5	Westinghouse
V–15 Cr–5 Ti	835 B	Rod	6.35 diam	0.250			7 8	25'9"			24	Westinghouse
	834,835 A	Sheet	76 wide × 2.5 thick	3 × 0.10					0.16	255.6	6	Westinghouse
		Sheet	76 wide × 1.5 thick	3 × 0.06					0.26	402.9	6	Westinghouse
		Sheet	76 wide × 0.76 thick	3 × 0.03					0.21	325.2	3	Westinghouse
Vanstar-7	836 Top	Rod	6.35 diam	0.250			7 6	24'9"			24	Westinghouse
	836 Bot,837	Sheet	76 wide × 2.5 thick	3 × 0.10					0.11	171.2	4	Westinghouse
		Sheet	76 wide × 1.5 thick	3 × 0.06					0.23	353.3	5	Westinghouse
		Sheet	76 wide × 0.76 thick	3 × 0.03					0.21	320.1	4	Westinghouse
Nb–1 Zr	839 Bot	Rod	6.35 diam	0.250			3 0	26'2"			19	Westinghouse
	838	Sheet	76 wide × 2.5 thick	3 × 0.10					0.14	218.8	4	Westinghouse
	838,839 Top	Sheet	76 wide × 1.5 thick	3 × 0.06					0.22	341.4	4	Westinghouse
		Sheet	76 wide × 0.76 thick	3 × 0.03					0.22	339.1	5	Westinghouse
Nb–5 Mo–1 Zr	841 Bot	Rod	6.35 diam	0.250			3 1	26'8"			18	Westinghouse
	840,841 Top	Sheet	76 wide × 2.5 thick	3 × 0.10					0.17	265.8	5	Westinghouse
	840	Sheet	76 wide × 1.5 thick	3 × 0.06					0.22	344.6	4	Westinghouse
	840,841 Top	Sheet	76 wide ×	3 ×					0.43	667.7	9	Westinghouse

Table 8.2.2. (Continued)

Alloy	Heat[a]	Product Form[b]	(mm)	(in.)	(kg)	(lb)	(m)	(ft)	(m^2)	($in.^2$)	(pieces)	Source
				Path E Alloys — Ferritic Steels								
HT-9	ESR-XAA-3587	Plate	356 × 114 × 4.83	14 × 4.5 × 0.190							1	Combustion Engineering
HT-9 + 1% Ni	ESR-XAA-3588	Plate	356 × 102 × 4.19	14 × 4 × 0.165							1	Combustion Engineering
HT-9 + 2% Ni	ESR-XAA-3589	Plate	356 × 114 × 4.55	14 × 4.5 × 0.179							1	Combustion Engineering
HT-9 + 2% Ni[d]	ESR-XAA-3592	Plate	356 × 102 × 0.175	14 × 4 × 0.175							1	Combustion Engineering
T-9 modified	ESR-XA-3590	Plate	356 × 114 × 3.99	14 × 4.5 × 0.157							1	Combustion Engineering
T-9 modified + 2% Ni	ESR-XA-3591	Plate	356 × 114 × 4.19	14 × 4.5 × 0.165							1	Combustion Engineering
T-9 modified + 2% Ni[d]	ESR-XA-3593	Plate	356 × 114 × 4.52	14 × 4.5 × 0.178							1	Combustion Engineering

[a]Bot — bottom.

[b]RCS — round-cornered square.

[c]Reference heat.

[d]With chromium equivalent adjusted.

Table 8.2.3. ETM Research Materials Inventory, Fusion Reactor Program, Disbursements — 10-1-78 to 12-31-79

Heat[a]	Product Form[b]	Dimensions (mm)	Dimensions (in.)	Quantity (kg)	Quantity (lb)	Quantity (m)	Quantity (ft)	Quantity (m^2)	Quantity ($in.^2$)	Quantity (pieces)	Sent to[c]
		Path A Alloys -- Austenitic Stainless Steels									
X-15893	Bar	102 diam	4	51.7	114	0.79	31"				MIT
	Bar	17 diam	0.66	0.26	0.57	0.14	5.7"				HEDL
	Bar	15.9 diam	0.625			9.2	30'4"				Metals Processing Group, M and C
	Plate	610 × 102 × 7.95	24 × 4 × 0.313							6	Metals Processing Group, M and C
	Sheet (20% cold worked)	0.76 thick	0.030					0.26	405		Radiation Effects Group, M and C
	Rod (20% cold worked)	6.35 diam	0.250			2.4	7'10"				HEDL
	Sheet (20% cold worked)	0.76 thick	0.030					0.06	100		HEDL
	Tubing (20% cold worked)	4.57 OD × 0.254 wall	0.180 × 0.010			1.8	5'10"				HEDL
	Tubing (46% cold worked)	4.57 OD × 0.254 wall	0.180 × 0.010			2.1	6'10"				HEDL
	Tubing (20% cold worked)	4.57 OD × 0.254 wall	0.180 × 0.010			1.8	5'11"				Radiation Effects Group, M and C
	Rod (19% cold worked)	5.38 diam	0.212			1.2	4				Radiation Effects Group, M and C
	Rod (50% cold worked)	7.95 diam	0.313			23	75'4"			41	USSR
	Sheet (50% cold worked)	51 wide × 1.9 thick	2 × 0.075					0.71	1100	50	USSR

Table 8.2.3. (Continued)

Alloy	Heat[a]	Product Form[b]	Dimensions (mm)	Dimensions (in.)	Quantity (kg)	Quantity (lb)	Quantity (m)	Quantity (ft)	Quantity (m^2)	Sent to[c]
PCA	K-280	RCS Bar	127 × 127 × 13	5 × 5 × 0.5	0.28	0.62				HEDL
		Bar	102 d	4	26	58	0.41	16"		MIT
		Bar	12.1	0.475			9.2	36		Metals Processing Group, M and C
		Plate	762 × 127 × 13	30 × 5 × 0.5						Metals Processing Group, M and C
		Bar	33.4 diam	1.313			2.1	6		Metals Processing Group, M and C
		Rod	6.35	0.250			2.4	8		Radiation Effects Group, M and C
		Rod	5.69	0.224			7.3	24		Radiation Effects Group, M and C
		Sheet	0.76 thick	0.030					.064	Radiation Effects Group, M and C
		Sheet	0.61 thick	0.024					.0064	HEDL
		Path B Alloys — High-Strength Fe-Ni-Cr Alloys								
B-1	J-271-1	RCS Bar	102	4	45.3	100				Metals Processing Group, M and C
		Bar	51 × 79 × 20	2 × 3.1 × 0.8	0.68	1.5				HEDL
		Sheet	305 × 76 × 0.61	12 × 3 × 0.024						HEDL
		Sheet	51 × 76 × 1.3	2 × 3 × 0.050						Materials Compatibility Group, M and C
		Sheet	203 × 76 × 1.3	8 × 3 × 0.050						Materials Compatibility Group, M and C
B-2	J-268-2	RCS Bar	102	4	49.0	108				Metals Processing Group, M and C
		Bar	51 × 79 × 20	2 × 3.1 × 0.8	0.68	1.5				HEDL
		Sheet	305 × 76 × 0.61	12 × 3 × 0.024						HEDL
		Sheet	51 × 76 × 1.3	2 × 3 × 0.050						Materials Compatibility Group, M and C

Table 8 2.3. (Continued)

Alloy	Heat[a]	Product Form[b]	Dimensions (mm)	Dimensions (in.)	Quantity (kg)	Quantity (lb)	Quantity (m)	Quantity (ft)	Quantity (m^2)	Quantity ($in.^2$)	Quantity (pieces)	Sent to[c]
B-3	J-267-1	RCS Bar	102	4	46.2	120						Metals Processing Group, M and C
		Bar	51 × 79 × 20	2 × 3.1 × 0.8	0.68	1.5					1	HEDL
		Sheet	305 × 76 × 0.61	12 × 3 × 0.024							2	HEDL
		Sheet	51 × 76 × 1.3	2 × 3 × 0.050							2	Materials Compatibility Group, M and C
		Sheet	203 × 76 × 1.3	8 × 3 × 0.050							1	Materials Compatibility Group, M and C
B	J 64 1	RCS Bar	102	4	45.8	101						Metals Processing Group, M and C
		Bar	51 × 79 × 20	2 × 3.1 × 0.8	0.68	1.5					1	HEDL
		Sheet	305 × 76 × 0.61	12 × 3 × 0.024							2	HEDL
		Sheet	51 × 76 × 1.3	2 × 3 × 0.050							2	Materials Compatibility Group, M and C
B 5	J 62 1	RCS Bar	102	4	44.4	98						Metals Processing Group, M and C
		Bar	51 × 79 × 20	2 × 3.1 × 0.8	0.68	1.5					1	HEDL
		Sheet	305 × 76 × 0.61	12 × 3 × 0.024							2	HEDL
		Sheet	51 × 76 × 1.3	2 × 3 × 0.050							2	Materials Compatibility Group M and C

Table 3 2 3 (Continued)

	Heat[a]	Product Form[b]	Dimensions (mm)	Dimensions (in.)	Quantity (kg)	Quantity (lb)	Quantity (m)	Quantity (ft)	Quantity (m^2)	Quantity ($in.^2$)	Quantity (pieces)	Sent to[c]
			Path C Alloys — Reactive and Refractory Alloys									
	832 Top	Rod	6.35 diam	0.250			1.1	[illegible]				Mechanical Properties Group, M and C
Ti	835 Bot	Rod	6.35 diam	0.250			1.3	4 [illegible]				Mechanical Properties Group, M and C
	836 Top	Rod	6.35 diam	0.250			1.3	4'2"				Mechanical Properties Group, M and C
	839 Bot	Rod	6.35 diam	0.250			1.3	[illegible]				Mechanical Properties Group, M and C
Zr	841 Bot	Rod	6.35 diam	0.250			1.3	4 5				Mechanical Properties Group, M and C
			Path E Alloys — Ferritic Steels									
	ESR-XAA-3587	Plate	356 × 114 × 4.8	14 × 4.5 × 0.190							1	Metals Processing Group, M and C
		Sheet	635 × 51 × 0.76	25 × 2 × 0.030							1	Radiation Effects Group, M and C
		Sheet	965 × 51 × 0.25	38 × 2 × 0.010							1	Radiation Effects Group, M and C
Ni	ESR-XAA-3588	Plate	356 × 102 × 4.19	14 × 4 × 0.165							1	Metals Processing Group, M and C
		Sheet	559 × 51 × 0.76	22 × 2 × 0.030							1	Radiation Effects Group, M and C
		Sheet	838 × 51 × 0.25	33 × 2 × 0.010							1	Radiation Effects Group, M and C

Table 8.2.3. (Continued)

Alloy	Heat[a]	Product Form[b]	Dimensions (mm)	Dimensions (in.)	Quantity (kg)	Quantity (lb)	Quantity (m)	Quantity (ft)	Quantity (m^2)	Quantity ($in.^2$)	Quantity (pieces)	Sent to[c]
HT-9 + 2% Ni	ESR-XAA-3589	Plate	356 × 114 × 4.55	14 × 4.5 × 0.179							1	Metals Processing Group, M and C
		Sheet	610 × 51 × 0.76	24 × 2 × 0.030							1	Radiation Effects Group, M and C
		Sheet	762 × 51 × 0.30	30 × 2 × 0.012							1	Radiation Effects Group, M and C
HT-9 + 2% Ni[e]	ESR-XAA-3592	Plate	356 × 102 × 4.44	14 × 4 × 0.175							1	Metals Processing Group, M and C
		Sheet	584 × 51 × 0.76	23 × 2 × 0.030							1	Radiation Effects Group, M and C
		Sheet	889 × 51 × 0.25	35 × 2 × 0.010							1	Radiation Effects Group, M and C

[a] Bot — bottom.

[b] RCS — round-cornered square.

[c] MIT — Massachusetts Institute of Technology; HEDL — Hanford Engineering Development Laboratory; M and C — Metals and Ceramics Division, Oak Ridge National Laboratory.

[d] Reference heat.

[e] With chromium equivalent adjusted.

9. CORROSION TESTING AND HYDROGEN PERMEATION STUDIES

9.1 HYDROGEN DISSOLUTION AND PERMEATION STUDIES OF ADIP PROGRAM ALLOYS — E. H. Van Deventer, A. G. Rogers, and V. A. Maroni (Argonne National Laboratory).

9.1.1 ADIP Task

I.A.4 Hydrogen Dissolution and Permeation Effects.

The results presented in this section contribute to Subrtask I.A.4., Milestones I.A.a through I.A.d.

9.1.2 Objectives

The objective of the work reported in this section is to provide base-line hydrogen dissolution and permeation data for alloys currently under study in the ADIP Program. The hydrogen dissolution, outgassing and permeation characteristics of these materials are vital to an understanding of their performance as first-wall and blanket structural materials for fusion devices. A further objective of this work is to begin examining methods for overcoming any serious hydrogen isotope uptake and migration problems associated with the rather strong hydride-forming nature of some classes of alloys.

9.1.3 Summary

Efforts to characterize the hydrogen dissolution and permeation characteristics of alloys currently under development in the ADIP Program have continued. An effort to measure the hydrogen permeabillity of pure a-titanium was generally unsuccessful owing to a tendance of the material to creep in

the gasket-seal-type assembly normally used for difficult-to-weld alloys. Work on the solubility of hydrogen in Ti-6Al-4V was completed. Based on these results, the amount of hydrogen dissolved in a Ti-6Al-4V fusion reactor first wall assembly could range from several hundred grams to a few kilograms, depending on the effective average T_2 pressure in the plasma boundary region and the first wall temperature distribution. Results of a survey of the hydrogen permeation characteristics of ferritic alloys showed that they are ∿5-times more permeable than 300-series stainless steels in the surface-unperturbed state, but that significant reductions in permeability can be achieved for oxidized aluminum-and chromium-containing ferritics.

9.1.4 Progress and Status

9.1.4.1 Path A Alloys

No report for this period.

9.1.4.2 Path B Alloys

No report for this period.

9.1.4.3 Path C Alloys

Work on the hydrogen dissolution and permeation characteristics of titanium-base alloys continued during the fourth quarter of FY 1979 and the first quarter of FY 1980. Efforts to measure the hydrogen permeabillity of pure a-titanium were unsuccessful. The gasket-sealing method[1] for preparing permeation assemblies, that had worked so well for the 5621S and 64 alloys,[1-3] was found to be unsuitable for pure titanium, owing to the fact that the a-titanium showed a tendency to creep and warp at elevated temperature (500 to 600°C), which caused a disruption of the gasket-seal. This creeping is apparently not a surprising observation for pure titanium,[4] and, quite interestingly, was not observed previously for the higher-strength 5621S and 64 alloys.

In another work area involving titanium alloys, the study of the solubility of hydrogen in Ti-6Al-4V was completed. The final set of four isotherms at 714, 614, 507, and 427°C is shown in Fig. 9.1.1. A plot of the temperature dependance of the Sieverts' constant for hydrogen dissolution in Ti-6Al-4V, obtained from the data in Fig. 9.1.1, is given in Fig. 9.1.2. Comparable data from Waisman et al.[5] are also shown in Fig. 9.1.2. Figures included in a prior report[2] of some of these data contain incorrect information. The results in Figs. 9.1.1 and 9.1.2 should be used in any further applications of the Ti-6Al-4V hydrogen solubility data.

Based on the data in Fig. 9.1.2, the solubility of hydrogen in Ti-6Al-4V is found to be approximately one-half the solubility of hydrogen in pure α-titanium,[6] but is still quite large from the standpoint of fusion reactor first wall applications. In a plasma/first wall boundary region where the time-averaged effective T_2 pressure is 10^{-4} torr and the average wall temperature is 400°C, the equilibrium tritium weight fraction in the first wall is likely to be close to 60 wppm (taking account of H/T isotope effects). The associated tritium inventory in the wall would then be at least several hundred grams, and could easily reach several kilograms if (1) the effective T_2 pressure were $>10^{-4}$ torr, (2) the average wall temperature was <400°C, and/or (3) implanted neutral tritons from the plasma were trapped to any significant degree inside the first wall structure.

9.1.4.4 Path D Alloys

No report for this period.

9.1.4.5 Path F Alloys

(Work reported in this subsection was initiated during the first quarter of FY 1980, in conjunction with the start of the ADIP Program activity to evaluate ferritic materials for use as fusion reactor construction materials.)

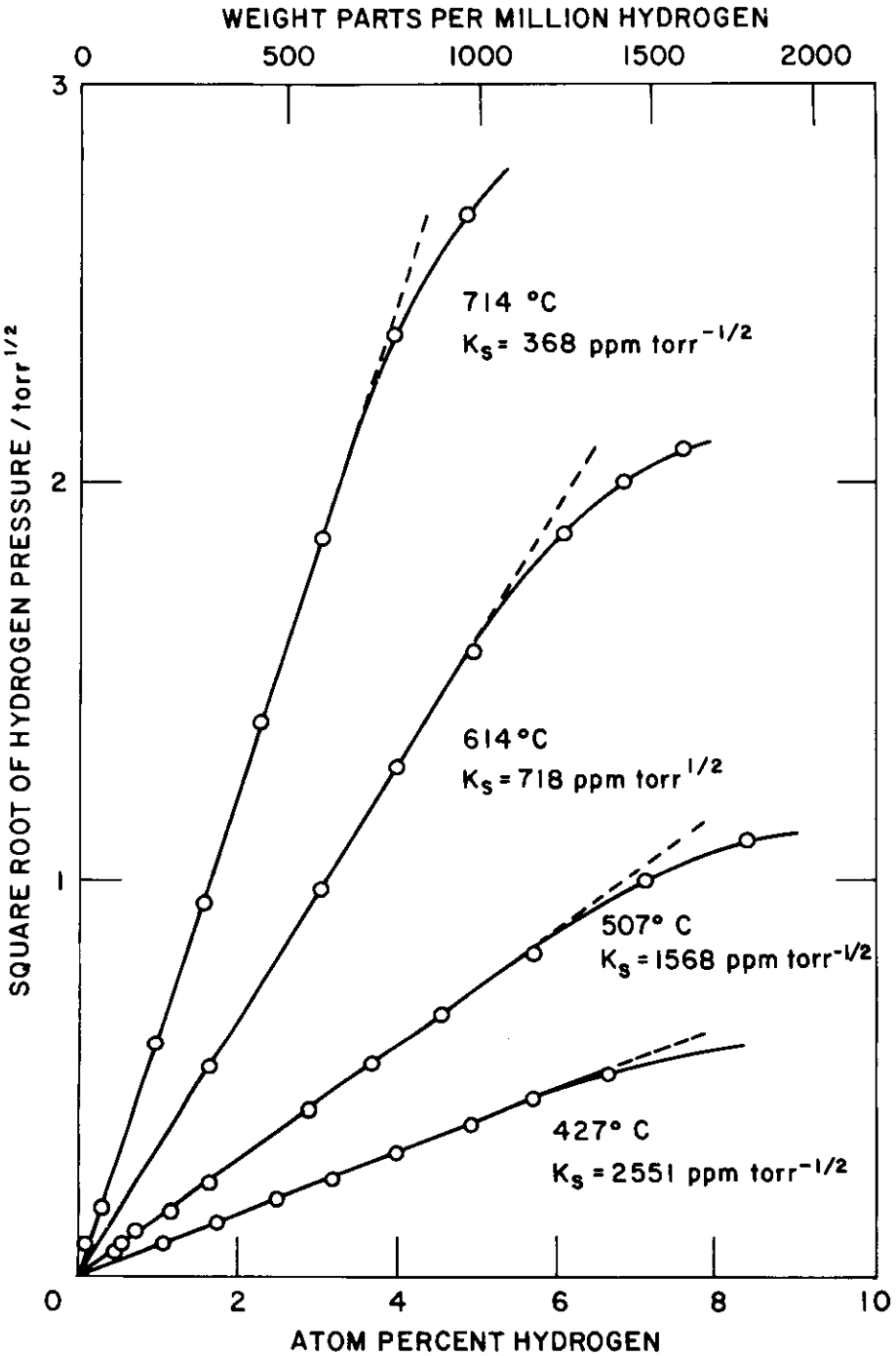

9.1.1 Sieverts' Law Constants for Hydrogen in the α-Phase of Ti-6Al-4V Alloy.

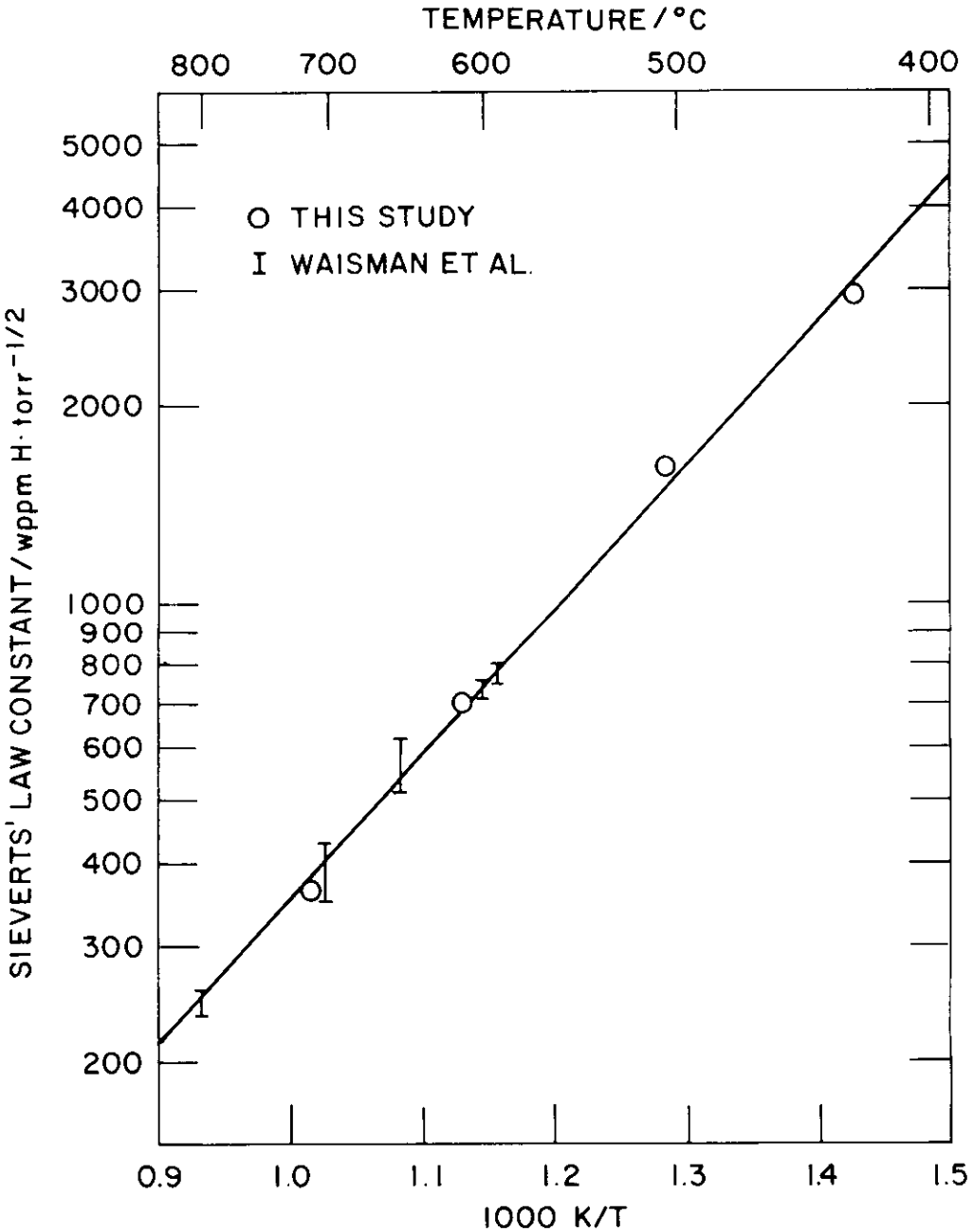

Fig. 9.1.2 Temperature Dependence of the Sieverts' Law Constant for Hydrogen in the α-Phase of the Ti-6Al-4V Alloy.

Ferritic steels have begun to receive attention as magnetic fusion reactor construction materials.[7] This interest is due to the generally improved mechanical properties of ferritic compared to austenitic steels and the finding that electromagnetic interactions with ferritics are not as severe as was once surmised due to the saturating effects of large dc magnetic fields. Accordingly, we have initiated an effort to characterize the data base for hydrogen dissolution in and permeation through ferritic materials. A survey of hydrogen permeation data for pure iron and ferritic alloys has been completed and a report describing the results of the survey is being drafted. The principal observations of the survey (see Fig. 9.1.3) were that the permeability of this class of materials if ∿5-times greater than that of 300-series SS, and significantly reduced permeation can be achieved for in-situ-oxidized aluminum-containing ferritic alloys and stearoxidized chromium-containing ferritics.

In parallel with the survey, an experimental permeation study of a developmental ferritic alloy, received from workers at Harwell in the UK, was initiated. This alloy (called Fecralloy), with the composition Fe-16Cr-5Al-0.3Y, should have a significantly reduced hydrogen permeability in the oxidized state because of the high aluminum content. Initial results indicate that its' hydrogen permeability is only slightly less than that of other ferritic steels, and not nearly as low as permeability results for an oxidized aluminum-modified 400-series stainless steel obtained previously in our laboratory.[8]

9.1.5 Conclusions

'Pure a-titanium was found to creep at elevated temperature in a gasket-seal-type permeation assembly, thwarting efforts to measure its' hydrogen permeability.

*Solubility data for hydrogen in Ti-6Al-4V indicate that the amount of dissolved tritium in a fusion reactor first wall fabricated from this material could range from several hundred grams to several kilograms, depending on effective T_2 activity and first wall temperature distribution.

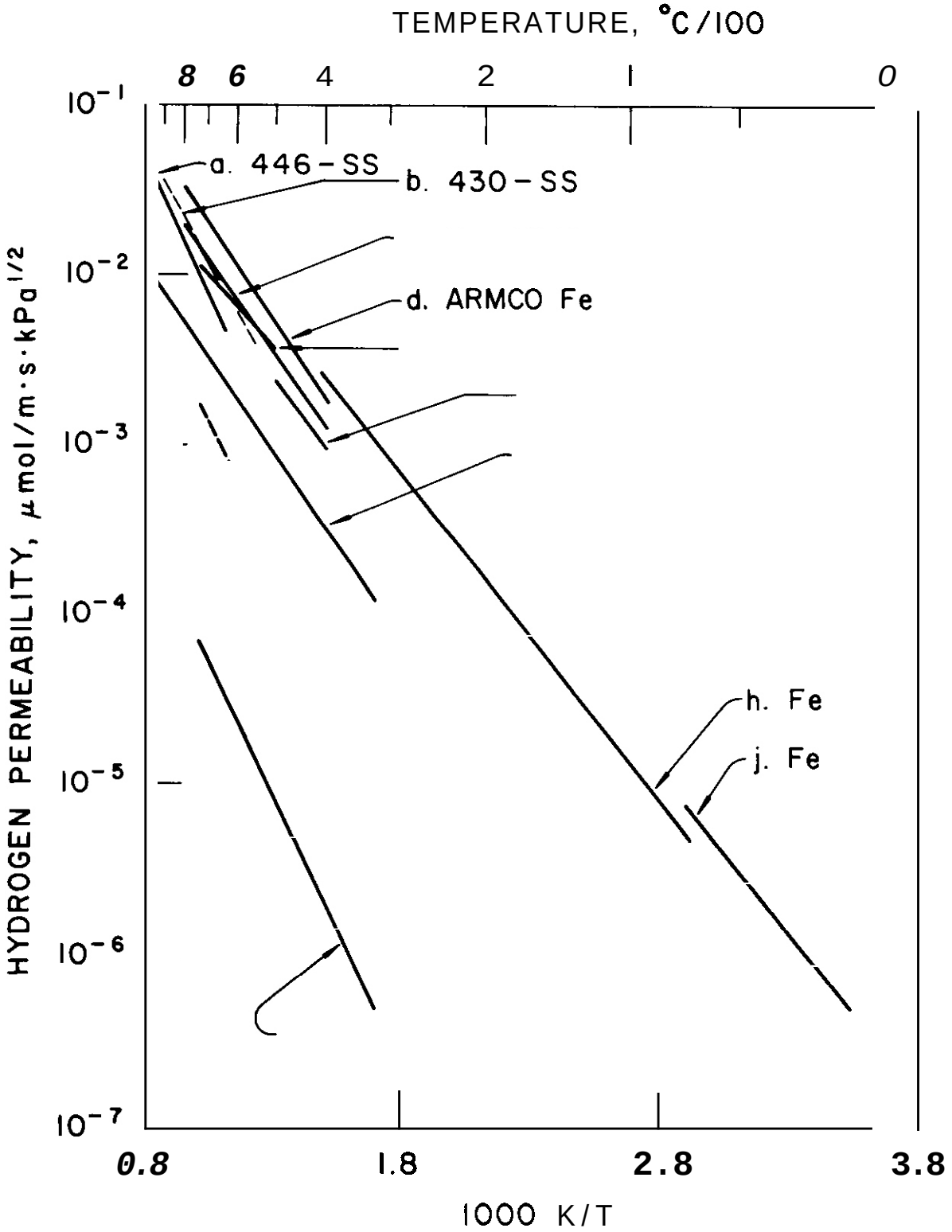

Fig. 9.1.3 Hydrogen Permeability Survey For Pure Iron (Fe) and Iron-Containing Alloys.

The hydrogen permeability of pure iron and iron-base alloys (ferritics) is ∿5-times greater than that of 300-series stainless steels, but significantly reduced permeability can be achieved with some in-situ oxidized aluminum-containing ferritic alloys and steam-oxidized, chromium-containing ferritics.

9.1.6 References

1. E. H. Van Deventer and V. A. Maroni, "Hydrogen Permeation Characteristics of Path A, Path B, and Path C Alloys," *Alloy Development for Irradiation Performance Quarterly Progress Report* for *the Period Ending September 30, 1978,* U. S. Department of Energy Report DOE/ET-0058/3 (1978) pp. 101-107.
2. E. H. Van Deventer, E. Veleckis, and V. A. Maroni, "Hydrogen Dissolution and Permeation Characteristics of Titanium-Base Alloys," *Alloy Development for Irradiation Performance Quarterly Progress Report* for *the Period Ending March 31, 1979,* U. S. Department of Energy Report DOE/ET-0058/5 (1979) pp. 132-140.
3. E. H. Van Deventer and V. A. Maroni, "Hydrogen Dissolution and Permeation of Titanium-Base Alloys," *Alloy Development* for *Irradiation Performance Quarterly Progress Report* for *the Period Ending June 30, 1979,* U. S. Department of Energy Report DOE/ET-0058/6 (1979) pp. 95-98.
4. J. W. Davis, McDonnell Douglas Astronautics Company, personal communication.
5. J. L. Waisman, G. Sines, and L. B. Robinson, "Diffusion of Hydrogen in Titanium Alloys Due to Composition, Temperature, and Stress Gradients," *Metall. Trans.* 4: 291-302 (1973).
6. E. Veleckis and A. G. Rogers, Argonne National Laboratory, work in progress.
7. See Chapter 7 of this report.
8. E. H. Van Deventer, V. A. MacLaren, and V. A. Maroni, "Hydrogen Permeation Characteristics of Aluminum-Coated and Aluminum-Modified Steels," *J. Nucl. Mater.* 88: 168-173 (1980).

9.2 VANADIUM ALLOY/LITHIUM PUMPED-LOOP STUDIES - D. L. Smith, R. H. Lee and V. A. Maroni (Argonne National Laboratory)

9.2.1 ADIP Task

I.A.3. Chemical and Metallurgical Compatibility Analysis. The results presented in this section contribute to Subtask I.A.3.4, Milestones I.A.3.c and I.A.3.d.

9.2.2 Objective

The objective of this work is to develop preliminary data on the compatibility of candidate Path C alloys exposed to a flowing lithium environment. The major effort involves investigations of nonmetallic element interactions in reactive/refractory metal-lithium systems and the effects of lithium exposure on the mechanical properties of refractory metal alloys. Information relating to atmospheric contamination of reactive/refractory metal alloys will also be generated. Specific near-term experiments include measurements of the distribution of non-metallic elements between selected refractory metals and lithium. The results of this work will contribute to the data base that relates compatibility and corrosion phenomena to other alloy development activities and will provide a basis for selecting candidate Path C alloys for further development.

9.2.3 Summary

The stainless steel-clad vanadium alloy loop with circulating lithium has continued to operate through the first quarter of FY 1980. Test samples of zirconium, vanadium, V-15Cr-5Ti, titanium, and yttrium have been exposed at 873 K to investigate the distribution of nonmetallic elements in lithium/refractory metal systems. The zirconium and yttrium exposures have been used to adjust and evaluate the nonmetallic (O, N, H, and C) concentration in lithium. Results of hydrogen analyses of the test samples have been compared with calculated distribution coefficients for hydrogen. Similar analyses of oxygen and nitrogen distribution are in progress.

9.2.4 Progress and Status

Investigations are continuing on the distribution of nonmetallic elements in lithium/Path C alloy systems. Tests are being conducted in a small forced-circulation stainless steel-clad vanadium-alloy loop. The loop has been operated continuously for over 6500 h; the first 500 h at 673 K and the remainder at 873 K. In addition to four filtered lithium dip samples for analysis of nitrogen in lithium, samples of zirconium, vanadium, V-15Cr-5Ti, titanium, and yttrium have been exposed to the lithium. The zirconium and yttrium exposures were conducted primarily to reduce the nitrogen and hydrogen concentrations. As reported previously, nitrogen concentrations in the lithium were reduced substantially (from 1342 to 36 ppm) during the first 2000 h.[1] Oxygen and hydrogen analyses of the zirconium samples will also contribute to the determination of oxygen and hydrogen concentrations in the lithium. The distribution of nonmetallic elements between lithium and the vanadium, V-15Cr-5Ti, and titanium will be determined.

Table 9.2.1 summarizes results for the hydrogen analyses of several lithium-exposed samples. Hydrogen analyses of the zirconium and yttrium were quite reproducible, whereas considerable variation in the results are noted in the titanium and vanadium analyses. Because of the relatively high diffusion rates of hydrogen in these metals at 873 K, the hydrogen concentrations are assumed to be in equilibrium with the hydrogen concentration in lithium. From distribution coefficients calculated by Natesan and Smith,[2] the predicted hydrogen concentration in lithium based on the zirconium results is 120 wppm or a hydrogen pressure of 2×10^{-2} Pa (1.5×10^{-4} torr). If the yttrium data is used to make this prediction, the corresponding values are 80 wppm and 1.7×10^{-2} Pa. The calculated distribution coefficients indicate that the hydrogen concentrations in zirconium and titanium should be about the same. Since the zirconium samples were larger, the experimental results are probably more reliable than those for titanium. The vanadium results, which are higher than expected in comparison with the zirconium and titanium values, are subject to more uncertainty because of the low

values and relatively small sample sizes. Additional analyses on pure vanadium and vanadium alloy samples are in progress. Results from the yttrium samples show that yttrium is effective for reducing the hydrogen concentration in the lithium.

Table 9.2.1 Hydrogen Analyses of Metal Samples After Exposure to 873 K Lithium in Vanadium Alloy Loop

Sample No.	Exposure Time, h	Measured Hydrogen Concentration, wppm	Calculated[a] Hydrogen Concentration, wppm
Zr-2	168	21	13
Zr-3	550	20,17	13
Ti-2	550	104,39	16
V-2	110	10,10	0.4
V-3	470	19,<1	0.4
Y-2	240	1839,1832	∿1836

[a]Based on the measured data for Y-2.

Oxygen analyses have also been obtained on some of the lithium-exposed sample. These results are presently being evaluated. Exposed samples have also been prepared for nitrogen analysis. Exposed samples are being analyzed with the electron microprobe to evaluate compositional variations in the surface regions.

9.2.5 Conclusions

Hydrogen analyses of zirconium, titanium, and vanadium samples exposed to lithium have been compared with calculated hydrogen distribution coefficients. Preliminary results show some discrepance between measured and calculated distribution coefficients. Additional analyses are expected to reduce the uncertainties in the measured values.

9.2.6 References

1. D. L. Smith, R. H. Lee, and V. A. Maroni, "Vanadium Alloy/Lithium Pumped-Loop Studies," *Alloy Development for Irradiation Performance Quarterly Progress Report for the Period Ending June 30, 1979,* U. S. Department of Energy Report DOE/ET-0058/10 (1979) pp. 99-101.

2. K. Natesan and D. L. Smith, "Effectiveness of Tritium Removal from a CTR Lithium Blanket by Cold Trapping Secondary Liquid Metals Na, K, and NaK," *Nucl. Technol.* 22: 138-150 (1974).

9.3 CORROSION OF Fe-Ni-Cr AND Fe-Ni-V ALLOYS IN STATIC LITHIUM — P. F. Tortorelli and J. H. DeVan (ORNL)

9.3.1 ADIP Task

ADIP Task I.A.3, Perform Chemicai and Metallurgical Compatibility Analyses.

9.3.2 Objective

The purpose of this program is to determine the chemical compatibility of fusion reactor candidate materials with metallic lithium. Specimens are exposed to static lithium containing selected solute additions to identify the kinetics and mechanisms that govern corrosion by lithium. Specific program objectives are: (1) to determine the effects of N, C, H, and O on apparent solubilities in Li; (2) to determine the C and N partitioning coefficients between alloys and Li; (3) to determine the effects of soluble (Ca, Al) and solid (Y, Zr, Ti) active metal additions on corrosion by Li; and (4) to determine the tendencies for dissimilar-metal mass transfer.

9.3.3 Summary

Data are reported on the compatibility of 500 and 600°C lithium with alloy 800 [46 Fe—32 Ni–21 Cr (wt %)] and a long-range-ordered (LRO) alloy [45 Fe—32 Ni–23 V (wt %)]. Although these alloys contained similar concentrations of Fe and Ni, alloy 800 was severely corroded in certain instances, while the LRO alloy resisted attack and incurred no loss of tensile properties in Li.

9.3.4 Progress and Status

Ductile long-range-ordered (LRO) alloys have been developed at ORNL for high-temperature applications.[1] In previous corrosion tests' an LRO alloy composed of 60 Co—25 Fe—15 V (wt %) was found to be compatible with static lithium at 600 and 850°C. Recently we completed a second series of tests with LRO alloy 35 [45 Fe–32 Ni—23 V (wt %)], which is being developed specifically for fusion first-wall applications. Table 9.3.1

Table 9.3.1. Weight Changes of Alloy 800 [46 Fe–32 Ni–21 (wt %)] and LRO-35 [45 Fe-32 Ni–23 V (wt %)]

Test Temperature (°C)	Weight change, g/m^2	
	Alloy 800[a]	LRO-35[b]
500	+16.3, –49.9	-0.2, –0.5, -0.5
600	-2.4, –121.3	–0.2, –0.5, -0.5

[a]1000-h exposures. Two tests were conducted at each temperature.

[b]2000-h exposures. Three tests were conducted at each temperature.

lists the weight changes for this alloy in static lithium along with data for alloy 800 [46 Fe-32 Ni–21 Cr (wt %)]. Note that the iron and nickel concentrations for the respective alloys are comparable. However, the Fe-Ni-Cr alloy suffered large weight losses in certain instances, while the corrosion rates of the ordered Fe-Ni-V alloy were consistently low and were on the order of those previously reported[3] for type 316 stainless steel. Metallographic examination showed that an extensive network of internal voids had formed in the alloy 800 (see Fig. 9.3.1), but little interaction between lithium and the LRO-35 alloy had occurred (see Figs. 9.3.2 and 9.3.3). The attack shown in Fig. 9.3.1 is similar to that reported earlier[2] for alloy 600 [76 Ni-8 Fe–16 Cr (wt %)] exposed to static lithium. Comparison of the tensile elongation of unexposed with exposed LRO-35 specimens (see Table 9.3.2) indicated that lithium had no adverse effect on the ductility of this iron-base ordered alloy.

Since Ni is much more soluble in Li than Fe or Cr, it is to be expected that the dissolution rate of Ni-containing alloys in static Li will increase with increasing Ni concentration. This trend has been observed previously,[2] and the present results for alloy 800 are consistent with this behavior. The low corrosion rates of LRO-35 reported above are a contradiction of this trend and may be attributable to any one or more of three factors: there is a synergistic effect of Cr on the dissolution

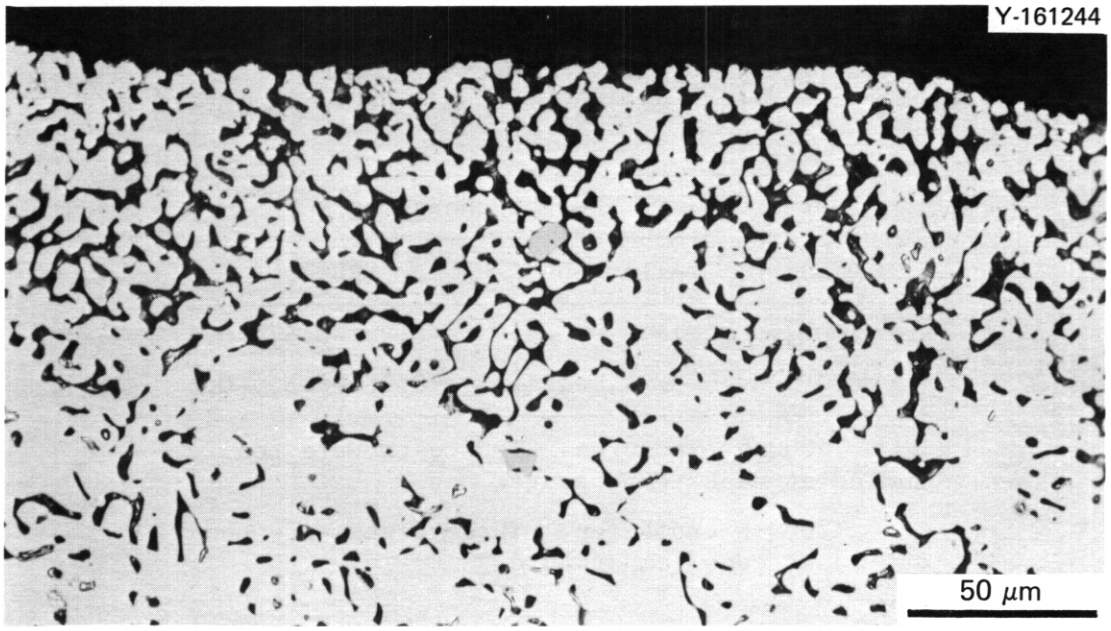

Fig. 9.3.1. Alloy 800 Exposed to Static Lithium at 700°C for 1000 h.

Table 9.3.2. Comparison of the Tensile Elongation of LRO-35 With and Without Prior Exposure to Static Lithium

Exposure	Elongation, %			
	Room Temperature	500°C	600°C	650°C
Unexposed LRO-35	44			34
LRO-35 in 500°C Li for 2000 h	42	38		
LRO-35 in 600°C Li for 2000 h	48		36	

of Ni-bearing alloys in Li, V inhibits the corrosion process, and/or the smaller diffusion rates in the ordered lattice[4] reduce Ni mobility so as to retard the leaching of Ni into the Li (that is, the solution process is no longer rate limiting). We will conduct a further test of LRO-35 in static lithium at a temperature slightly above the critical ordering temperature (670°C) to compare the corrosion behavior of this alloy in the disordered state with that already determined in the ordered state.

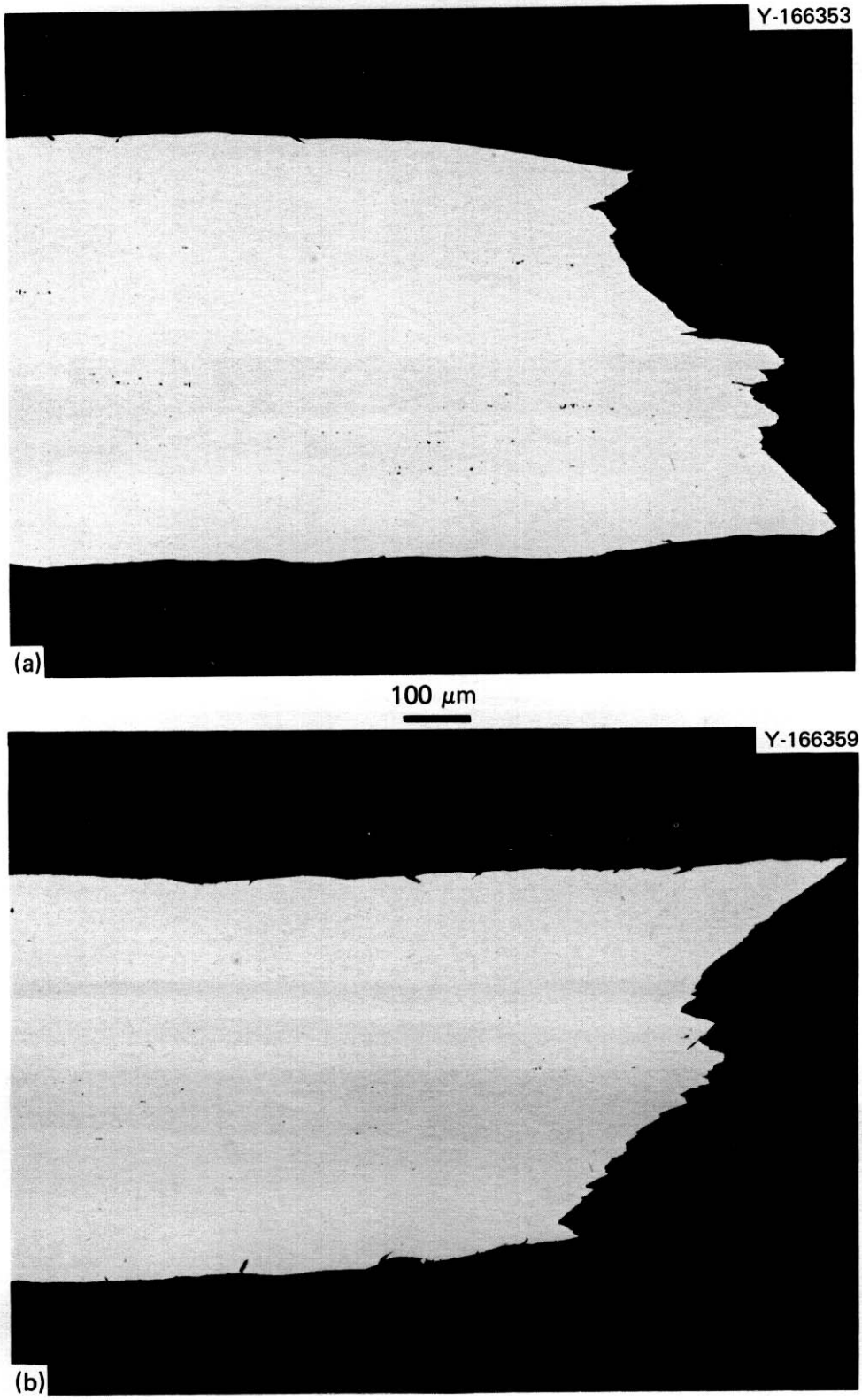

Fig. 9.3.2. The 45 Fe–32 Ni–23 V (wt %) Long-Range-Ordered Alloy Exposed to Static Lithium at (a) 500 and (b) 600°C for 2000 h and Tensile Tested at Room Temperature.

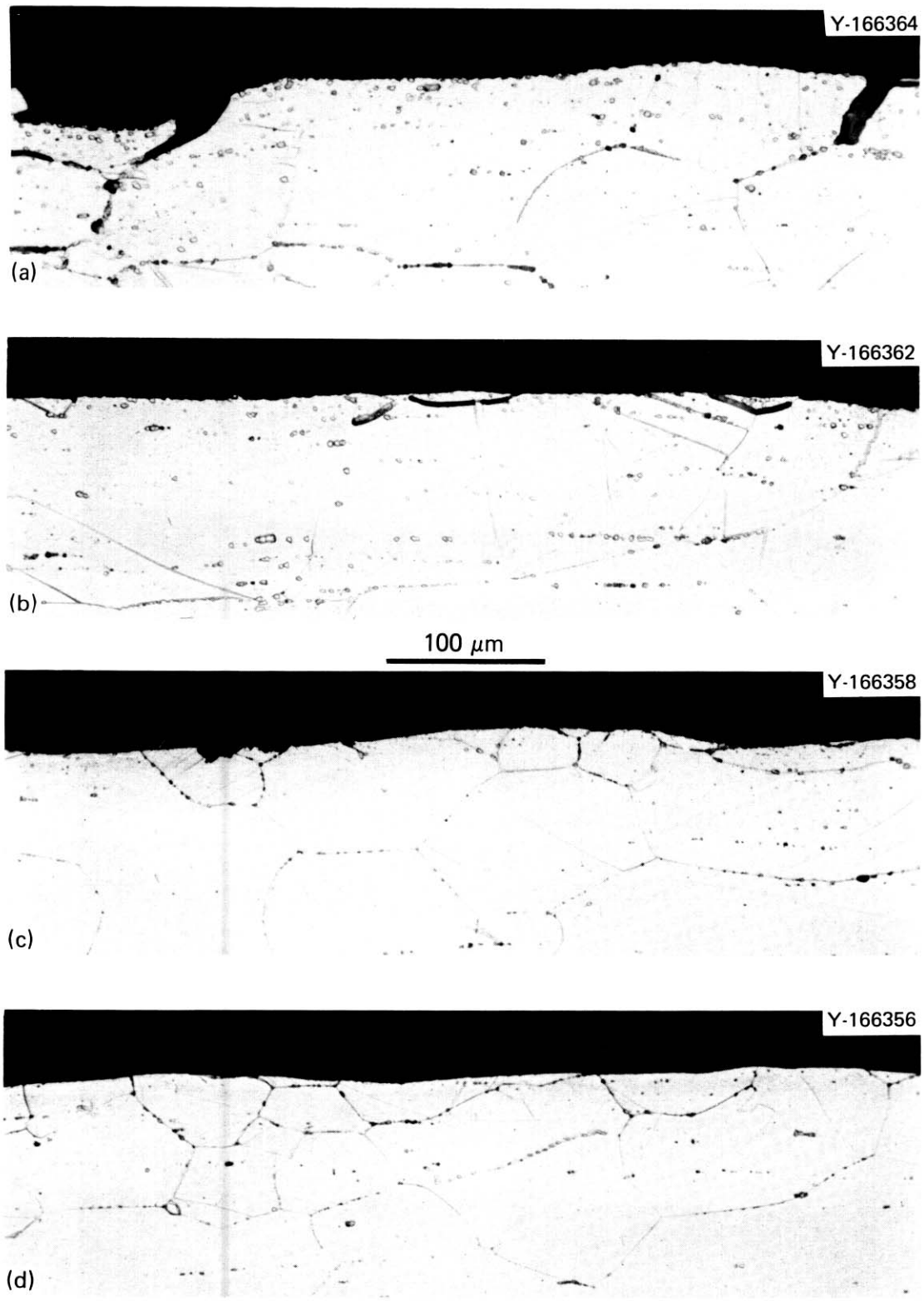

Fig. 9.3.3. The 45 Fe–32 Ni–23 V (wt %) Long-Range-Ordered Alloy Exposed to Static Lithium at (a) 500°C Near Fracture Surface, (b) 500°C in Grip Area, (c) 600°C Near Fracture Surface, and (d) 600°C in Grip Area. Exposure time was with subsequent tensile testing at room temperature.

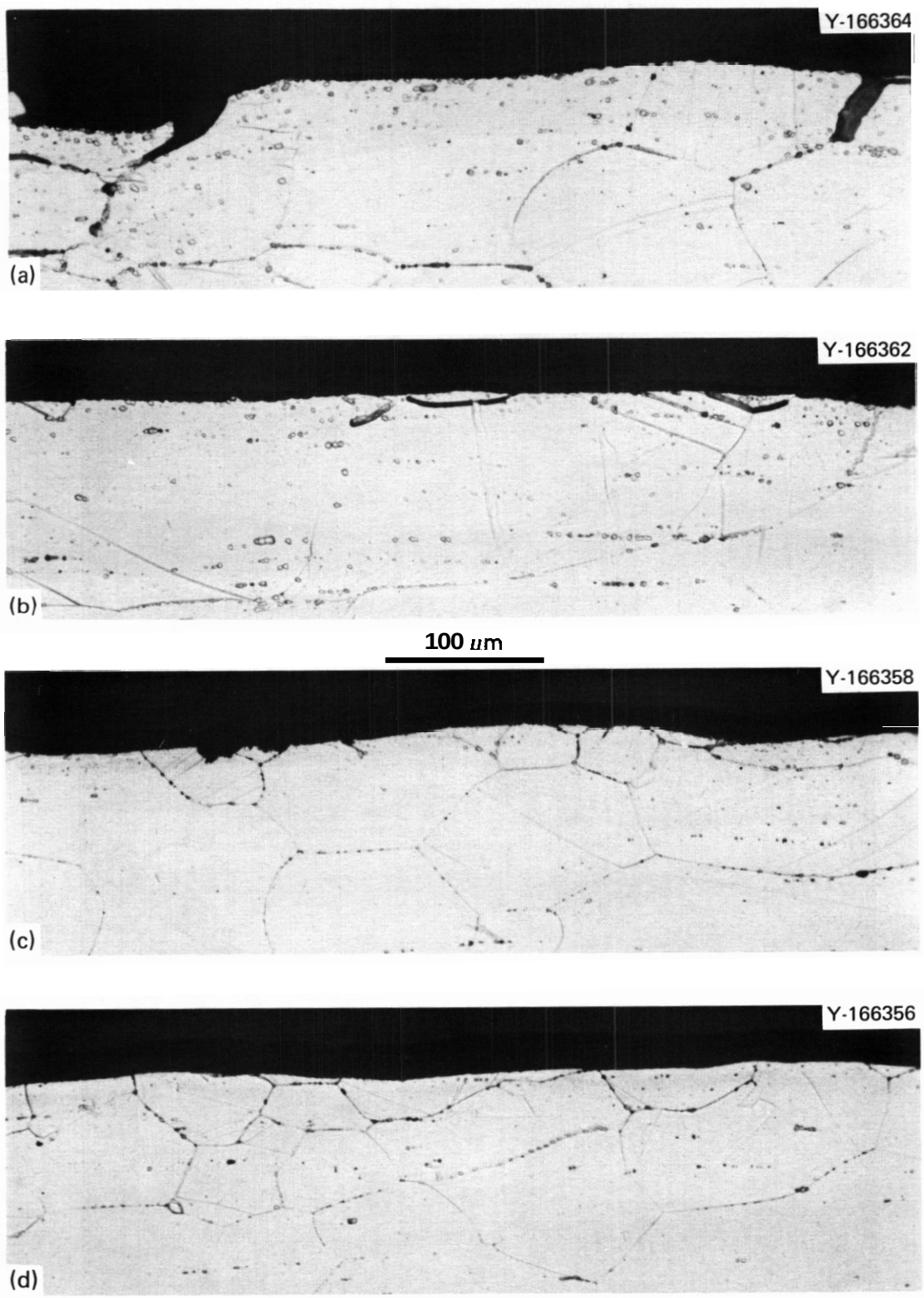

Fig. 9.3.3. The 45 Fe-32 Ni-23 V (wt %) Long-Range-Ordered Alloy Exposed to Static Lithium at (a) 500°C Near Fracture Surface, (b) 500°C in Grip Area, (c) 600°C Near Fracture Surface, and (d) 600°C in Grip Area. Exposure time was with subsequent tensile testing at room temperature.

9.3.5 Conclusion

The LRO-35 alloy has acceptable compatibility with static lithium at 500 and 600°C. Alloy 800, which has similar concentrations of Fe and Ni, was significantly attacked in static Li at these temperatures.

9.3.6 References

1. C. T. Liu, "Development of Ductile Long-Range Ordered Alloys for Fusion Systems," *J. Nucl. Muter.* 85 & 86: 907–11 (1979).
2. P. F. Tortorelli and J. H. DeVan, "The Corrosion of Ni-Fe-Cr and Co-V-Fe (LRO) Alloys in Static Lithium," *ADIP Quart. Prog. Rep. Mar. 31, 1979,* DOE/ET-0058/5, pp. 141–47.
3. J. H. DeVan and J. R. DiStefano, "Capsule Tests of Iron-Base Alloys in Lithium," *ADIP Quart. Prog. Rep. Mar. 31, 1978,* DOE/ET-0058/1, pp. 190–99.
4. E. M. Schulson, "Order Strengthening as a Method for Reducing Irradiation Creep," *J. Nucl. Muter.* 66: 322 (1977).

9.4 CORROSION OF TYPE 316 STAINLESS STEEL AND ALLOYS B1 AND B3 IN LITHIUM THERMAL-CONVECTION LOOPS — P. F. Tortorelli and J. H. DeVan (ORNL)

9.4.1 ADIP Task

ADIP Task I.A.3, Perform Chemical and Metallurgical Compatibility Analyses.

9.4.2 Objective

The purpose of this task is to evaluate the corrosion resistance of candidate first-wall materials to flowing lithium in the presence of a temperature gradient. Corrosion rates (in both dissolution and deposition) are measured as functions of time, temperature, additions to the lithium, and flow conditions. These measurements are combined with chemical and metallographic examinations of specimen surfaces to establish the mechanisms and rate-controlling processes for dissolution and deposition reactions.

9.4.3 Summary

Results from three thermal-convection-loop experiments are reported. The corrosion rates of ADIP alloys B1 and B3 [64 Fe—25 Ni—10 Cr—1 Mo (wt %) and 56 Fe—30 Ni—12 Cr—3 Mo (wt %), respectively] were much greater than that of type 316 stainless steel. Similar corrosion rates in flowing lithium were measured for type 316 stainless steel in both austenite and a-ferrite systems. Adding aluminum to a type 316 stainless steel loop that had already been circulating lithium for over 5000 h resulted in flow restrictions that were probably the result of aluminum deposits in the coldest part of the circuit. Consequently, corrosion inhibition by aluminum addition to the lithium is most effective in a new system.

9.4.4 Progress and Status

As described previously,[1] two types of thermal-convection loops (TCLs) are being used to evaluate the compatibility of Path A and B materials with lithium. The first type is in the form of a 0.46 by 0.64-m parallellogram that contains interlocking tab specimens of the same material as

the loop. The loop is operated without interruption for 3000 to 10,000 h and is then cut open to remove tab specimens for analysis. The second type of TCL is larger (0.48 by 0.76 m) and is designed so that tab specimens can be withdrawn and inserted without altering the loop operating conditions. *In* this way corrosion rates can be monitored at selected time intervals for a given set of test specimens.

An alloy 800 [46 Fe—32 Ni—21 Cr (wt %)] TCL of the first type has been used to test ADIP alloys B1 [64 Fe—25 Ni—10 Cr—1 Mo (wt %)] and B3 [56 Fe—30 Ni—12 Cr—3 Mo (wt %)] **in** flowing lithium. The loop circulated lithium between 500 and 300°C for 2832 h before being terminated as a result of flow restrictions. The resulting weight changes of coupons situated around the loop are shown in Fig. 9.4.1 and can be compared with data **from** a similar loop of type 316 stainless steel. Note that the corrosion rates of the Path B materials are significantly greater than

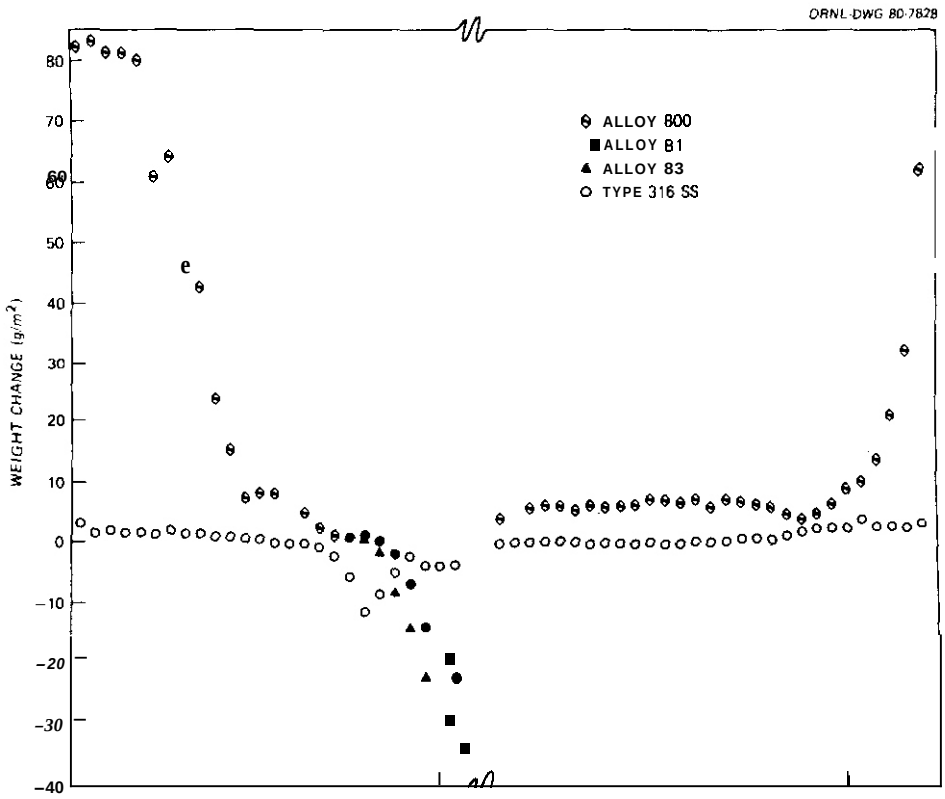

that of type 316 stainless steel under the same temperature conditions. The weight loss rate appears to he directly proportional to the nickel concentration of the alloy (see Fig. 9.4.1). Because of this the pure nickel wire (0.8 mm in diameter) used to connect the loop coupons was completely dissolved in the hotter region of the loop. This affected the present weight change results in two ways. The first is that the nickel from the dissolved wire deposited on the cooler surfaces of the loop and contributed significantly to the weight gains shown in Fig. 9.4.1. This accounts for the greater net specimen weight gain over net weight loss. The second is that the nickel wire may have acted to buffer the dissolution of the Path B coupons in the hotter zone. This effect would lead to coupon weight losses that were smaller than those in a loop that did not contain any pure nickel. The reported corrosion rates for alloys B1 and B3 are therefore minimum. The surface compositions of the loop coupons are presently being determined by x-ray fluorescence to assess whether surface concentrations of nickel are higher in the immediate vicinity of the dissolved wire than at positions further away. If the amount of nickel from the dissolved wire is taken into account in a mass balance, the corrosion rates of alloys B1 and B2 would approximately increase by a factor of 4. In any case this does not change the basic observation that the corrosion rates of Path B alloys in lithium are significantly greater at 500°C than those of Path A materials.

In the preceding quarterly' we reported that the corrosion rates of "virgin" type 316 stainless steel specimens inserted in a loop that had circulated lithium for over 5000 h at a maximum temperature of 600°C were not greatly enhanced over those measured in a new loop under similar conditions. We therefore concluded that the corrosion of type 316 stainless steel was not significantly accelerated by dissimilar-metal transfer when a-ferrite was also present. We have continued the operation of this TCL and measured the coupons' weight changes after an additional 500-h exposure. The cumulative data for the weight loss of the coupon at the maximun loop temperature *(600°C)* are shown in Fig. 9.4.2 as the solid circles (specimen 3B-H3). The open circles (specimen 3A-H3) are previous data from the earlier operation of the loop when both the TCL and coupons

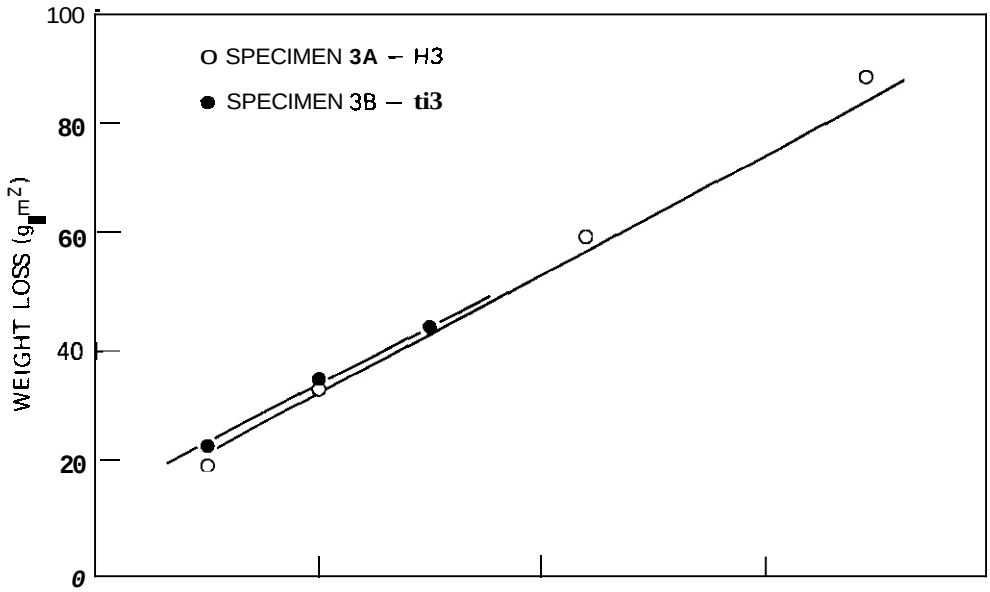

were initially austenitic.' The addition of the latest data point allows a tentative steady-state corrosion rate to be derived from the slope of the weight loss-vs-exposure time curve in a similar manner to that used with previous data.[2] This corrosion rate for specimen 3B-H3, 21.2 mg/m^2h, is the same as that suffered by the original coupon (3A-H3) in that loop position, 21.3 mg/m^2h, and is consistent with the dissolution of an iron-rich surface (produced by the rapid leaching of nickel from the austenite) being rate controlling at steady state. Therefore, it is to be expected that in an all-austenite system (as with specimen 3A-H3), an austenite-ferrite system (as with specimen 3B-H3), or an all-ferrite system, the corrosion rates will quickly converge because of the destabilization of austenite in lithium caused by the preferential leaching of nickel. The magnitude of dissimilar-metal transfer in an austenite-ferrite system is small, and such an effect will only occur during the initial stage of exposure to lithium.

Earlier we reported[3] that the addition of aluminum to lithium before the start of a type 316 stainless steel TCL experiment resulted in decreasing the corrosion rate at 600°C during subsequent operation by a

factor of 5. In the preceding quarterly' we reported that the addition of aluminum to the lithium stream of a type 316 stainless steel TCL that had been in operation between 600 and 450°C for over 5000 h resulted in a rapid reaction with the stainless steel and also caused the loop to quickly plug. Since then the loop has been drained, has been flushed with a charge of lithium, and has been refilled. New type 316 stainless steel specimens (specimen set b) were inserted into the loop and were exposed for 500 ti, after which the TCL again showed signs of flow restrictions. Therefore, the loop's lithium was drained once again, a flush charge was circulated, the TCL was refilled, and new coupons (specimen set c) were inserted. After 500 h of operation flow restrictions were again apparent.

Figure 9.4.3 contains the 500–h weight change data as a function of loop position from the various stages of operation of this TCL. The first set of data (a) is for the coupons that were in the loop before the aluminum was added. The second and third sets (b and c) are for the type 316 stainless steel coupons from the second and third fills,

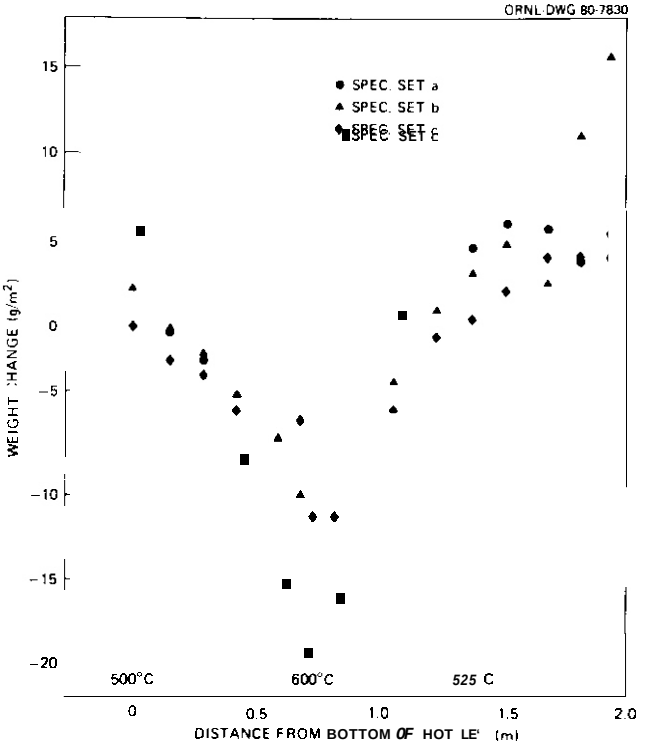

Fig. 9.4.3. Weight Changes vs Loop Position for Type 316 Stainless Steel After 500 h.

respectively. When compared to the specimens of set a, it is apparent that the hot-leg coupons of specimen sets b and c suffered significantly lower weight losses, while the cold-leg coupons gained more weight than the original specimens. Examination of the specimens of set b by scanning electron microscopy indicated the presence of nickel-aluminum deposits on the coupons near the bottom of the cold leg (see Fig. 9.4.4), but very little aluminum was found elsewhere.

Since nickel is preferentially leached in austenitic stainless steel-lithium systems, a significant quantity of nickel in this TCL had mass transferred from the hotter to the colder parts of the loop before the insertion of the aluminum into the lithium. When the Al was added it could be expected to react with both Ni and Fe to form aluminides with these elements. If Ni were concentrated near the bottom of the cold leg, reaction with Al could produce Ni-A1 deposits, similar to those in Fig. 9.4.4 that were sufficient in volume to cause the observed flow restriction. Alternatively, aluminum reacting with iron in the hotter regions of the loop could have produced layers that tended to spall and lead to flow restrictions as the spalled products accumulated in lower parts of the loop. After the draining and refilling of the loop with lithium, a redistribution of the aluminum to the fresh type 316 stainless steel coupon surfaces in the hot leg and to mass-transferred nickel on the cold-leg coupons would account for the reduced corrosion rates and enhanced deposition, respectively, for specimen sets b and c (see Fig. 9.4.3). These results imply that aluminum additions to lithium will be most effective when added to an uncorroded austenitic stainless steel-lithium system. Otherwise the deposits formed by the aluminum may adversely affect lithium flow in the circuit.

9.4.5 Conclusions

1. The corrosion rates of ADIP alloys B1 and B3 in flowing lithium are significantly greater than that for type 316 stainless steel.

2. The steady-state corrosion rate of type 316 stainless steel in a flowing lithium/α-ferrite system is the same as that in an all-type-316 system. Dissimilar-metal transfer between austenite and ferrite in flowing lithium is transitory, and its magnitude is small.

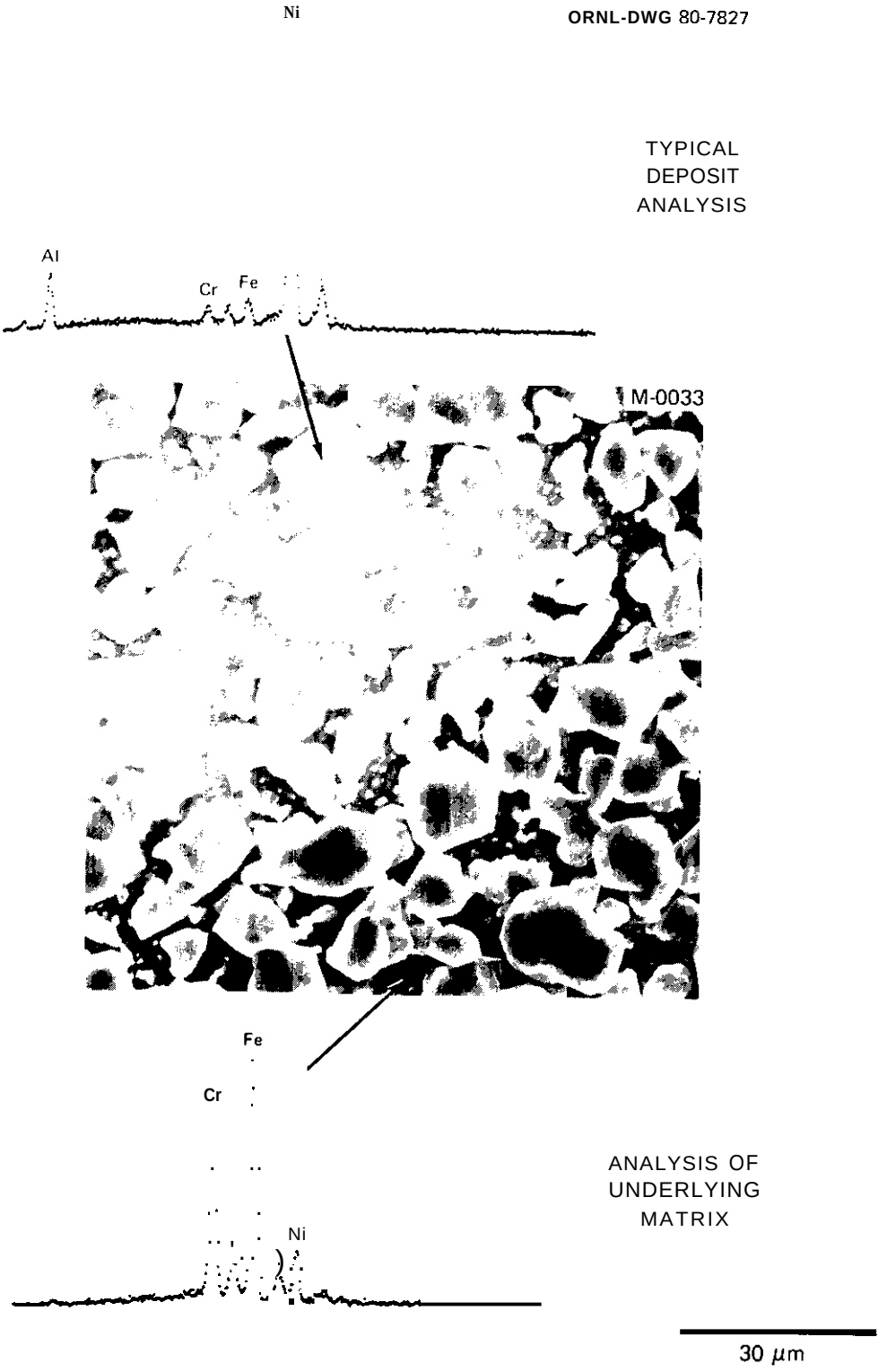

Fig. 9.4.4. Deposits on a Cold-Leg Coupon (About 450°C) in a Type 316 Stainless Steel-Lithium Thermal-Convection Loop to Which Aluminum was Added.

3. Aluminum additions to lithium will be most effective when they are made in an uncorroded austenitic stainless steel circuit. Otherwise the formation of aluminum deposits may lead to flow restrictions.

9.4.6 References

1. P. F. Tortorelli and J. H. DeVan, "Thermal-Convection Loop Tests of Fe-Ni-Cr Alloys," *ADIP Quart. Prog. Rep. Sept. 30, 1979*, DOE/ET-0058/7, pp. 170-74.
2. P. F. Tortorelli and J. H. DeVan, "Thermal-Gradient Mass Transfer in Lithium-Stainless Steel Systems," *J. Nucl. Muter.* 85 & 86(II, A): 289–93 (1979).
3. J. H. DeVan and J. R. DiStefano, "Thermal-Convection Loop Tests of Type 316 Stainless Steel in Lithium," *ADIP Quart. Prog. Rep. Mar. 31, 1978*, DOE/ET-0058/1, pp. 200–08.

9.5 COMPATIBILITY OF TYPE 316 STAINLESS STEEL WITH THE TRITIUM-PROCESSING SALT LiF-LiCl-LiBr — J. R. Keiser and P. F. Tortorelli (ORNL)

9.5.1 ADIP Task

ADIP Task I.A.3, Perform Chemical and Metallurgical Compatibility Analyses.

9.5.2 Objective

Molten salts have been proposed for blanket, coolant, and tritium-processing applications in a fusion reactor. The purpose of the present work is to determine the corrosion behavior of candidate alloys in appropriate molten salts.

9.5.3 Summary

A type 316 stainless steel thermal-convection loop circulated LiF-LiCl-LiBr for over 8000 h. The steady-state corrosion rate was low enough to assure adequate compatibility between the salt and stainless steel.

9.5.4 Progress and Status

A LiF-LiCl-LiBr salt has been proposed[1] for use as a means to extract tritium from a lithium blanket by contacting lithium with this salt, reseparating the salt and metal phases, and subsequently processing the tritium from the LiF-LiCl-LiBr. Consequently, the corrosion of type 316 stainless steel by flowing (about 15 mm/s) LiF-LiCl-LiBr has been studied to determine whether compatibility with the structural material would be limiting in such a system. The thermal-convection loop (TCL) used for this work has been described previously,[2] and preliminary data have already been reported.[2] Loop operation has been terminated after greater than 8000 h of coupon exposure. The measured weight losses for the coupon at the maximum temperature position (540°C) are plotted as a function of exposure time in Fig. 9.5.1. The corrosion rate up to about 2700 h (derived from the slope of the best-fit line in Fig. 9.5.1) was low: 1.6 mg/m^2h. At that time a small amount of lithium was added to

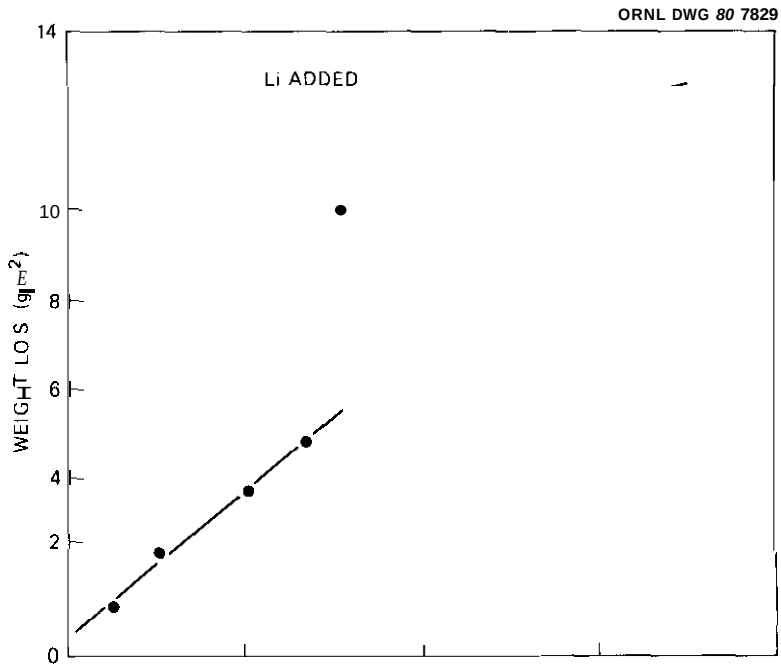

the LiF-LiCl-LiBr to simulate processing conditions and, as shown in Fig. 9.5.1, the weight loss increased dramatically during the next few hundred hours. This can be attributed to free lithium in the loop, but the details of such behavior await analysis of the controlled potential voltammetry data. In any case the effect was temporary, and after an additional 1500 h the corrosion rate decreased to 0.4 mg/m^2h. This low rate indicates that type 316 stainless steel has acceptable compatibility with LiF-LiCl-LiBr.

9.5.5 Conclusion

The corrosion rate of type 316 stainless steel in flowing LiF-LiCl-LiBr is low (≤ 1 mg/m^2h).

9.5.6 References

1. W. F. Calaway, "Electrochemical Extraction of Hydrogen from Molten LiF-LiCL-LiBr and Its Application to Liquid-Lithium Fusion Reactor Blanket Processing," *Nucl. Technol.* 39: 63–74 (1978).

2. J. R. Keiser and J. H. DeVan, "Design and Operation of Thermal-Convection Loops for Corrosion Measurements in LiF-LiCl-LiBr," NACE Corrosion/79 paper 117, Atlanta, Georgia, March 12—16, 1979.

DOE/ER-0045/1
Distribution
Category
UC-20, 20c

DISTRIBUTION

1–4. Argonne National Laboratory, 9700 South Cass Avenue, Argonne, IL 60439

L. Greenwood
V. Maroni
D. L. Smith
H. Wiedersich

5–6. Battelle-Pacific Northwest Laboratory, P.O. Box 999, Richland, WA 99352

J. L. Brimhall
D. Dingee

7. Carnegie-Mellon University, Schenley Park, Pittsburgh, PA 15213

J. C. Williams

8–203. Department of Energy, Technical Information Center, Office of Information Services, P.O. Box 62, Oak Ridge, TN 37830

For distribution as shown in TIU-4500 Distribution Category, UC-20 (Magnetic Fusion Energy), and UC-20c (Reactor Materials)

204–209. Department of Energy, Office of Fusion Energy, Washington, DC 20545

M. M. Cohen
T. C. Reuther, Jr. (5 copies)

210. Department of Energy, Oak Ridge Operations Office, P.O. Box E, Oak Ridge, TN 37830

Office of Assistant Manager, Energy Research and Development

211. General Atomic Company, P.O. Box 81608, San Diego, CA 92138

S. M. Rosenwasser

212—217. Hanford Engineering Development Laboratory, P.O. Box 1970, Richland, WA 99352

D. G. Doran
J. J. Holmes
R. E. Nygren
E. C. Opperman
R. W. Powell
J. L. Straalsund

218—219. Lawrence Livermore Laboratory, P.O. Box 808, Livermore, CA 94550

M. Guinan
C. M. Logan

220. Massachusetts Institute of Technology, Cambridge, MA 02139

D. J. Rose

221—222. McDonnell Douglas Astronautics Company, East, P.O. Box 516, St. Louis, MO 63166

J. W. Davis
D. L. Kummer

223—225. Naval Research Laboratory, Washington, DC 20375

Superintendent, Materials Science and Technology Division
J. A. Sprague
H. Watson

226—253. Oak Ridge National Laboratory, P.O. Box X, Oak Ridge, TN 37830

Central Research Library (2 copies)
Document Reference Section
Laboratory Records Department (2 copies)
Laboratory Records Department, RC
ORNL Patent Section
B. G. Ashdown
E. E. Bloom (5 copies)
D. N. Braski
J. H. DeVan
T. A. Gabriel
M. L. Grossbeck
M. R. Hill (3 copies)
K. C. Liu
P. J. Maziasz
C. J. McHargue
T. K. Roche
J. L. Scott
P. F. Tortorelli
F. W. Wiffen
J. W. Woods

254–255. Sandia Laboratories, Livermore Division 8316, Livermore, CA 94550

J. Swearengen
W. Baller

256. University of California, Department of Chemical, Nuclear, and Thermal Engineering, Los Angeles, CA 90024

R. W. Conn

257. University of Virginia, Department of Materials Science, Charlottesville, VA 22901

W. A. Jesser

258. University of Wisconsin, 1500 Johnson Drive, Madison, WI 53706

W. G. Wolfer

259. Westinghouse Electric Company, Fusion Power Systems Department, P.O. Box 10864, Pittsburgh, PA 15236

R. E. Gold

U S GOVERNMENT PRINTING OFFICE 1980 640 245/015